The Environment of Quasars in the High Redshift Universe

内山　久和

博士（理学）

総合研究大学院大学
物理科学研究科
天文科学専攻

平成３０（２０１８）年度

The Environment of Quasars in the High Redshift Universe

A Dissertation
for Degree of Doctor of Philosophy, 2019

Department of Astronomical Science
SOKENDAI (The Graduate University for Advanced Studies)

Hisakazu Uchiyama

Abstract

Luminous quasars are generally thought to be formed through major mergers of gas-rich galaxies. At a high redshift, the reservoir of the gas feeding the quasars can be supplied by major (wet) mergers. This suggests that the activity of quasars and therefore, their supermassive black hole (SMBH) growth, may depend not only on their intrinsic properties but also on the surrounding environment beyond the scale of a galaxy. It is generally assumed that the most luminous quasars and galaxies are hosted by massive halos, as suggested by M-σ relations. Therefore, if quasar activity is triggered by frequent mergers, it should preferentially occur in the peaks of the matter density, i.e., high redshift protoclusters (or clusters in the formation) that are thought to evolve into the galaxy clusters seen in the local universe. However, this topic is still controversial and a consistent picture for the environment of high-z quasars has not yet been settled. In addition, the extreme rarity for both protoclusters and quasars does not allow us to derive a general picture of their relation.

Moreover, there is another aspect that makes it difficult to evaluate the quasar environment. The most luminous quasars could suppress galaxy formation in their surroundings through feedback, "photoevaporation": photoionization heating by an intense ultra-violet (UV) radiation from the quasars can evaporate collapsed gas in the halo and further inhibit gas cooling. This phenomenon could be effective around luminous quasars, especially in terms of preventing the formation of low-luminosity galaxies even if some of these quasars reside in very massive dark matter halos. However, the occurrence of this process is not readily apparent during observations, because in addition to the small field-of-view (FoV), previous studies have not probed deep enough to investigate galaxies with sufficiently low luminosity or low mass, where more effective photoevaporation is expected.

In this thesis, the advantages of the wide-field imaging capability of a Subaru telescope was exploited to characterize the large-scale environment of high-redshift quasars by systematically investigating (1) the number of galaxies that are clustered around quasars, and (2) the extent of the influence of the radiation effect of quasar on these surrounding galaxies. Two wide-field images dataset produced by Subaru were used. One is the 1st release data (DR1) of the Hyper Suprime-Cam Subaru Strategic Program (HSC-SSP) of $\sim$ 121 square degrees to statistically characterize the environment of a large number of optically selected quasars at $z \sim 3.8$ from the Sloan Digital Sky Survey (SDSS). The other is the narrow-band images obtained using the Suprime-Cam to target 11 fields of quasars at $z \sim 2-3$, to study the radiative feedback effects on the surrounding low-luminosity galaxies systematically.

Firstly, a cross-correlation between the positions of the SDSS quasars at $z \sim 4$ and the bias-free wide-field protocluster catalog was performed, which is produced by HSC-SSP DR1 data at the same redshift. It was found that only two out of 151 quasars exist in regions with galaxy overdensity significance of more than 4σ, compared to the field. The distributions of the angular separation between the nearest protoclusters and quasars are statistically identical to those found in the g-dropout galaxies (star-forming galaxies at $z \sim 4$). In addition, the overdense significance at the position of the quasars are also the same as those of g-dropout galaxies. These results suggest that at this redshift, quasars tend to exist in almost the same environment as star-forming galaxies. Using stacking analysis, it was found that the mean density of the g-dropout galaxies in the vicinity of quasars is slightly higher than that in the region of g-dropout galaxies over $1.0 - 2.5$ physical Mpc (pMpc) scales. However, at < 0.5 pMpc, the values in the vicinity of quasars tend to be lower. I also found that quasars with more massive black holes or higher UV-luminosity tended to avoid the most overdense regions. These results are consistent with a scenario in which the $z \sim 4$ luminous quasar exists in structures that are less massive than those expected for the progenitors of the current mature galaxy clusters.

Next, I focused on the Lyman alpha emitters (LAEs) to examine the possible photoevaporation effect of quasar UV radiation on surrounding low mass galaxies systematically at $z = 2 - 3$. I selected LAEs using Suprime-Cam narrow-band images at the same redshifts as the quasars at $z \sim 2$. The proximity zone of a quasar is defined by the region where the local UV radiation from this entity is comparable to the UV background. It was found that LAEs with a rest-frame equivalent width of Lyman alpha emission (EW_0) of > 150Å which is a sign of lower stellar mass ($< 10^8 M_\odot$) are scarce in the quasar proximity zones. This suggests that quasar photoevaporation is effective. The halo mass of LAEs with $EW_0 > 150$Å is estimated to be $3.6^{+12.7}_{-2.3} \times 10^9 M_\odot$, either from the Spectral Energy Distribution (SED) fitting or the main sequence. Based on a hydrodynamical simulation, the predicted delay in star formation under a local UV background intensity with $J = 10^{-21}$ erg s^{-1} cm^{-2} Hz^{-1} sr^{-1} for galaxies with less than this halo mass is approximately > 20 Myr. This is longer than the expected age of LAEs with $EW > 150$Å. However, photoevaporation seems to be less effective in the vicinity of very luminous quasars, which is consistent with the idea that these quasars are still in an early stage of quasar activity.

These findings imply that appearance of most quasars is independent of their large-scale environments. Once they appear, low-mass galaxy formation around the quasar will be suppressed because of the intense UV radiation from the quasar, photoevaporation. In the thesis, for the first time, the environment of quasars at high redshifts throughout their lifetime is statistically and observationally revealed.

Acknowledgments

I am deeply grateful to my supervisor, Prof. Nobunari Kashikawa. It is not too much to say that I was able to complete this thesis thanks to him. He gave me helpful advices and useful comments at any time and place when I went to ask him. Thanks to him, I become able to conduct researches with co-investigators have huge growth although I started from zero in astronomy. I wouldn't be the person I am today without him. He was not only the best adviser but also the best co-investigator.

I would like to offer my special thanks to Dr. Jun Toshikawa. He kindly had a discussion with me every day when I began to study. I had a so good start for astronomical study thanks to him. Furthermore, He conduct an one-to-one seminar in order to teach me basics of astronomy.

I owe a very important debt to Prof. Roderik Overzier. When I visited him in an internship in Brazil, he kindly teach me from food, clothing and shelter to study. He kindly discussed many things with me. It's a very nice memory. Moreover, he always carefully checked our papers and proposals, and provided useful comments and discussions.

I would like to express the deepest appreciation to Associate Prof. Masayuki Tanaka who is also my supervisor. He gave me constructive comments and warm encouragement for study and writing this thesis. In addition, he kindly taught me how to observe in the HSC-SSP observation.

I would like to thank the great referees, Associate Prof. Satoshi Miyazaki, Prof.

Ryohei Kawabe, Assistant Prof. Masatoshi Imanishi, Associate Prof. Kazuhiro Shimasaku, and Prof. Tetsu Kitayama for their helpful comments that improved the manuscript.

I would like to express my gratitude to my co-investigators. Dr. Yi-Kuan Chiang gave me helpful comments for stacking analysis. Dr. Murilo Marinello kindly guided in the internship and conducted the estimation of black hole masses. Dr. Yuu Niino gave insightful comments and suggestions in our group meeting. Dr. Shogo Ishikawa always kindly listened to my problems whenever I was worried about something. Dr. Masafusa Onoue gave me many useful comments for our study in a group meeting. Dr. Kohei Ichikawa gave insightful comments and suggestions for our study and a seed of new study. Dr. Kubo Mariko provided helpful advices in meetings. Dr. Masayuki Akiyama provided quasar sample detected by HSC. Assistant Prof. Masatoshi Imanishi gave me useful comments for this thesis. I am particularly grateful for the assistance given by Prof. Jean Coupon, Mr. Yuichi Harikane, Prof. Tadayuki Kodama, Assistant Prof. Yutaka Komiyama, Dr. Chien-Hsiu Lee, Prof. Yen-Ting Lin, Prof. Satoshi Miyazaki, Prof. Tohru Nagao, Prof. Atsushi J. Nishizawa, Dr. Yoshiaki Ono, Prof. Masami Ouchi, Dr. Shiang-Yu Wang, Mr. Kei Ito, Mr. Shigeru Namiki, and Mr. Yongming Liang. I thank Profs. Toru Yamada, Sadanori Okamura and Masahi Chiba for providing access to the NB413, NB503, and NB515 filters, respectively, for our observations.

I would particularly like to thank again my colleagues, Dr. Jun Toshikawa, Dr. Shogo Ishikawa, Dr. Masafusa Onoue, Mr. Kei Ito, Mr. Shigeru Namiki, and Mr. Yongming Liang. They made enormous contribution to our study, giving me many useful comments in meetings and pleasant study life. I am also grateful to Assistant Prof. Masao Hayashi, Assistant Prof. Takuma Izumi, Ms. Haruka Baba and Dr. Taiki Kawamuro for useful comments and discussion.

The Hyper Suprime-Cam (HSC) collaboration includes the astronomical communities of Japan and Taiwan, and Princeton University. The HSC instrumentation

and software were developed by the National Astronomical Observatory of Japan (NAOJ), the Kavli Institute for the Physics and Mathematics of the Universe (Kavli IPMU), the University of Tokyo, the High Energy Accelerator Research Organization (KEK), the Academia Sinica Institute for Astronomy and Astrophysics in Taiwan (ASIAA), and Princeton University. Funding was contributed by the FIRST program from Japanese Cabinet Office, the Ministry of Education, Culture, Sports, Science and Technology (MEXT), the Japan Society for the Promotion of Science (JSPS), Japan Science and Technology Agency (JST), the Toray Science Foundation, NAOJ, Kavli IPMU, KEK, ASIAA, and Princeton University.

This paper makes use of software developed for the Large Synoptic Survey Telescope. We thank the LSST Project for making their code available as free software at http://dm.lsst.org

The Pan-STARRS1 Surveys (PS1) have been made possible through contributions of the Institute for Astronomy, the University of Hawaii, the Pan-STARRS Project Office, the Max-Planck Society and its participating institutes, the Max Planck Institute for Astronomy, Heidelberg and the Max Planck Institute for Extraterrestrial Physics, Garching, The Johns Hopkins University, Durham University, the University of Edinburgh, Queen’ s University Belfast, the Harvard-Smithsonian Center for Astrophysics, the Las Cumbres Observatory Global Telescope Network Incorporated, the National Central University of Taiwan, the Space Telescope Science Institute, the National Aeronautics and Space Administration under Grant No. NNX08AR22G issued through the Planetary Science Division of the NASA Science Mission Directorate, the National Science Foundation under Grant No. AST-1238877, the University of Maryland, and Eotvos Lorand University (ELTE) and the Los Alamos National Laboratory.

Finally, my deepest heartfelt appreciation goes to my family and my partner who are supporting my life. It is thanks to you that I have succeeded thus far.

Contents

Chapter 1 Introduction

It is important to understand galaxy formation and evolution under various environments, leading to a better understanding of the underlying baryonic physics and the global history of our universe (§1.1). In particular, the overdense environments such as protoclusters, which are expected to evolve into clusters, are good laboratories for studying the environmental effects on the properties and evolution of galaxies (§1.2). High-z quasars are expected to preferentially appear in protoclusters and thus, be good tracers of them according to the merger scenario and M-σ relation (§1.3). However, the details of their environment are still not clear in spite of numerous previous studies. This comes from the rarity of quasars and protoclusters, and the use of different depth, coverage, or definition of the surrounding environment in these studies. In addition, the luminous quasars could suppress galaxy formation in their surroundings through complicated feedback, "photoevaporation" (§1.4). Thus, I attempt to systemically and quantitatively characterize the environment of high-z quasars using wide-field imaging based on the Hyper Suprime-Cam and Suprime-Cam mounted on the Subaru telescope, and examine the underlying baryonic physics observationally (§1.5).

1.1 Understanding Complicated Baryonic Physics

It is possible to know how our universe has evolved and its fate by understanding the distribution of dark matter. The evolution of our universe is described by the Einstein equation,

$$G = T, \tag{1}$$

where G is the Einstein tensor containing the cosmological term and T is the energy-momentum tensor. Roughly speaking, the space-time evolution expressed on the left-hand-side is controlled by the distribution of the matter filled in the space-time expressed by the right-hand-side via equation (1). To reduce the equation of motion (1), it is necessary to understand the distribution of the dark matter included in the right-hand-side of equation (1), because dark matter accounts for $\sim 85\%$ of the total matter in the universe, and thus, our universe contains mostly the "invisible" matter. Thus, it can be said that the distribution of dark matter dominantly controls of space-time evolution.

However, it is not easy to understand the distribution of dark matter because there is a difference in the distribution between dark matter and galaxies which can be used as a tracer to shed light on the "invisible" universe dominated by dark matter. This difference is due to baryonic physics such as star formation, merging, inflow/outflow, environmental effects, and Supernovae (SN)/ Active galactic nuclear (AGN) feedback. For example, in terms of star formation, baryonic matter accretes onto dark matter halos according to the hierarchical structure formation scenario, and stars form in the molecular gas dense regions (star-forming regions). Starburst (a burst of star formation) also occurs when gas-rich galaxies merge. Star formation can be significantly affected by the influence of the SN/AGN feedbacks. In the "radio-mode" AGN feedback, jet from the AGN mechanically blow off a large number of baryons outside the halo. However, in the "quasar-mode" AGN feedback, the gas is carried by the radiation pressure from the accretion disk around the central supermassive black hole (SMBH). Inflow and outflow are important processes in the regulation of the star formation process. Gas stripping or strangulation is a specific mechanism for suppressing star formation in cluster galaxies.

Therefore, it is important to understand their diverse, multi-scale, and complicated baryonic physics in order to realize not only dark matter distribution but also the evolution of the universe.

1.2 Environmental effect on galaxy evolution

In order to observationally understand the underlying baryonic physics, it is essential to elucidate the galaxy formation and evolution processes under various environments such as galaxy overdense regions (e.g., clusters), low dense regions (e.g., voids), or the regions exposed strong ultra-violet (UV) radiation from star-forming galaxies or quasars.

The galaxy properties strongly depend on their surrounding environment, as is well-known as the morphology-density relation (Dressler, 1980) (Figure 1) and the color-magnitude relation (Terlevich et al., 2001). For example, in the local universe, the cluster early-type galaxies that are characterized by a high stellar mass and an old stellar population, form a clear "red sequence" in the color-magnitude diagram. In contrast, the young and less massive spiral galaxies tend to reside in low-density regions, forming the other sequence, "blue cloud".

In order to understand when and how the characteristics of cluster galaxies emerge and which processes are essential to their onsets, we need to directly observe "protoclusters" at high-z, which are progenitors of the most massive local clusters. Here, protoclusters are defined as the galaxy overdense regions which evolve into dark matter halos with masses of $> 10^{14}\ M_{\odot}$ at $z = 0$. The tightness of the red sequence up to $z \sim 1.5$ indicates that the major star formation activity in these galaxies took place at an earlier epoch (Kodama et al., 1998). High-z protoclusters are therefore expected to host high star formation activity, corresponding to the major formation epoch of the stellar populations in their galaxies. This is supported by observational evidence of enhanced star formation in the central region of clusters at $z > 1.5$ (e.g. Hayashi et al., 2010) and the disappearance of the red sequence at $z > 2.5$ (Kodama et al., 2007). In an early stage of cluster growth, galaxies frequently experience galaxy merger, which can trigger starburst and exhaust large amounts of gas in galaxies. AGN activity and its feedback effect are the main mechanisms that limit the growth of massive cluster early-type galaxies.

In particular, direct observation in protoclusters at $z > 3$ is the key to understanding the global formation and evolution of cluster galaxies, or providing much information on the primordial conditions at their birth. For example, at $z \sim 2-3$, some protocluster galaxies are on average found to be older and more massive than those in fields (Steidel et al., 2005; Koyama et al., 2013; Cooke et al., 2014), which could either be explained by environmental effects or a faster evolution in biased

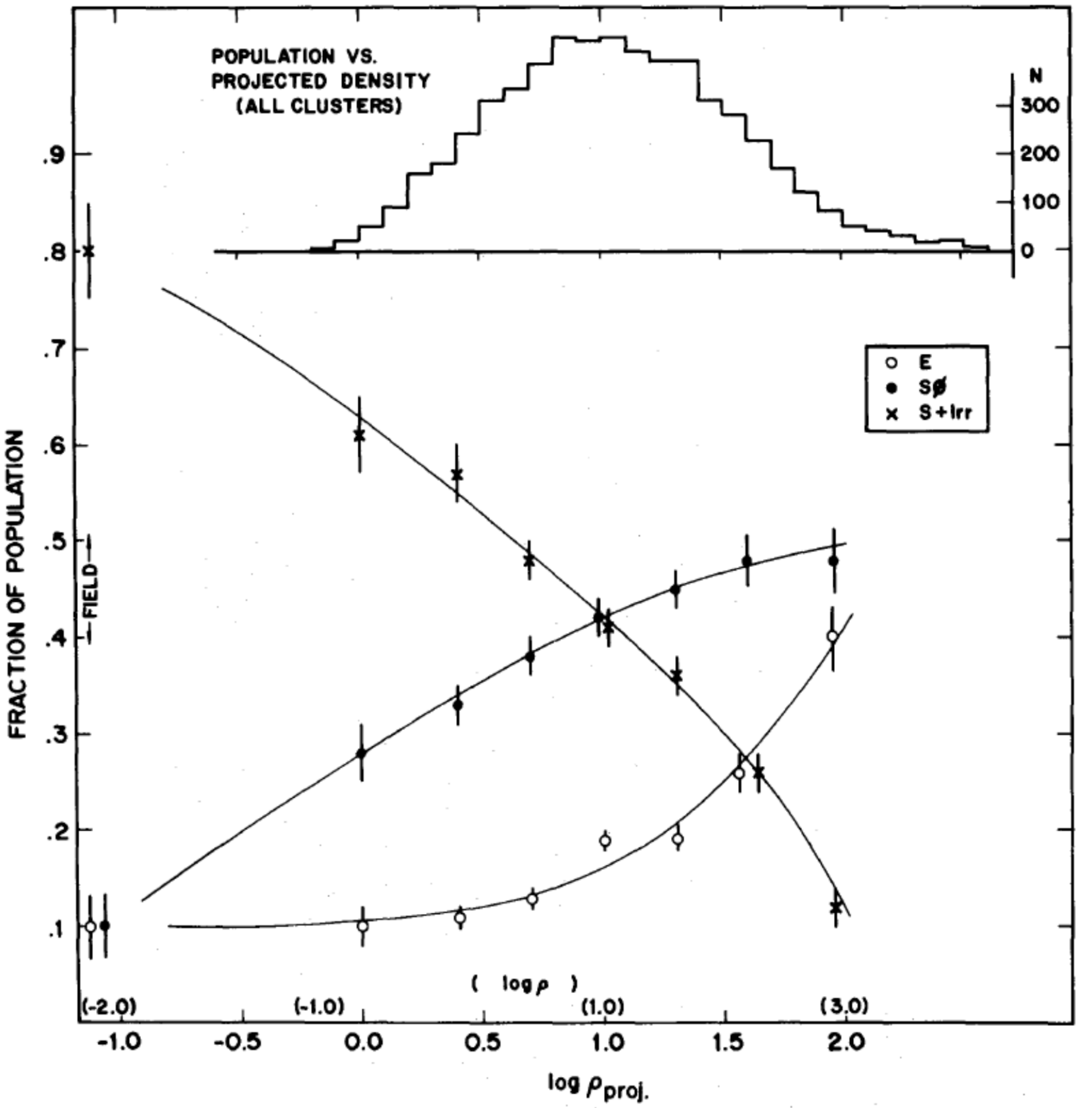

Figure 1 Morphology-density relation taken from Dressler (1980). The fraction of E, S0, and S+I galaxies are drawn as a function of the projected galaxy density. The open circles, black circles, and crosses represent the case of E, S0, and S+I-type galaxies, respectively. The distribution of the galaxies in the bins of the density is represented by the upper histogram.

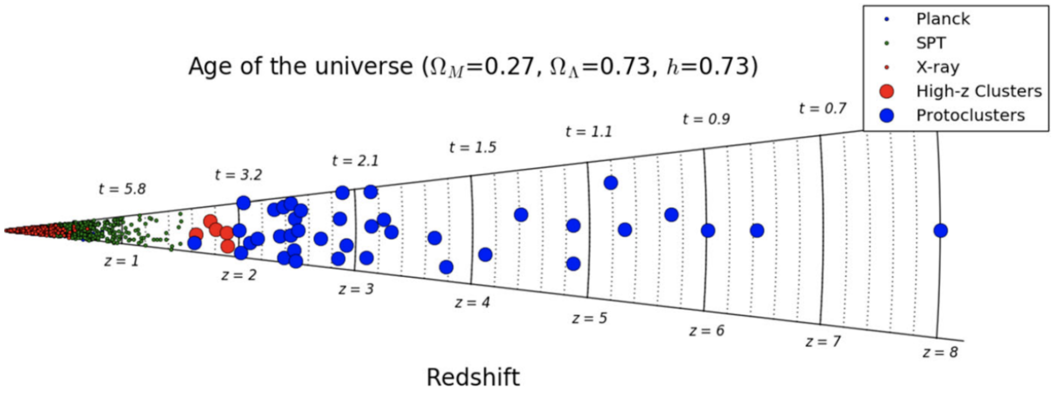

Figure 2 The distribution of redshifts of known protoclusters (blue points) taken from Overzier (2016). The local clusters are represented by black dots. Red points indicate high-z clusters at $z > 1.6$. The position of objects along the polar axis does not represent any information and is used for visibility purposes only.

regions. However, at higher redshifts $z \sim 4-5$, the stellar mass of cluster galaxies lie in a very similar range as in the field (Overzier et al., 2009). Thomas et al. (2005) showed that most star formation activity in the local early-type galaxies is expected to have occurred at $z \sim 3-5$ in overdense regions.

However, the number of known protoclusters at $z > 3$ is critically small ~ 10 (see Figure 2), which inhibits an in-depth understanding the galaxy formation history.

1.3 Detection of High-z Protoclusters

There are two methods for detecting such rare protoclusters.

The first is simply to detect the overdense regions of star-forming galaxies. These galaxies are essentially the only tracers which have been used to identify the galaxy overdense regions such as protoclusters at $z > 3$. Beyond $z = 3$, the detection of star-forming galaxies basically relies on two significant diagnostics on their spectral energy distributions (SEDs): the strong Lyman break on the continuum flux and the redshifted Lyα emission line. The radiation from a distant object is subjected to absorption due to intergalactic medium (IGM) along the line-of-sight direction during the travel of the light to earth. As a result, a continuum with a wavelength that is shorter than the redshifted Lyman alpha emission is significantly damped (Madau, 1995). The star-forming galaxies (SFGs) that are selected by photometrically detecting the continuum break are called Lyman break galaxies (LBGs) (see Figure 3). On the other hand, the Lyman alpha photons are mainly generated in star-forming regions and are easily scattered or absorbed by dust. They could escape from a young dust free galaxy. Such young galaxies can be selected by using a narrow band (in short, NB) filter that is matched to the wavelength of the Lyman alpha emission, and are referred to as LAEs (see Figure 4). Both characteristics can be used as promising approaching for the identification of high-z galaxies. By definition, LAEs can also be detected using the Lyman break method when their continuum fluxes are sufficiently bright, while LBGs include galaxy populations without Lyα emission. In the case of LBGs, the identification of the physical attributes that determine the presence or absence of their Lyα emissions is still an open question. Moreover, the physical and/or evolutionally connection is not yet clear. The typical stellar mass and age of LBGs are estimated to be $\sim 10^9 - 10^{11} M_\odot$ and 1Myr $-$2Gyr, respectively (Shapley et al., 2005), while the typical stellar mass and age of LAEs are $\sim 10^8 - 10^{10} M_\odot$ and $\sim$ 100Myr, respectively (e.g. Shimakawa et al., 2017).

The second method for the detection of protoclusters is based on the use of AGNs. The radio galaxy (RG), which is one of the AGNs in terms of the unified model of AGN (e.g. Urry & Padovani, 1995) (Figure 5), can be good tracer for high-z protoclusters even at $z > 3$. RGs are thought to appear via the Blandford-Znajek process (Blandford & Znajek, 1977). The torque of a global magnetic field terminated the rotation of SMBH. The rotational energy of the SMBH flows into the ambient magnetosphere, and then a radio jet is emitted via synchrotron radiation around the magnetic field. The energy of the radio emission can be expressed as $\propto M_{\rm BH} B_{\rm p} S$, where $M_{\rm BH}$ is a central black hole mass, $B_{\rm p}$ is the background poloidal magnetic field, and S expresses the spin of the black hole. Thus, RGs are expected to act as good signposts of galaxy overdense regions

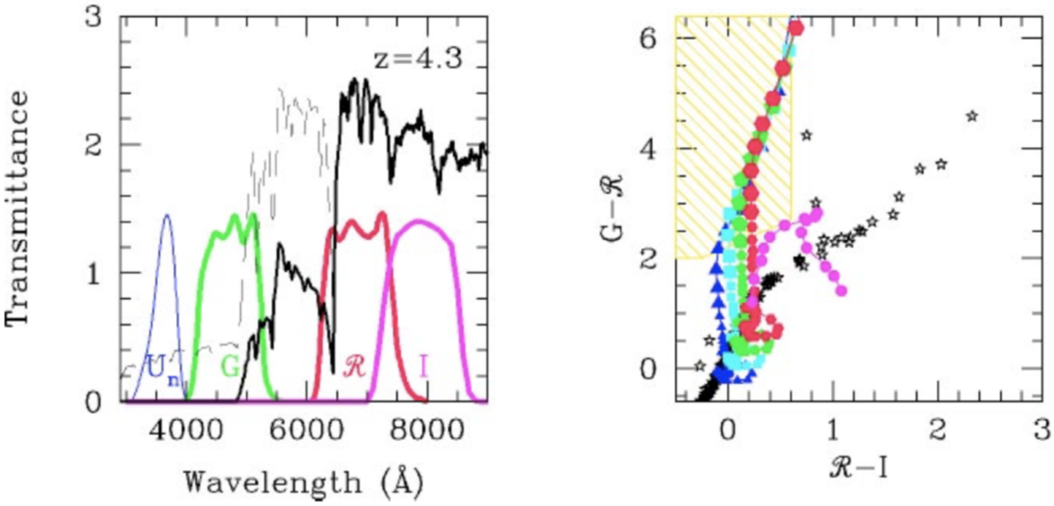

Figure 3 Example of the spectrum and color-color diagram of Lyman break galaxy taken from the part of Figure 1 in Giavalisco (2002). The left panel shows the spectrum of a star-forming galaxies at $z = 4.3$, observed from a frame of the Earth (black solid line). We can identify the galaxy by taking the colors of the discontinuous spectrum around the rest-frame wavelength of $1216\mathring{A}$, which is occurred by IGM absorption, using the filter sets of G-, R-, and I-bands which are drawn by green, red, and magenta lines, respectively. This galaxy have the red color of $G - R$ and the relatively bluer color of $R - I$, lying in the shaded area, which is the selection criteria of "Lyman break galaxy", in the right panel. Especially, the galaxy selected by the color selection is called "G-dropout galaxy" or simply, "G-dropout" because the flux observed in the G-band filter has "dropped out". The curves drawn in the color-color diagram show the redshift evolution tracks of the galaxies which have a continuous star-formation history starting at $z = 0.5$ with a step of $\Delta z = 0.1$. The four tracks have different dust extinction; $E(B-V) = 0$ (triangles), $E(B-V) = 0.15$ (squares), $E(B-V) = 0.3$ (pentagons), and $E(B-V) = 0.45$ (hexagons). The colors of stellar are shown by star symbols.

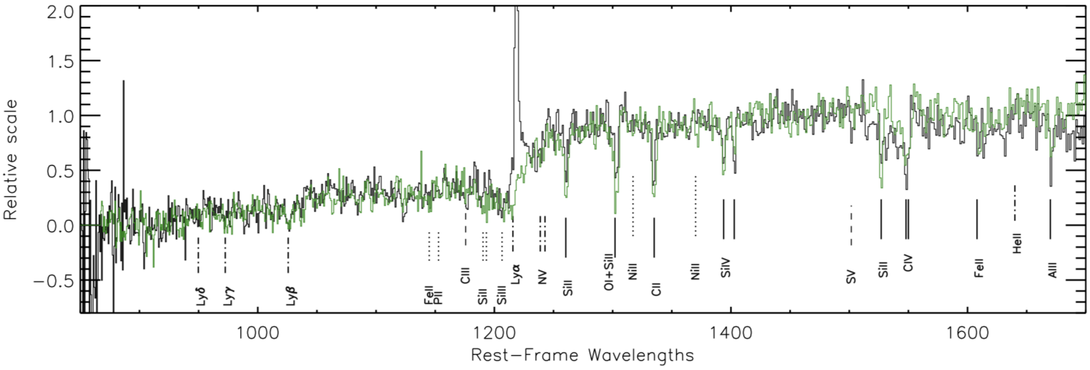

Figure 4 Example of the spectrum (black solid line) of Lyman alpha emitter taken from Lee et al. (2013). The spectrum is normalized at the wavelength of $1450\mathring{A}$.

because the SMBH mergers induced by galaxy mergers build up the black hole mass and the spin (Fanidakis et al., 2013). For instance, Kuiper et al. (2010) found the excess of the LAE and LBG density in the vicinity of RGs, MRC0316-257 at $z \sim 3.1$. Venemans et al. (2007) attempted to search for overdense regions of spectroscopically confirmed LAEs near RGs at $z \sim 2-5$. They concluded that at least six of eight RG fields reside in protoclusters. At $z \sim 4.1$, Saito et al. (2015) found that the RG TNJ1338, reside in the LAE overdense region.

A quasar, which is another type of AGN (Figure 5), is also expected to be a tracer of high-z protoclusters. This object is among the most luminous objects in the universe and is thought to form through major mergers of gas-rich galaxies (Kauffmann & Haehnelt, 2002) as shown in Figure 6, or cold streams (e.g. Dekel & Birnboim, 2006; Kereš et al., 2005; Ocvirk et al., 2008). Their typical bolometric luminosity of $\sim 10^{46}$erg/s can be achieved by releasing the huge gravitational energy of gas falling towards a central supermassive black hole (SMBH) which is expected to appear in the center of almost all galaxies. Therefore, it is expected that quasars preferentially reside in overdense regions where galaxy mergers occur frequently (Hopkins et al., 2008). The co-evolution of SMBHs and galaxies is supported by a tight correlation between the mass of central SMBHs and bulge stellar mass or velocity dispersion (Magorrian et al., 1998; Marconi & Hunt, 2003;

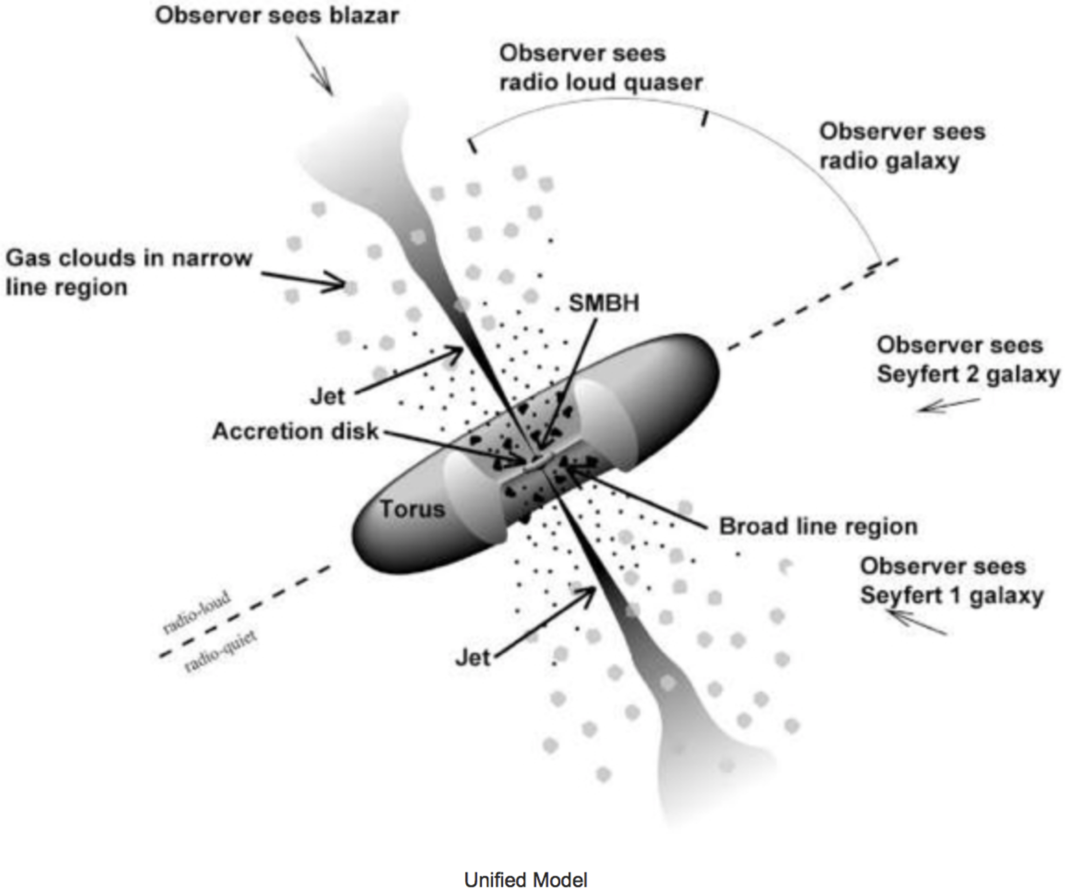

Figure 5 The unified model (or torus model) of AGN taken from the web page "https://fermi.gsfc.nasa.gov/science/eteu/agn/". The name of AGNs such as blazer, quasar, radio galaxy and so on, depends on the observer's orientation for the jet, the torus around the SMBH, and the accretion disk.

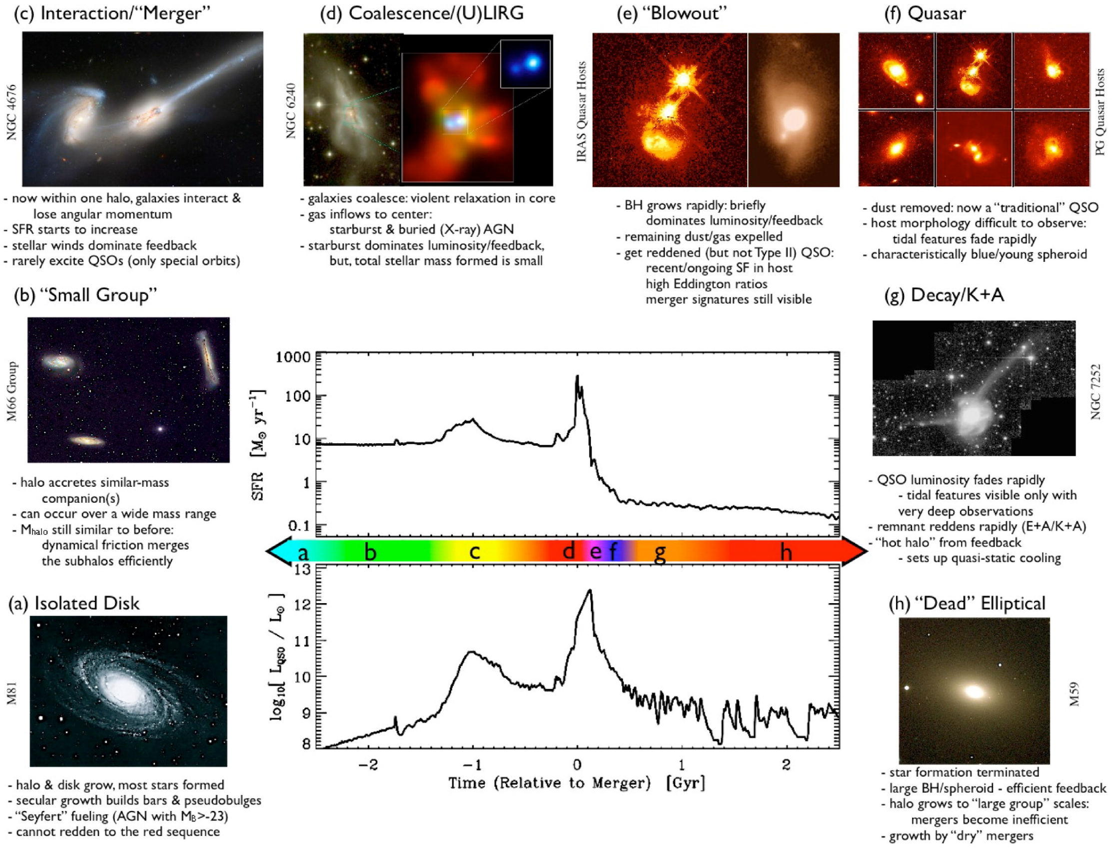
(c) Interaction/“Merger”

- now within one halo, galaxies interact & lose angular momentum
- SFR starts to increase
- stellar winds dominate feedback
- rarely excite QSOs (only special orbits)

(d) Coalescence/(U)LIRG

- galaxies coalesce: violent relaxation in core
- gas inflows to center: starburst & buried (X-ray) AGN
- starburst dominates luminosity/feedback, but, total stellar mass formed is small

(e) “Blowout”

- BH grows rapidly: briefly dominates luminosity/feedback
- remaining dust/gas expelled
- get reddened (but not Type II) QSO: recent/ongoing SF in host high Eddington ratios merger signatures still visible

(f) Quasar

- dust removed: now a “traditional” QSO
- host morphology difficult to observe: tidal features fade rapidly
- characteristically blue/young spheroid

(b) “Small Group”

- halo accretes similar-mass companion(s)
- can occur over a wide mass range
- M_{halo} still similar to before: dynamical friction merges the subhalos efficiently

(g) Decay/K+A

- QSO luminosity fades rapidly
  - tidal features visible only with very deep observations
- remnant reddens rapidly (E+A/K+A)
- “hot halo” from feedback
  - sets up quasi-static cooling

(a) Isolated Disk

- halo & disk grow, most stars formed
- secular growth builds bars & pseudobulges
- “Seyfert” fueling (AGN with M_B>-23)
- cannot redden to the red sequence

(h) “Dead” Elliptical

- star formation terminated
- large BH/spheroid - efficient feedback
- halo grows to “large group” scales: mergers become inefficient
- growth by “dry” mergers

Figure 6 The growth phases diagram taken from Hopkins et al. (2008) in a typical galaxy through a wet merger. Image credit: (a) NOAO/AURA/NSF; (b) REU program/NOAO/AURA/NSF; (c) NASA/STScI/ACS Science Team; (d) optical (left): NASA/STScI/R. P. van der Marel & J. Gerssen; X-ray (right): NASA/CXC/MPE/S. Komossa et al.; (e) left: J. Bahcall/M. Disney/NASA; right: Gemini Observatory/NSF/University of Hawaii Institute for Astronomy; (f) J. Bahcall/M. Disney/NASA; (g) F. Schweizer (CIW/DTM); (h) NOAO/AURA/NSF.

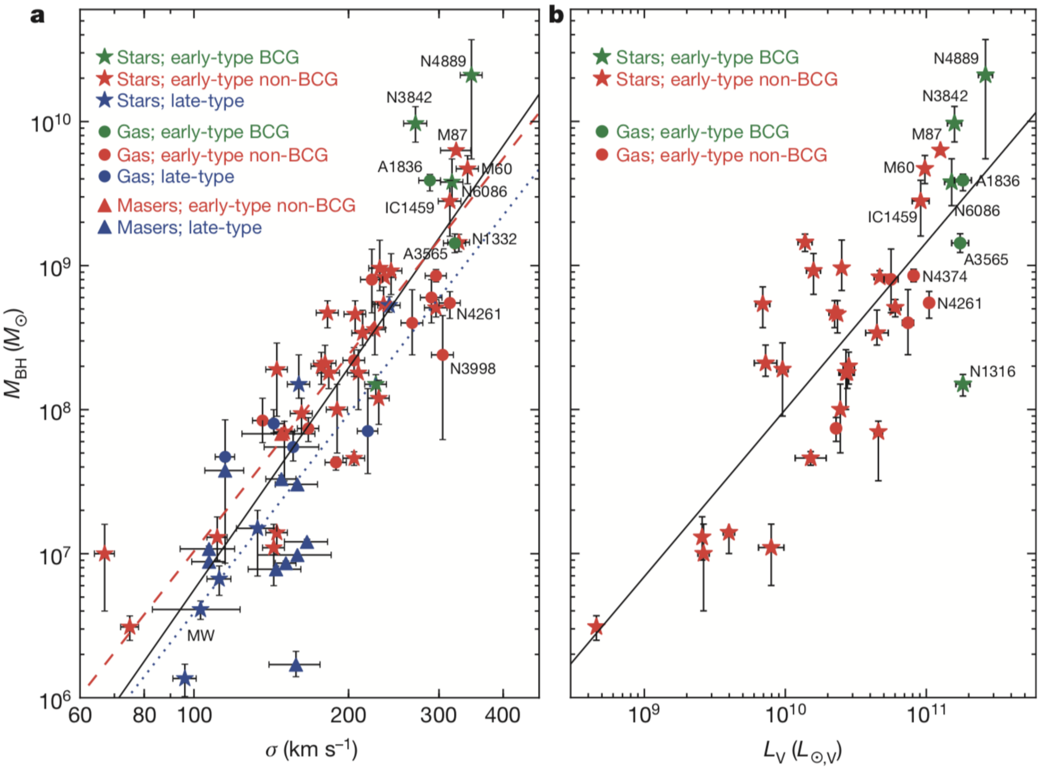

Figure 7 M-σ relation taken from McConnell et al. (2011). (a) The relation between blackhole mass and stellar velocity dispersion. (b) The relation between blackhole mass and V-band bulge luminosity.

McConnell et al., 2011) as shown in Figure 7, which is called M-σ relation. The underlying dark matter halo masses of quasar hosts have been statistically estimated using clustering analysis. The optically selected quasar halo masses at $z \sim 1-3$ are consistent with the typical halo mass of $\sim 10^{12}\ M_\odot$ at that epoch (Adelberger & Steidel, 2005; Coil et al., 2007; White et al., 2012), suggesting that they do not reside in very biased regions. In fact, Cai et al. (2016) recently found that the masses of protoclusters that are traced by Lyα forest absorption, $> 10^{13.7} M_\odot$, are much more massive than those of typical quasars at $z \sim 2-3$. However, at a higher redshift $z > 3$, Shen et al. (2007) showed that optical quasar halo masses are more massive with $M \sim (4-6) \times 10^{12}\ h^{-1} M_\odot$. This implies that almost all luminous quasars could be associated with cluster progenitors.

1.4 Co-evolution of quasars and galaxies

In spite of numerous previous investigations, an observational picture of the environment of high-z quasars is far from conclusive due to a high rarity of quasars and protoclusters, and the use of different depth, coverage, or definition of the surrounding environment in these studies (see Overzier, 2016, for a review), although quasars have been thought to act as signposts for high-z protoclusters as expected from the merger scenario and the massive halos of quasars (§1.3). For example, Husband et al. (2013) found that three luminous quasars at $z \sim 5$ reside in the overdense regions of LBGs. Morselli et al. (2014) identified more i-dropout galaxies in four $z \sim 6$ quasar fields compared to the numbers expected for a blank field. Adams et al. (2015) reported that approximately 10 % of a sample of luminous quasars at $z \sim 4$ reside in the overdense regions of LAEs. Recently, Kikuta et al. (2017) investigated quasar fields at $z \sim 4.9$ and suggested that high-z quasars are not associated with the extreme galaxy overdense regions of LAEs. Bañados et al. (2013) and Mazzucchelli et al. (2017) used deep narrow- and broad-band (in short, BB) imaging to study the environment of $z \sim 5.7$ quasars and did not find any enhancement of LAEs compared with average fields. This implies that either high-z quasars may not trace the most massive dark matter halos, or galaxy merger is not a predominant physics to trigger quasar activity. Trainor & Steidel

(2012) showed that hyper luminous quasars reside in galaxy overdense regions, but the environment around them is not very different from that around much less luminous quasars.

Moreover, there is another aspect that makes it difficult to evaluate the quasar environment. The most luminous quasars could suppress galaxy formation in their surroundings through feedback, “photoevaporation” (see §1.4), even if some of these quasars reside in very massive dark matter halos. The quasar photoevaporation effect, which is expected from numerical simulation (e.g. Barkana & Loeb, 1999), evaporates the collapsed gas in the halo and further inhibit gas cooling by photoionization heating due to the intense ultraviolet (UV) background radiation associated with the quasars. This large-scale radiative feedback should be inefficient for bright ($L > L_*$) galaxies residing in deep potential wells, but may heavily suppress star formation in lower mass objects (Benson et al., 2002) as shown in Figure 8. After the reionization epoch, low-luminosity galaxies can form in the general field only if there are no strong UV ionizing sources such as nearby quasars. Consequently, it is expected that the luminosity function of galaxies in the vicinity of quasars should be flatter than that of the general field population as shown in Figure 8.

The low-mass galaxies in the vicinity of quasars need to be observed to detect the quasar photoevaporation effect. For example, Kashikawa et al. (2007) performed a survey for both LBGs and LAEs around a quasar, Sloan Digital Sky Survey (SDSS) J0210-0018 at $z = 4.8$. They found that LBGs formed a filamentary structure including the quasar, while LAEs were distributed in a ring-like structure around the quasar, avoiding its immediate vicinity within a distance of ~ 4.5 comoving Mpc (cMpc) where the local UV background radiation could be ~ 100 times stronger than the average for the epoch. This clustering segregation could be caused by photoevaporation resulting in a deficit of lower mass LAEs in the vicinity of intense UV sources. LAEs are young galaxies with low dust content and relatively low stellar mass (Shapley et al., 2001); therefore, they are particularly prone to photoevaporation in the vicinity of intense radiation sources such as quasars. Recently, Ota et al. (2018) found a quasar residing in a low-density

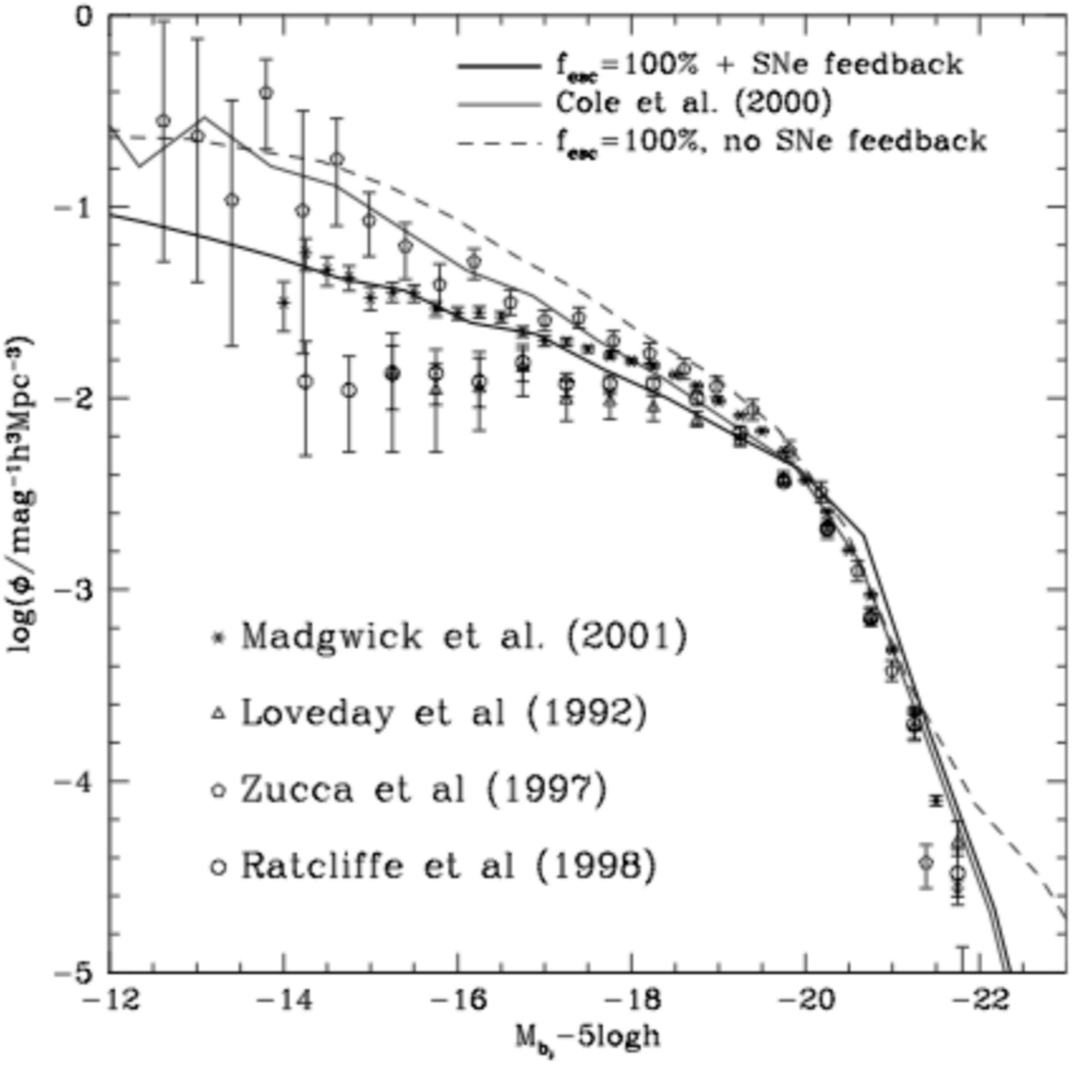

Figure 8 Photoevaporation effect taken from Benson et al. (2002). This figure shows the b_J-band galaxy luminosity function at $z = 0$ for UV sources (thick solid line) and without sources (dashed line).

region of LAEs at $z = 6.6$, while Kikuta et al. (2017) investigated the distribution of LAEs in the vicinity of two quasars and a radio galaxy at $z \sim 4.9$ and did not find evidence of the quasar photoevaporation.

However, these previous studies at $z \sim 5-6$ are not sufficiently deep to probe galaxies with appropriately low luminosity ($\mathrm{M_{UV}} > -20.5$) or low mass ($M_{\rm vir} < 10^{10} M_\odot$), where more effective photoevaporation is expected. In addition, the small sample sizes did not allow us to derive a general picture of this effect in the vicinity of high-z quasars.

1.5 This thesis

In this thesis, I attempted to systemically and quantitatively characterize the environment of high-z quasars in order to obtain a better understanding of the global history of our universe by answering the two non-clear points (1) In what environments quasars exist and (2) How much influence quasar photoevaporation effects have on surrounding galaxies. The previous difficulties in answering these two questions and the approach for overcoming these difficulties in the study are summarized as follows.

1. In what environment do quasars exist?

   It has been difficult to examine the relation between quasars and their environments systematically. From the above, high-z quasars are expected to preferentially appear in protoclusters according to the merger scenario and M-σ relation. However, until recently, the number of known protoclusters at $z > 3$ has been very small, ~ 10 (Chiang et al., 2013). A direct technique to detect nearby clusters by searching for thermal X-ray emission from intra-cluster medium (Böhringer et al., 2001) is insensitive at $z > 2$, where clusters are expected to be in a growing phase. Furthermore, strong radiation from quasars may provide negative feedback, which may suppress nearby galaxy formation (see §1.4). This will cause a significant bias when using the protocluster sample selected using these signposts.

Therefore, it is necessary to find more protoclusters in blank field for expanding systematic studies toward $z \gtrsim 3$. I utilized the Hyper Suprime-Cam (HSC; Miyazaki et al., 2012), which is an unprecedented wide-field imaging instrument mounted on the 8.2 m Subaru telescope to build the largest sample of $z \sim 4$ protoclusters to date (Toshikawa et al., 2018). The new protocluster sample was constructed from the data of the Strategic Program for the Subaru Telescope (HSC-SSP : P.I. Miyazaki), that is currently on-going. Figure 9 shows the survey area of the 1st release data (DR1) of HSC-SSP (Aihara et al., 2018). See §2.1.1 for more information. The bias-free wide-field protocluster survey allows us to investigate the general relationship between quasars and protoclusters, which will help us to verify the merger scenario which activate quasars and to understand the early interplay between structure formation, galaxy, and SMBH co-evolution.

In this thesis, I used the DR1 of HSC-SSP of $\sim$121 square degrees to statistically characterize the environment of a large number of optically selected quasars at $z \sim 3.8$ from the SDSS. This was achieved by measuring their typical environmental density and the cross-correlation with the protocluster catalog at the same redshift.

2. How much influence do quasar photoevaporation effects have on surrounding galaxies?

   From the above, the previous studies did not observe sufficiently deep to probe galaxies with appropriately low luminosity or equivalently, low mass, where more effective photoevaporation is expected. In addition, the small sample size and FOV (Field of View) did not allow for the derivation of a general picture of this effect in the vicinity of high-z quasars.

   Thus, wide field imaging with a Suprime-Cam mounted on the 8.2 m Subaru telescope was performed. A total of 11 fields were targeted, that were expected to be affected by a strong local UV background from quasars at $z = 2 - 3$, in order to study the radiative feedback effect on the surrounding low-luminosity galaxies systematically. The combination of NB imaging with

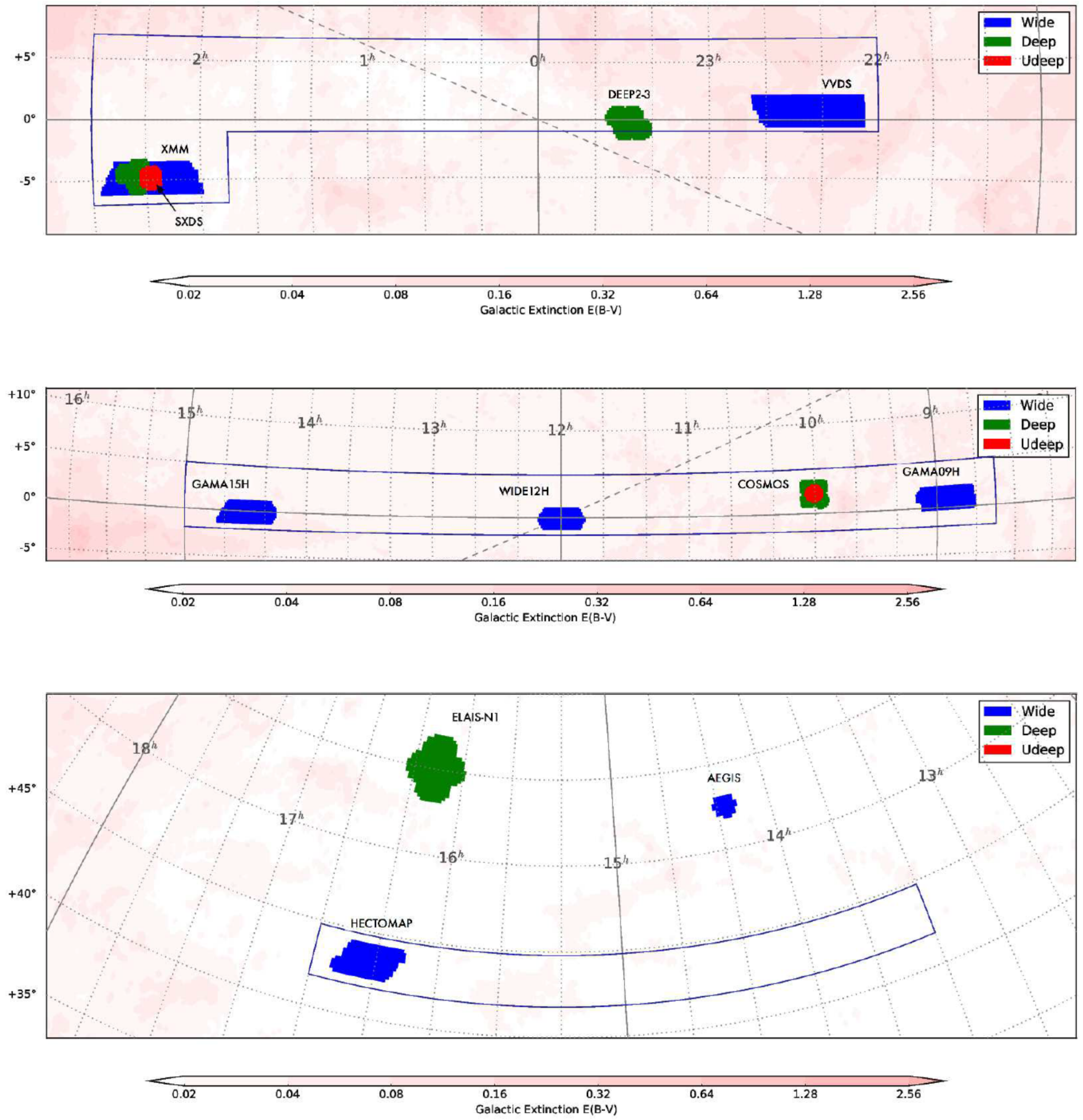

Figure 9 Survey area of HSC-SSP acquired from Aihara et al. (2018). The Wide-, Deep-, and Ultra Deep-layers which have already been observed in the DR1 of HSC-SSP, are represented by blue, green, and red areas, respectively. The boxes show the wide survey region which will be observed in the future.

deep BB imaging can effectively isolate LAEs at $z = 2 - 3$ (Venemans et al., 2005), down to a low luminosity of $M^{*}_{\mathrm{UV,z=3}} + 2.0 \sim -15$, which is 1.5 magnitudes deeper than the previous study at $z > 4$.

This thesis is organized as follows. In §2, I characterized the environment of quasars. Firstly, the protocluster sample is described in the HSC-Wide layer, in addition to the SDSS quasar sample. The correlation between protoclusters and quasars is investigated, and the idea of whether or not quasars are statistically good indicators of protoclusters is discussed. I further examine the average radial density profile around quasars on the small scale using a stacking analysis, in addition to its dependence on quasar luminosity and black hole mass. In §3, I examine quasar photoevaporation feedback. The selection and reduction of targeted quasar fields are described in addition to the construction of the LAE sample. The LAE galaxy density in the vicinity of the quasars was also investigated, in addition to a search for the correlation between the galaxy density, the properties of the LAEs and the quasars (e.g. black hole mass and luminosity). In §4, I summarize and discuss our findings. Finally, future works are given.

The following cosmological parameters were assumed in this investigation: $\Omega_M = 0.3$, $\Omega_\Lambda = 0.7$, $H_0 = 70$ km s^{-1} Mpc^{-1}, and magnitudes are given in the AB system.

Chapter 2 Correlation between QSOs and Protoclusters at $z \sim 4$

In this chapter, the DR1 of HSC-SSP of $\sim$ 121 square degrees was used to statistically characterize the environment of a large number of optically selected quasars at $z \sim 3.8$ from the SDSS. This was performed by measuring their typical environmental density and the cross-correlation with the protocluster catalog at the same redshift. In §2.1, the protocluster sample in the HSC-Wide layer, and our SDSS quasar sample are described. In §2.2, the correlation between protoclusters and quasars is examined, and whether quasars are statistically good indicators of protoclusters or not is discussed. Furthermore, the average radial density profile around quasars on the small scale using a stacking analysis, and its dependence on quasar properties are examined. The implications of our results are discussed in §2.3.

2.1 DATA AND SAMPLE SELECTION

2.1.1 The Subaru HSC-SSP survey

The Subaru HSC-SSP survey started in early 2014 and will spend 300 nights until completion by 2019 or 2020. The HSC is equipped with 116 2K × 4K Hamamatsu fully-depleted CCDs, of which 104 CCDs are used to obtain science data over a FoV of with a diameter of 1.5 deg. The present thesis is based on the so-called wide layer of the HSC-SSP, which has a wide-area coverage. In the future, the survey area will be increased to $\sim$ 1400 deg^2. Moreover, high sensitivity will be achieved using five optical (g, r, i, z, y) bands whose transmission curves are represented in Figure 10. The total exposure times range from 10 min in the g and r bands to 20 min in the i, z, and y bands. The expected 5σ limiting magnitudes for point sources are (g, r, i, z, y) = (26.5, 26.1, 25.9, 25.1, 24.4) mag measured in 2.0arcsec apertures. It is expected that $>$ 1400 protocluster candidates will be

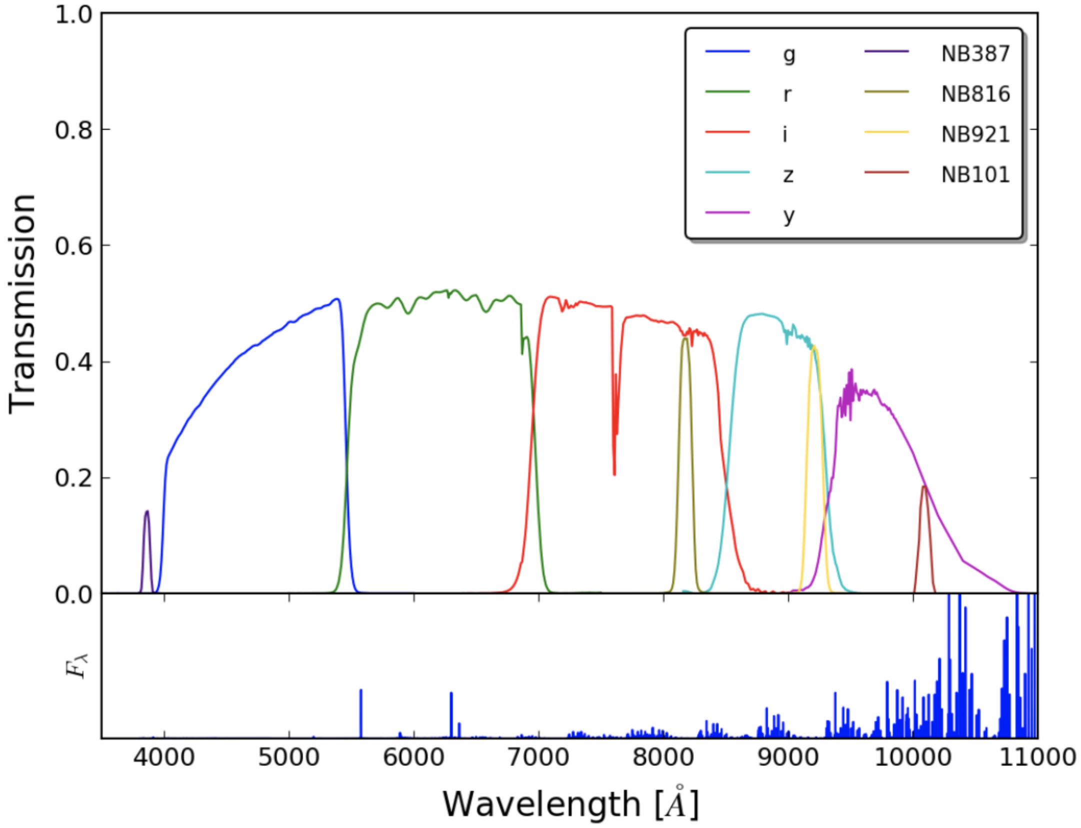

Figure 10 The bandpasses of HSC-SSP taken from Aihara et al. (2018). They are included the CCD response, the reflectivity of all mirrors, and transmission of all optics, filters, and the atmosphere. The lower panel shows the spectrum of sky emission.

obtained at $z \sim 4$ by the end of the survey (Toshikawa et al., 2018, 2016). The HSC data (DR S16A, Aihara et al., 2018), which includes data taken before April 2016, has already produced an extremely wide field image of > 200 deg^2 with a median seeing size of $0.6 - 0.8$ arcsec in the wide layer. The survey design is shown in Aihara et al. (2018). The filter information is given in Kawanomoto et al. (2018). Data reduction was performed with the dedicated pipeline hscPipe (version 4.0.2, Bosch et al., 2018), a modified version of the Large Synoptic Survey Telescope software stack (Ivezic et al., 2008; Axelrod et al., 2010; Jurić et al., 2015). The astrometric and photometric calibrations are associated with the Pan-STARRS1 system (Schlafly et al., 2012; Tonry et al., 2012; Magnier et al., 2013). I use the cModel magnitude [1], which is measured by fitting two-component PSF-convolved galaxy models (de Vaucouleurs and exponential) to the source profile (Abazajian et al., 2004). The fluxes and colors of the sources were measured using the cModel.

Table 1 Details of the five fields included in the HSC-SSP Data Release S16A used in this analysis.

Name	range in R.A. (J2000)	range in Decl. (J2000)	effective area [deg^2]
W-XMMLSS	$1^h36^m00^s$ to $3^h00^m00^s$	$-6°00'00''$ to $-2°00'00''$	31.26
W-Wide12H	$11^h40^m00^s$ to $12^h20^m00^s$	$-2°00'00''$ to $2°00'00''$	17.00
W-GAMA15H	$14^h00^m00^s$ to $15^h00^m00^s$	$-2°00'00''$ to $2°00'00''$	39.27
W-HECTMAP	$15^h00^m00^s$ to $17^h00^m00^s$	$42°00'00''$ to $45°00'00''$	12.60
W-VVDS	$22^h00^m00^s$ to $23^h20^m00^s$	$-2°00'00''$ to $3°00'00''$	20.73

2.1.2 HSC protocluster sample

The new large survey for high-redshift protoclusters based on the unprecedented imaging data produced by the HSC-SSP survey is ongoing. The catalog of protocluster candidates at $z \sim 4$ is described in Toshikawa et al. (2018). I will briefly review the key steps of the construction of the protocluster catalog in this section.

---

[1] https://www.sdss.org/dr12/algorithms/magnitudes/#cmodel

At first, the g-dropout galaxies are selected from 5 independent fields in HSC-SSP S16A DR (i.e. W-XMMLSS, W-Wide12H, W-GAMA15H, W-HECTMAP, and W-VVDS ; see Table 1) , using the following LBG criteria as given in van der Burg et al. (2010) :

$$
\begin{aligned}
1.0 &< g - r, && (2)\\
r - i &< 1.0, && (3)\\
1.5(r - i) &< (g - r) - 0.80, && (4)\\
r &\leq m_{\mathrm{lim},3\sigma}, && (5)\\
i &\leq m_{\mathrm{lim},5\sigma}, && (6)
\end{aligned}
$$

where $m_{\mathrm{lim},3\sigma}$ and $m_{\mathrm{lim},5\sigma}$ are 3σ and 5σ limiting magnitude, respectively. If the objects were not detected in the g-band filter at 3σ, their g-band magnitudes were replaced by the corresponding 3σ limiting magnitudes. Only homogeneous depth regions are used, where the limiting magnitudes reach those expected in all g-, r-, and i-bands. The regions around bright objects are carefully masked. The effective areas are summarized in Table 1. The total effective area achieved was 121 square degrees. In this area, 259,755 g-dropouts down to $i < 25.0$ were obtained. This number count is consistent with that of van der Burg et al. (2010). The redshift distribution of g-dropout galaxies is expected to be the almost same as that of van der Burg et al. (2010) based on the same color criteria.

Next, the fixed aperture method was applied to estimate the surface density contour maps of g-dropout galaxies. Apertures with radius of 1.8 arcmin, which corresponds to 0.75 physical Mpc (pMpc) at $z \sim 3.8$, were distributed in the sky of HSC-Wide layer. This aperture size is comparable with the typical protocluster size at this epoch with a descendant halo mass of $\gtrsim 10^{14}\ M_{\odot}$ at $z = 0$ (Chiang et al., 2013). To evaluate the overdensity significance quantitatively, we estimated the local surface number density by counting galaxies within the fixed aperture. The overdensity significance is defined by $(N\text{-}\bar{N})/\sigma$, where N is the number of the g-dropout galaxies in an aperture, and $\bar{N}$ and σ are average and standard deviation of N, respectively. Red galaxies at intermediate redshifts and dwarf stars could satisfy the color selection criteria when their photometric errors are large. The fraction of contamination from these objects in the g-dropout color selection is evaluated to be 25% at most at $i < 25.0$ (Ono et al., 2018), 20% of which originates in photometric error (Toshikawa et al., 2016). The overdensity significance should not be largely affected by the contamination.

The final protocluster candidates were selected from those regions that had overdensities with $> 4\sigma$ significance. Although there is a large scatter due to projection effects, surface overdensity significance is closely correlated with descendant halo mass at $z = 0$. Toshikawa et al. (2016) showed that $>$ 76% of $> 4\sigma$ overdense regions of g-dropouts are expected to evolve into dark matter halos with masses of $> 10^{14}\ M_\odot$ at $z = 0$, although there is no clear difference of the halo masses between $< 4\sigma$ overdense regions and fields due to a large scatter. It should be noted that the success rate of this technique has already been established by the previous study of the ~ 4 deg^2 of the Canada-France-Hawaii Telescope Legacy Survey (CFHTLS) Deep Fields, as the precursor of this HSC protocluster search, followed by Keck/DEep Imaging Multi-Object Spectrograph (DEIMOS) and Subaru/Faint Object Camera and Spectrograph (FOCAS) spectroscopy (Toshikawa et al., 2016). Each $> 4\sigma$ overdense region was carefully checked and 22 false detections of mainly spiral arms of local galaxies were removed. As a result, 179 protocluster candidates were identified at $z \sim 3.8$ in the HSC-Wide layer with overdensity significance ranging from 4 to 10σ (Figure 12). Figure 11 shows the histogram of the overdensity significance of the protocluster candidates.

Note that the redshift range of a g-dropout galaxy is expected to be $\sim$ 60pMpc (Ono et al., 2018), meaning that the $> 4\sigma$ overdense region corresponds to an extreme system with a > 10 times higher density than average in the typical protocluster scale of 1.5pMpc at $z \sim 4$. The $z = 0$ average descendant halo masses of the $z \sim 4$ protoclusters are estimated to be $\sim 3 \times 10^{14} M_\odot$ (Toshikawa et al., 2016), corresponding to the Virgo cluster mass. The overdensity of the Virgo cluster in the scale of a few Mpc is ~ 30 (Davis et al., 1980) which is consistent with that of the $z \sim 4$ protoclusters.

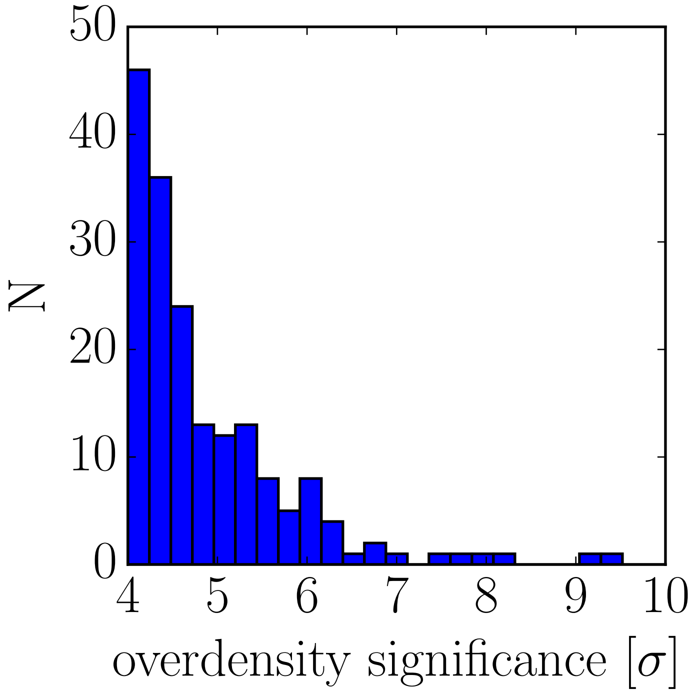

Figure 11 Histogram of overdensity significance of the 179 protocluster candidates from Toshikawa et al. (2018). The horizontal axis shows the significance of the overdensities of g-dropout galaxies measured within 1.8 arcmin radius circular apertures across the HSC-SSP Wide layer. The maximum significance is 9.37.

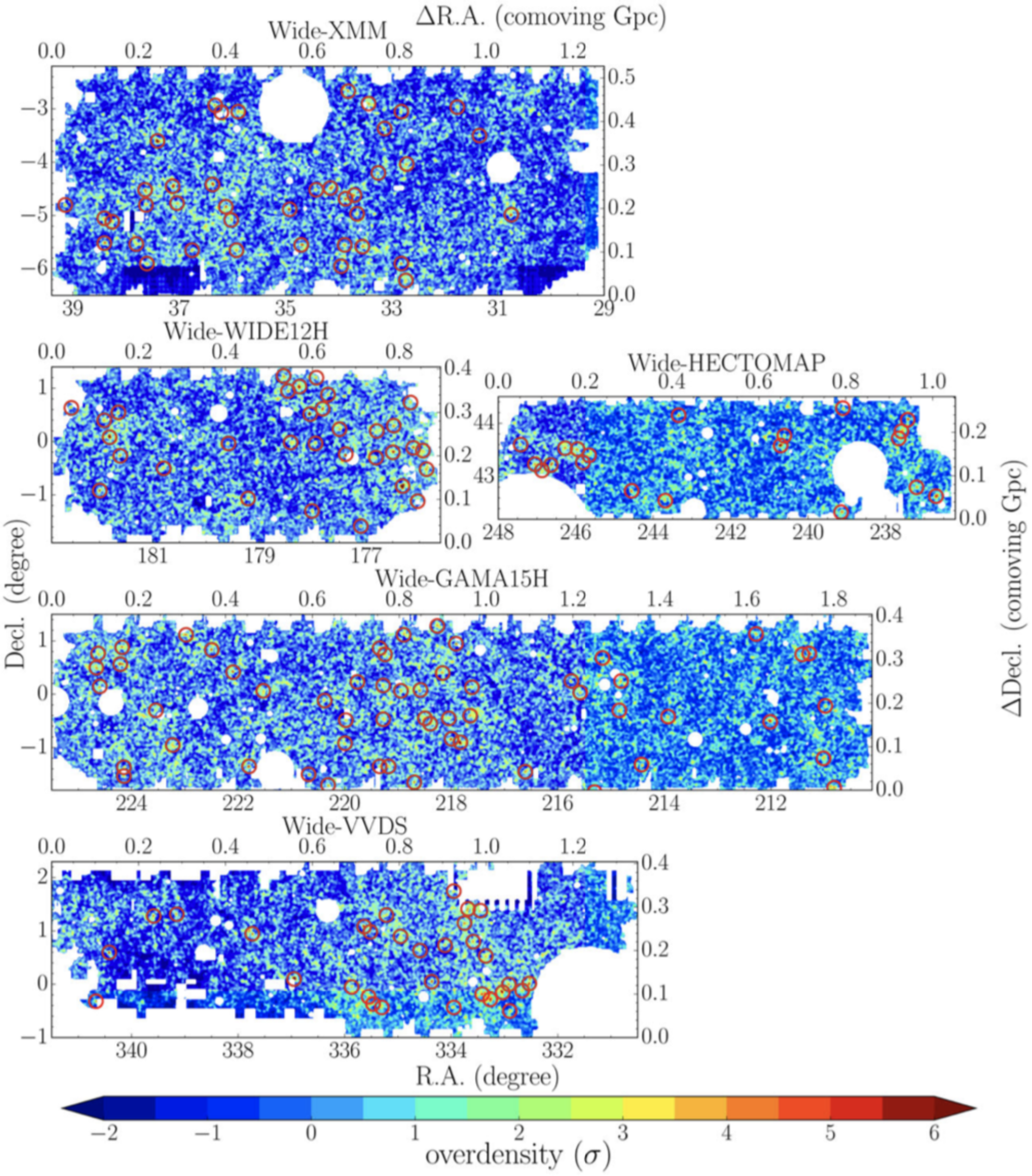

Figure 12 Overdensity maps in the HSC-Wide layer taken from Toshikawa et al. (2018). The color contours indicate the overdensity significance. The positions of 179 protoclusters are represented by the red circles.

2.1.3 Quasars

The quasar sample was extracted from the SDSS quasar catalog of Pâris et al. (2017) based on SDSS DR12. The SDSS-DR12 quasar catalog is the final SDSS-III quasar catalog. It contains $297,301$ spectroscopically confirmed quasars over a wide redshift range of $0.041 < z < 6.440$ in the area covering approximately $10,200$ deg^2 of the sky. The quasars have been selected from three different observational programs: 1) the Baryon Oscillation Spectroscopic Survey (BOSS; Dawson et al., 2013), 2) ancillary programs such as the SDSS-IV pilot survey, and 3) objects targeted by chance in other programs, such as the luminous galaxy survey. For the details of target selection for spectroscopic observation and quasar confirmation, please see Ross et al. (2012). Within the g-dropout redshift range of $z = 3.3 - 4.2$ which corresponds to the g-dropout selection function with a value over 0.4 (Ono et al., 2018), 151 quasars were found in the effective areas of the HSC-Wide layer. The i-band absolute magnitudes of this sample range from ~ -29 to -26 (see Figure 19). I use the reduced one-dimensional (1D) spectral data of the quasars, that are available through the SDSS Science Archive Server (SAS) to estimate the black hole masses for this sample (§3.3). The spectral resolution was $R \sim 1300 - 2500$ (Pâris et al., 2017). If the quasars have a match in the FIRST radio catalog (Becker et al., 1995), whose detection limit is 1 mJy within 2.0 arcsec, the "FIRST_MATCHED" flag in the SDSS DR12 catalog is set to 1 (Pâris et al., 2017). The sample contains 8 FIRST- detected quasars (FIRST_MATCHED = 1) with strong radio emission of $L_\nu(6.74\mathrm{GHz}) > 5.0 \times 10^{32}$ erg s^{-1} Hz^{-1}, which is approximately 10 times larger than that of a dichotomy between star-forming galaxies and radioactive AGNs (Magliocchetti et al., 2002; Mauch & Sadler, 2007). It should be noted that the radio property of AGNs affect clustering strength (Donoso et al., 2010).

2.2 RESULTS

2.2.1 Cross-correlation between protoclusters and quasars

At first, the projected distance from the quasars to the nearest protoclusters was measured to find whether the two populations are related. The results are shown in Figure 13. The blue histogram shows the angular separations between quasars

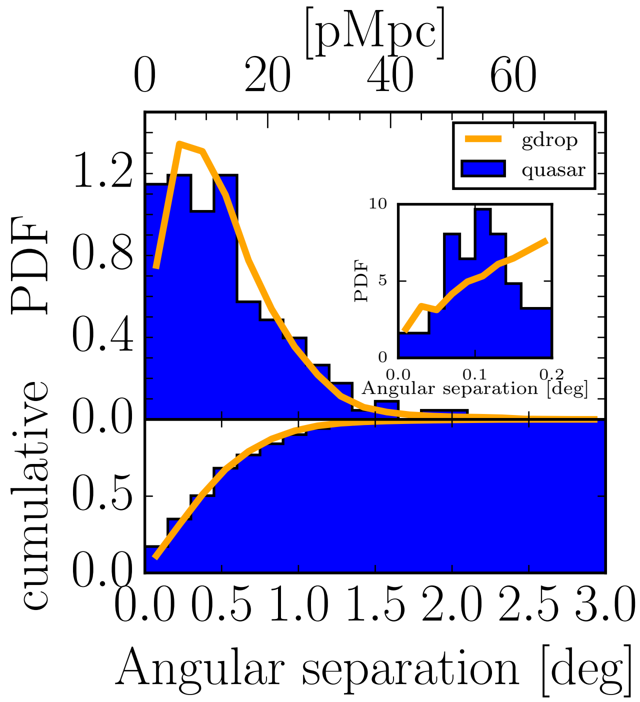

Figure 13 Histogram of distance from quasars and g-dropouts to the nearest protocluster candidates. The blue rods represent the case of quasars and the red line indicate the case of all g-dropout galaxies. The vertical axis shows the probability distribution function (PDF) and the cumulative PDF. The small chart shows the PDF in the region limited to the small scales, < 0.2 deg.

and protoclusters, while the orange line represents the separations between g-dropout galaxies and protoclusters. The P-value of the Kolmogorov-Smirnov (KS) test between the two distributions is 0.573. This indicates that they are not significantly different, at least on these scales. I also focused on the smaller scale < 0.2 degrees to conduct a similar analysis (see small chart in Figure 13). However, the result does not change: the P-value in the KS test is 0.100.

To measure the environments in detail, I also measured the overdensity significances at the exact locations of the quasars. The maximum overdensity significance within a circle of radius $a = 1$ arcmin (2.5 comoving Mpc; cMpc) was also measured because it is known that quasars and radio galaxies at these redshifts are not always at the center of the overdense regions (e.g. Venemans et al., 2007). Figure 14 (a) shows the probability distribution of the nearest maximum overdensity significance of quasars and random points, which are uniformly distributed in the exactly same area as the protocluster survey area, within a circle of radius $a = 1$ arcmin. It was found that the quasars tend to reside in galaxy denser regions than the random points with $\sim 1.5\sigma$ significance. This means the signal of the clustering of the quasars. The probability distribution of the nearest maximum overdensity significance of quasars and g-dropouts is shown in Figure 15 (a). It was found that only two quasars coincide with protocluster candidates. These protoclusters have overdensity significances of 4.51σ and 4.56σ and are represented in Figure 16. It is interestingly to note that one of these protoclusters has two nearby quasars ("quasar pair") at the same redshift of $z \approx 3.6$. These systems are discussed in detail in Onoue et al. (2018). The typical radius of protoclusters with $M_{z=0} \gtrsim 10^{14}\ M_{\odot}$ is $\gtrsim 1.8$ arcmin at $z = 4$ (Chiang et al., 2013); therefore, I also checked the distributions of the maximum overdensity significance found within a circle of radius $a = 3$ and $a = 10$ arcmin centered on the quasars, shown in panel (b) and panel (c) of Figure 14 and 15, respectively. I also compared the distribution of the overdensity found for quasars with that found for random points and g-dropouts. The quasars also tend to exist in galaxy denser regions than the random points with $\sim 1.2 - 1.5\sigma$ significance. The distributions of the quasars and g-dropouts are statistically similar at all scales and the results are summarized in Table 2.

It is expected that the shape of the redshift distribution of the quasars would not be exactly the same as that of the g-dropout galaxies. Therefore, the examined correlations may be diluted by the slight differences in the redshift of these samples. Nonetheless, it was confirmed that the results did not change even if 80 quasars at $z = 3.5 - 4.0$ were extracted or quasars that satisfy the exact same selection criteria (7) - (6) of the g-dropouts were selected. This result is robust even if extraction is performed only for the overdense regions with $> 5\sigma$ to enhance the purity of the

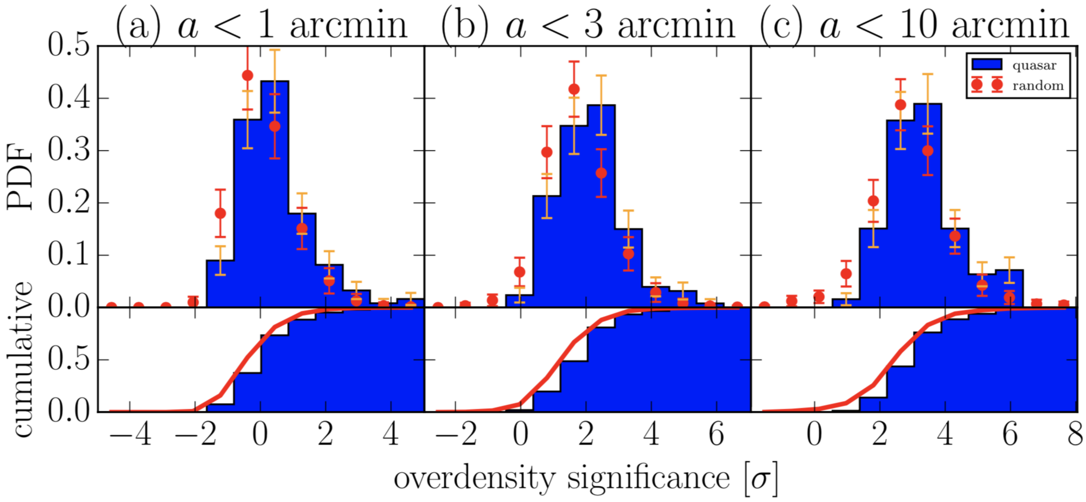

Figure 14 Histogram of overdensity significance of quasars (blue histogram) and random points (red points). The panels (a), (b) and (c) show the histograms of the maximum overdensity significance centered on quasars and random points with radii of 1 (0.42), 3 (1.25), and 10 (4.2) arcmin (pMpc), respectively. The vertical axis shows the probability distribution function (PDF) and the cumulative PDF. The realization of the random points is 100. The error bar of the quasar distribution is assumed to obey the Poisson distribution. On the other hand, the error of the random points is the standard deviation of the realization.

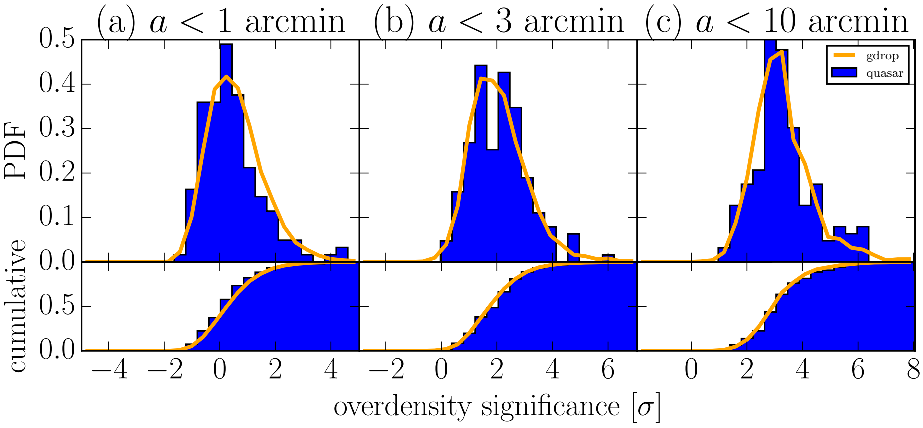

Figure 15 Histogram of overdensity significance of quasars (blue histograms) and g-dropouts (orange lines). The panels (a), (b) and (c) show the histograms of the maximum overdensity significance centered on quasars and g-dropouts with radii of 1 (0.42), 3 (1.25), and 10 (4.2) arcmin (pMpc), respectively. The vertical axis shows the probability distribution function (PDF) and the cumulative PDF.

sample: the P-value of the KS test between their distributions is 0.437, and when focusing on the smaller scale < 0.2 degree, the P-value is 0.67.

2.2.2 Stacked densities around quasars

In Figure 15, the overdensity significance distributions around the quasars are discontinuously examined only on 1, 3, and 10 arcmin scales. In order to investigate the continuous overdensity significance maps around the quasars, the median stacked overdensity significance map around all quasars and g-dropout galaxies (Figure 17) were measured. Each galaxy overdensity significance map has a 1 arcmin spatial resolution that was estimated from the fixed apertures with a radius of 1.8 arcmin. Here, to compare their environments in a non-biased manner, the quasars that are also g-dropouts were counted only once. The panels (a) and (b) show the overdensity significance map in the vicinity of quasars and g-dropouts, respectively. The g-dropout galaxies that were used to create these maps are the same as those used to define the overdensity significance. The variance of

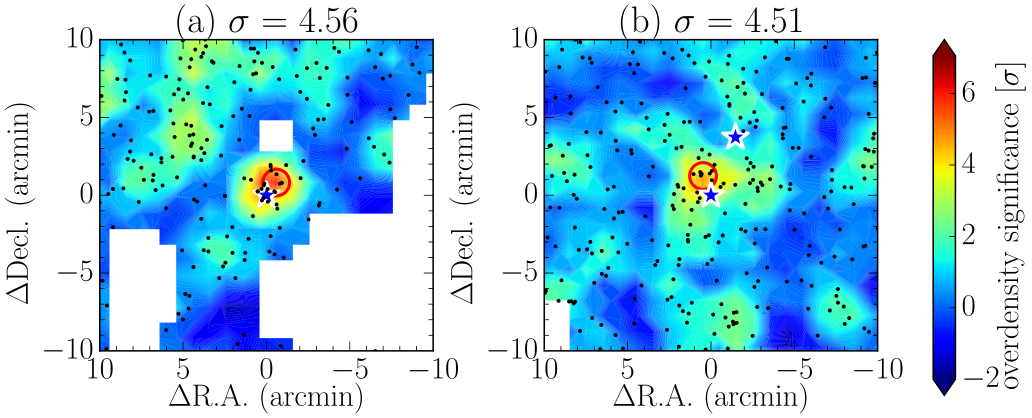

Figure 16 The two quasars found within 1 arcmin (0.42 pMpc) of a protocluster candidate. The quasars are represented by the blue star symbols. The quasar in the center of each panel lies near a $> 4\sigma$ maximum overdensity significance region of $\sigma = 4.56$ and 4.51 in panel (a) and (b), respectively. The color contours show the overdensity significance map and the red circle shows the local maximum of the region. The black dots show the g-dropout galaxies and the mask regions are represented by the white regions. The size of each panel is 20 arcmin × 20 arcmin. The quasar pair at $z \approx 3.6$ from Onoue et al. (2018) is represented in the panel (b).

Table 2 Statistical Tests of the Correlation of the separations between Quasars and Protoclusters, and g-dropouts and Protoclusters shown in Figures 13 and 15.

	KS P-value
Figure 13	0.573
Figure 15 (within 1 arcmin)	0.105
Figure 15 (within 3 arcmin)	0.645
Figure 15 (within 10 arcmin)	0.712

the stacked map seen in the quasar field is consistent with that of 151 randomly selected g-dropouts.

To more clearly illustrate the difference, Figure 18 shows the radial profile of the median stacked overdensity significance maps of Figure 17. The blue (green) points show the median densities within a circular ring with a width of 1 arcmin in the case of quasars (g-dropouts). The error bars show the standard error of the mean. An interesting structure is identified: the average density around quasars is slightly higher than that of g-dropout galaxies in the $1.0 - 2.5$ pMpc-scale environment at the level of several sigma, while on the smaller-scale environment, < 0.5 pMpc, that of quasars is lower by approximately one sigma.

2.2.3 Photometric properties of quasars in overdense regions

A check was performed to identify differences between the luminosities of quasars inside and outside the overdense regions. Figure 19 shows the relation between the ambient overdense significances and the i-band absolute magnitudes of the quasars, which correspond to their rest-UV luminosity at this redshift. The absolute magnitudes are estimated from the visual inspection redshift of each quasar in the SDSS DR12 catalog, 'Z_VI'. The panels (a), (b) and (c) show the cases of maximum overdensity significance within the circles of radii 1, 3 and 10 arcmin centered on the quasars, respectively. To show whether the quasar sample is

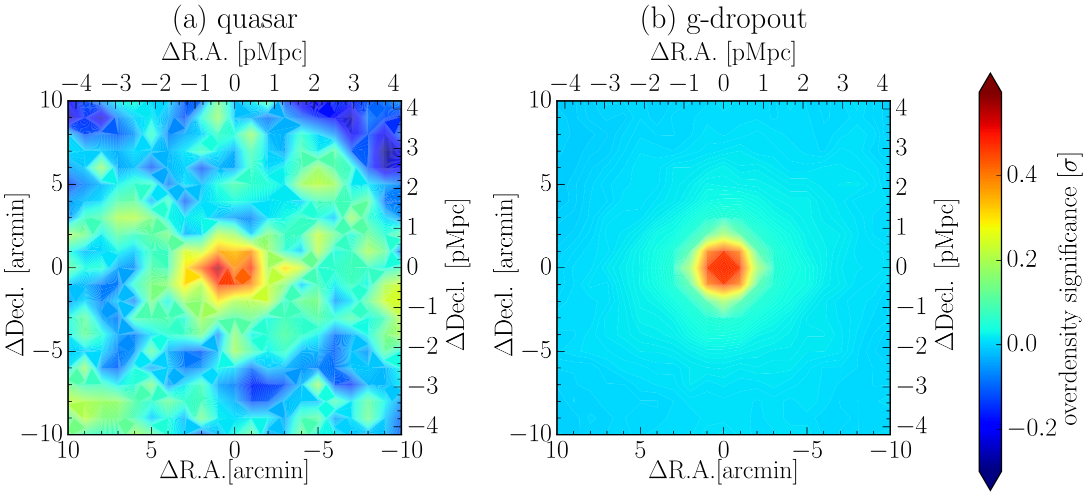

Figure 17 Median stacking overdensity significance map in the vicinity of quasars/g-dropouts. The panels (a) and (b) show the median stacking density map around quasars and g-dropouts, respectively. Their objects reside in the center of each panel. The size of each panel is 20 arcmin × 20 arcmin.

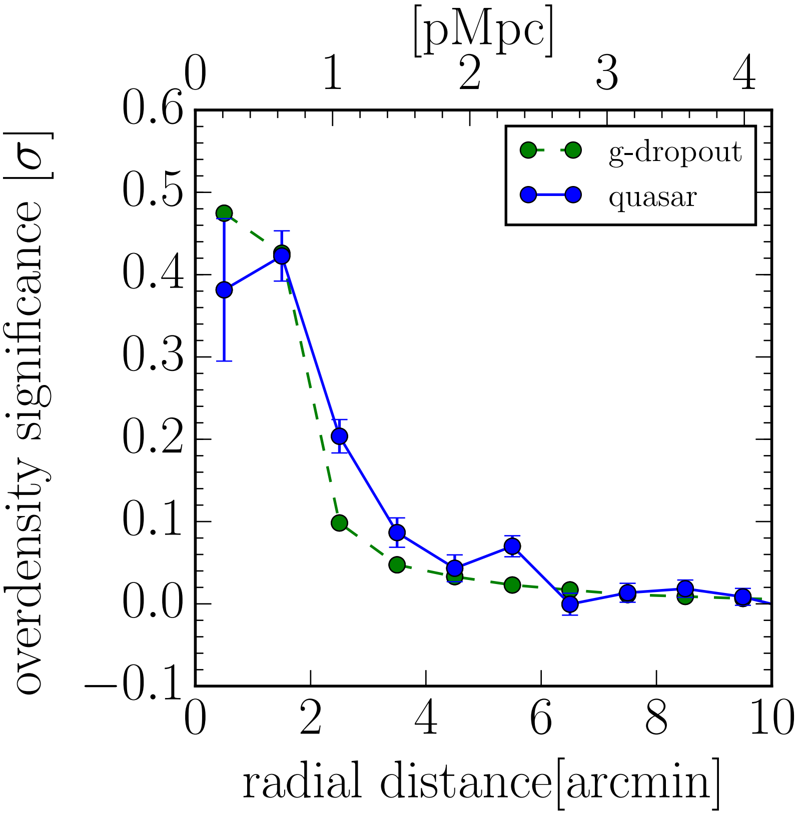

Figure 18 Radial profile of median stacked overdensity significance around quasars/g-dropouts. The blue points show the case of quasars. The bars indicate the 1σ standard error of the mean. The median of the radial distances of g-dropouts with 1σ standard error bars are represented by green points.

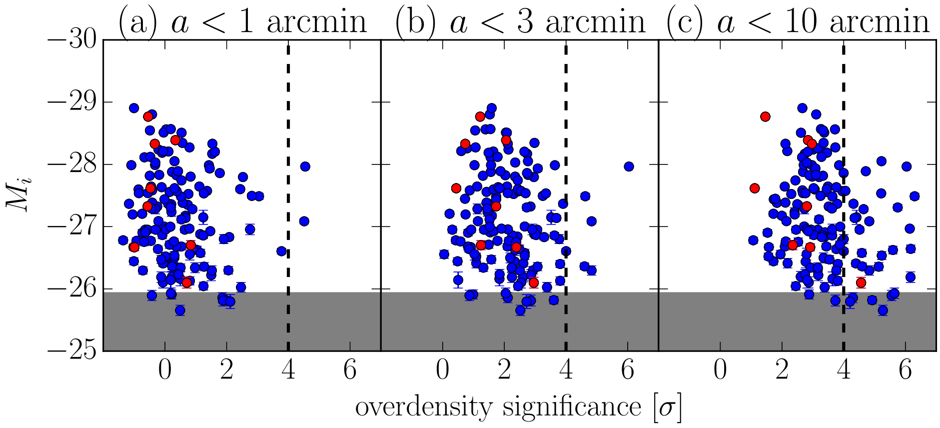

Figure 19 UV luminosities for overdensity significances in the vicinity of quasars. The panels (a), (b) and (c) show the relationship between the i-band absolute magnitudes of the quasars and the maximum overdensity significances centered on each quasar with radii 1, 3, and 10 arcmin, respectively. The FIRST detected quasars are also represented by the red points. The $> 4\sigma$ overdense regions are to the right of the dashed line. The gray shaded region shows the complete limit, which corresponds to the BOSS limiting magnitude of $r < 21.8$.

complete, the completeness limit (the gray shaded region) was shown, which corresponds to the BOSS limiting magnitude of $r < 21.8$, assuming $r - i = 0.145$, which is the median color of the SDSS quasar sample at $z = 3.3 - 4.2$. The Spearman rank correlation test revealed that the correlation coefficients are 0.165, 0.153, and 0.199, and the P-values are 0.0464, 0.0611, and 0.0146 for the three angular scales, respectively. This suggests weak correlations between the quasar luminosity and the environment with $\sim 2\sigma$ significance. These results show that brighter quasars statistically tend to reside in lower density regions of g-dropout galaxies. The black hole masses of quasars in Appendix A are also evaluated. These findings are summarized in Table 7 and discussed in next section.

Table 3 Spearman rank correlation test results for the relation between absolute i-band magnitudes (UV luminosity) and black hole masses of quasars and overdensity within 1 (0.42), 3 (1.25), and 10 (4.2) arcmin (pMpc).

UV luminosity	ρ [1]	P-value
local peak within 1 arcmin	0.165	0.0464
local peak within 3 arcmin	0.153	0.0611
local peak within 10 arcmin	0.199	0.0146
C IV-based BH mass	ρ [1]	P-value
Coatman et al. (2017)		
local peak within 1 arcmin	−0.194	0.0273
local peak within 3 arcmin	−0.0969	0.263
local peak within 10 arcmin	−0.0985	0.257
Park et al. (2013)		
local peak within 1 arcmin	−0.216	0.0136
local peak within 3 arcmin	−0.138	0.111
local peak within 10 arcmin	−0.140	0.107

[1] The correlation coefficient in the Spearman correlation test.

2.3 Discussion

2.3.1 The low coincidence of quasars and protoclusters

In this study, I attempted to identify any positive correlation between quasars and protoclusters at $z \sim 4$. Only two quasars were found to spatially coincide with protoclusters. However, for most quasars, there was no observed correspondence with the protoclusters. In this section, I will show how this result can be understood.

First, I try to compare the number densities of the $z \sim 4$ quasars and $z = 0$ galaxy clusters to elucidate the reason for their low positional coincidence. If the number density of the quasars at $z = 4$ is much lower than that of clusters, the quasars would not reside in the protoclusters. As a result, however, it was found that the number density of halos that are capable of hosting quasars at $z \sim 4$ is close to the number density of current clusters. The detail estimation is described as follows. The total comoving cosmic volume covered by the survey (121 deg^2 between $z = 3.3$ and $z = 4.2$) was approximately 1.18 cGpc^3. The space density of the 151 quasars which are almost completely observed (see Figure 19 and Figure 34) is thus approximately 3.74×10^{-7} h^3 cMpc^{-3}. The total number density of the halos that are capable of hosting such quasars can be evaluated by correcting the quasar number density for duty cycle and viewing angle. The net lifetime of a quasar is believed to be approximately $10^6 - 10^8$ yr from clustering or demographic analysis (e.g. Martini, 2004). The cosmic time between $z = 4.2$ and $z = 3.3$ is ~ 0.467 Gyr. Therefore, at any given time, it is expected that approximately $0.2 - 20\%$ of the halos can host quasars. This increases the halo number density to $1.87 \times 10^{-6} - 1.87 \times 10^{-4}$ h^3 cMpc^{-3}. Next, a correction needs to be performed for the viewing angle. It is expected that at most $50 - 70$ percent of random viewing angles will be along the line-of-sight, producing luminous quasars (Simpson, 2005). Thus, the total number density of halos hosting quasar-like host galaxies is $2.67 \times 10^{-6} - 3.74 \times 10^{-4}$ h^3 cMpc^{-3}. However, the number density of local rich clusters of galaxies with $> 10^{14}$ $M_\odot$ is approximately 1.26×10^{-5} h^3 cMpc^{-3} (e.g. Rozo et al., 2009), which is consistent with the halo number density estimated by the halo mass functions from Behroozi et al. (2013). The number density of halos that are capable of hosting quasars at $z \sim 4$ is thus close to the number density of current clusters.

Next, I will examine the reason why almost all the quasars are not found in the protoclusters from the viewpoint of the halo mass. I calculated what the percentage of the quasars which evolve into the halos with the mass of $> 10^{14} M_\odot$ at $z = 0$ is in our sample, by the Extended Press Schechter (EPS) model (Press & Schechter, 1974; Bower, 1991; Bond et al., 1991; Lacey & Cole, 1993) which can evolve the $z \sim 4$ quasar halo masses into their $z = 0$ descendant halo masses. There is a large variance in the $z \sim 4$ quasar halo mass due to the rarity of the high-z quasars (e.g. He et al., 2018). Thus, the percentage was calculated in the following two cases ((a) and (b)).

(a) The halo mass of quasars is observationally estimated using clustering analysis as $M_{\rm halo} \sim 4 - 6 \times 10^{12}\ h^{-1}M_{\odot}$ at $z > 3.5$ (Shen et al., 2007), which represents the minimum halo mass. Approximately $30-50$ % of these should evolve into halos with masses $> 10^{14}\ M_{\odot}$ at $z = 0$ based on the the EPS model. This estimate is likely to be a lower limit because the mean halo mass is approximately 3 times the the minimum halo mass (e.g. Ishikawa et al., 2015). In principle, the number density and halo mass suggest that quasars could be associated with protoclusters, assuming that the Shen et al. (2007) halo mass estimates are correct. However, the results also show that there is no association between the HSC-SSP Wide protoclusters and the majority of the quasars, since only 2 out of 151 quasars were found to reside near protoclusters.

(b) Recently, Eftekharzadeh et al. (2015) derived less massive quasar halo mass, $M_{\rm halo} = 0.6 \times 10^{12} h^{-1}M_{\odot}$ at $z \sim 3$, based on the larger sample by BOSS. He et al. (2018) showed that the average halo mass of $z \sim 4$ less-luminous quasars, $M_i \gtrsim -26$, detected by HSC is $\sim 1 \times 10^{12} h^{-1}M_{\odot}$. In the GALFORM (e.g. Lacey et al., 2015), the halo mass function of quasars at $z \sim 4$ is predicted to have a peak at approximately $M_{\rm halo} \sim 0.3 - 1.0 \times 10^{12}\ \ h^{-1}M_{\odot}$ (Fanidakis et al., 2013; Orsi et al., 2016), which is approximately 10 times less massive than Shen et al. (2007), with a large range of mass distribution. Oogi et al. (2016) also predicted a few $10^{11}\ M_{\odot}$ for the median halo mass of quasars at $z \sim 4$. It should be noted that the clustering strength of quasars is almost independent of their luminosity (e.g. He et al., 2018; Shen et al., 2013; Eftekharzadeh et al., 2015). The quasar halo mass of $\sim 0.3 - 1.0 \times 10^{12}\ h^{-1}M_{\odot}$ at $z \sim 4$ yields a probability that the $z = 0$ descendant halo mass exceeds $10^{14} M_{\odot}$ of only $\sim 1 - 5\%$. This result seemed to be reasonable, suggesting that a typical quasar halo mass might be $\lesssim 10^{12} h^{-1}M_{\odot}$ at $z \sim 4$.

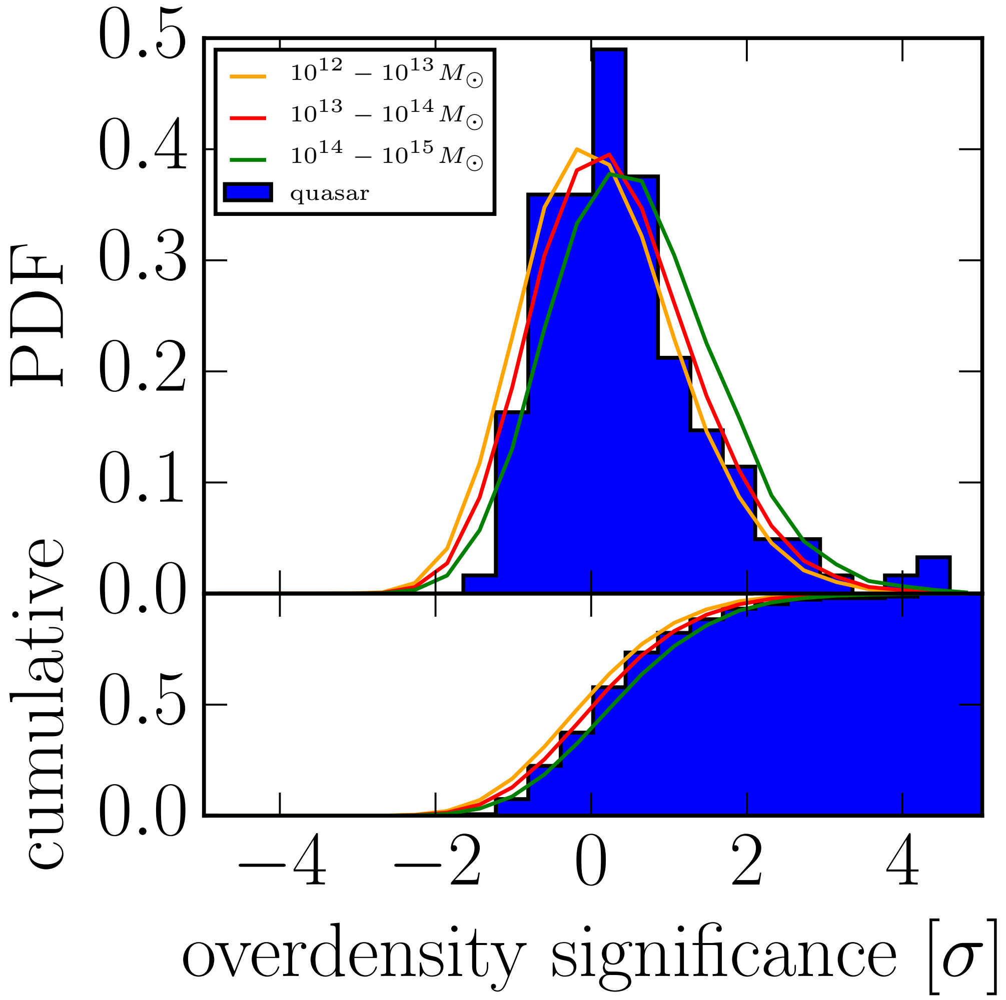

Figure 20 Correspondence between observational overdensity significances of quasars and their $z = 0$ descendant halo masses and simulated g-dropouts. The blue histogram shows the distribution of the maximum overdensity significances centered on quasars with a radius of 1 arcmin, which is exactly the same as Figure 15 (a). The orange, red, and green lines represent the simulated g-dropout overdensity significance distributions with $z = 0$ descendant halo masses $M_{\mathrm{h,z=0}} = 10^{12}\ M_\odot - 10^{13}\ M_\odot$, $M_{\mathrm{h,z=0}} = 10^{13}\ M_\odot - 10^{14}\ M_\odot$ and $M_{\mathrm{h,z=0}} > 10^{14}\ M_\odot$, respectively. Their overdensity significances are the ones simulated for $z \sim 4$.

The descendant halo masses at $z \sim 0$ can be also estimated from the distribution of overdensity significances at the $z \sim 4$ quasar positions (Figure 15 (a)) by using the light cone model (Henriques et al., 2012). I associated the overdensity significances which simulated that g-dropout galaxies exist with their $z = 0$ descendant halo masses by tracing the halo merger tree from $z = 0$ to $z \sim 3.8$. Figure 20 presents the distribution of overdensity significances of the observed quasars at $z \sim 4$ (blue histogram) and simulated g-dropout galaxies with the descendant halo masses of $M_{\rm h,z=0} = 10^{12} M_\odot - 10^{13} M_\odot$ (orange line), $M_{\rm h,z=0} = 10^{13}\ M_\odot - 10^{14}\ M_\odot$ (red line) and $M_{\rm h,z=0} > 10^{14}\ M_\odot$ (green line) in the simulation. It is found that the predicted descendant halo mass distribution from overdensity significances of the observed quasars at $z \sim 4$ are generally consistent with the mass distribution $M_{\rm h,z=0} = 10^{13}\ M_\odot - 10^{14}\ M_\odot$ with P-value = 0.314, but were inconsistent with those of $M_{\rm h,z=0} = 10^{12}\ M_\odot - 10^{13}\ M_\odot$ and $M_{\rm h,z=0} > 10^{14}\ M_\odot$ with P-value = 0.00502 and 0.0332 in the KS test, respectively. Generally, luminous quasars at $z \sim 4$ reside in density environments which evolve into halos with a mass of $\sim 10^{13}\ M_\odot - 10^{14}\ M_\odot$.

In summary, the reason for the low coincidence of the quasars and the protoclusters is as follows. The quasar halo masses at $z \sim 4$ are expected to be $\lesssim 10^{12} h^{-1} M_\odot$. Almost all the halos with such halo masses could evolve into halos with a mass of $\sim 10^{13}\ M_\odot - 10^{14}\ M_\odot$, and only $1 - 5\%$ quasars might evolve into the cluster halo masses of $> 10^{14} M_\odot$.

Table 4 Statistical Test for Correlation of Position between bright quasars and protoclusters

	KS P-value	Median quasar	Median g-dropout
local peak within 1 arcmin	0.0392	0.189	0.474
local peak within 3 arcmin	0.702	1.78	1.94
local peak within 10 arcmin	0.849	3.06	3.12

These results can be compared with those of Adams et al. (2015), who found one overdense region of LBGs ($r < 25.0$) in a sample of 9 luminous SDSS quasars, $M_i < -28.0$, at $z \sim 4$. If a sample with the same luminosity range as that of their 9 quasars is chosen from the 151 quasars, it is found that only one out of 27 quasars reside in a protocluster. Although the fraction of the quasars in overdensities appears to be three times higher in Adams et al. (2015), it is noted that none of their quasars lie in overdensities as significant as the $> 4\sigma$ overdensities that were selected in this work. In addition, it is interesting to note that the evidence for a physical overdensity in the case of the quasar in Adams et al. (2015) only appear after spectroscopic follow-up, showing that spectroscopic redshifts are crucial to obtaining definitive answers.

It is also found that no FIRST-detected quasars reside in $> 4\sigma$ overdense regions. However, Hatch et al. (2014) showed at a high statistical significance, the radio-loud AGNs reside in denser Mpc-scale environments than similarly massive radio-quiet galaxies at $z = 1.3 - 3.2$. Venemans et al. (2007) found that 6 out of 8 radio galaxies reside in overdense regions. This difference between results might be attributed to not only the aforementioned reasons but also to the differences in selection criteria. The radio-loud AGN from Hatch et al. (2014) and Venemans et al. (2007) are approximately 10 times more luminous in the radio than the FIRST-detected quasars, and the environments were measured in an entirely different manner. It is therefore difficult to assess whether the results are consistent or not. My results were also limited by the small sample size of only 8 FIRST-detected quasars. In the future, I will investigate the environments of large numbers of radio-loud and radio-quiet quasars using the full 1400 deg^2 of the HSC-SSP Wide survey in detail.

2.3.2 Do quasars appear through gas-rich major mergers?

From this observation, I cannot assess whether the appearance of quasar is caused by a gas-rich major merger, because the major merger scale is at most 75pkpc (Larson et al., 2016) which is much smaller than the typical scale of the $z \sim 4$ protoclusters, $\sim$ 3.6pMpc (Chiang et al., 2013). However, the $z \sim 4$ protoclusters has not yet virialized, and the average halo mass is estimated to be $\sim 3 \times 10^{13} M_\odot$

which corresponds to the galaxy group halo mass (Toshikawa et al., 2018), implying that it might be easy for the galaxy mergers to occur in the $z \sim 4$ protoclusters. Both of more detailed observations and numerical simulations about the galaxy merger in protoclusters are needed in order to examine the triggering mechanism of quasars.

2.3.3 The relation between density and quasar properties

It is found that UV brighter quasars statistically tend to reside in lower dense regions of g-dropout galaxies. In addition, quasars with the most massive black holes tend to avoid overdense regions. Figure 21 shows the distributions of overdensity significances of bright quasars that are defined as being brighter than the median of the absolute i-band magnitudes of the quasar sample. In fact, the brighter quasars significantly reside in lower dense regions than g-dropout galaxies, at least in the 1 arcmin-scale environment. The results are summarized in Table 4. The results of earlier works have suggested that the strong radiation from quasars may provide negative feedback and suppress nearby galaxy formation, especially for low-mass galaxies (Kashikawa et al., 2007). The near zone sizes (e.g. Fan et al., 2006; Mortlock et al., 2011) of the quasar sample were used to evaluate the scale of the AGN feedback. The intrinsic flux was estimated by fitting a single power law to the continuum, free of line emissions at $\sim 1340 - 1360$ Å, $1440 - 1450$ Å and $1700 - 1730$ Å. The IGM transmission curves are calculated by the observed fluxes divided by the intrinsic fluxes blueward of Lyα and then fitted using a single power law. Then, the near zone size is defined by the proper radius at which the fitted transmission first falls below 10 % (Fan et al., 2006; Mortlock et al., 2011). Figure 22 shows the relation between the overdensity significance and the near zone size for each quasar. Although the scatter is large, it appears that quasars tend to have much smaller near zones when their overdensity significance is larger than $\sim 2\sigma$. In addition, quasars in lower density regions can have the full range of near zone sizes. The statistical coefficient ρ and the P-value are -0.232 and 0.00798 in the Spearman rank correlation test. These findings may indicate that galaxy formation is delayed in overdense regions due to quasar feedback. Another possibility is that the near zones in overdense regions are smaller due to the much

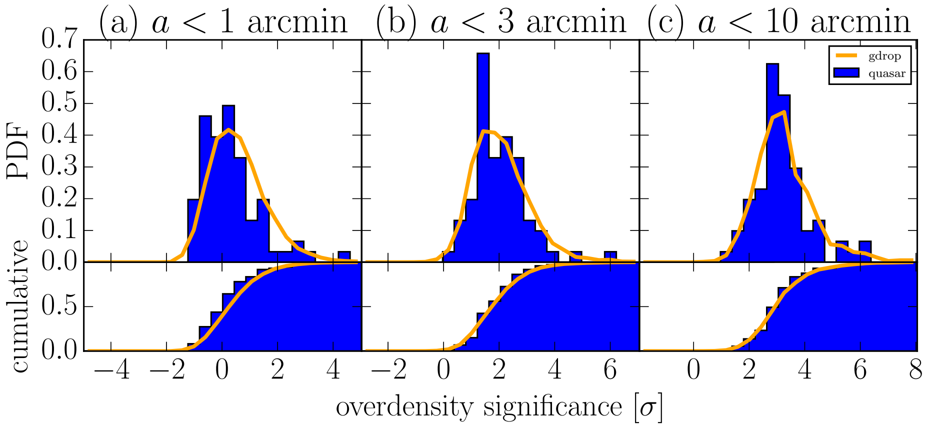

Figure 21 Histogram of overdensity significance of bright quasars. The panels (a), (b) and (c) show the histograms of the maximum overdensity significance centered on quasars with the radius of 1(0.42), 3(1.25), and 10(4.2) arcmin(pMpc), respectively.

higher gas densities, which are more difficult to fully ionize.

Considering the viewing angle of type-1 quasars, this effect should be the most significant on the number density of galaxies along the quasar line of sights (LOS), and become weaker as it moves away from the LOS. The tendency towards low-density at < 1 arcmin as observed in Figures 18 and 21 could also be caused by this effect. The results of the statistical test to examine the possible UV luminosity, black hole mass and near zone size dependence on the distance to the nearest overdense region (see Figures 19, 34, and 22) is in agreement with the hypothesis although projection effects may smear out this small-scale over (under) the density signal.

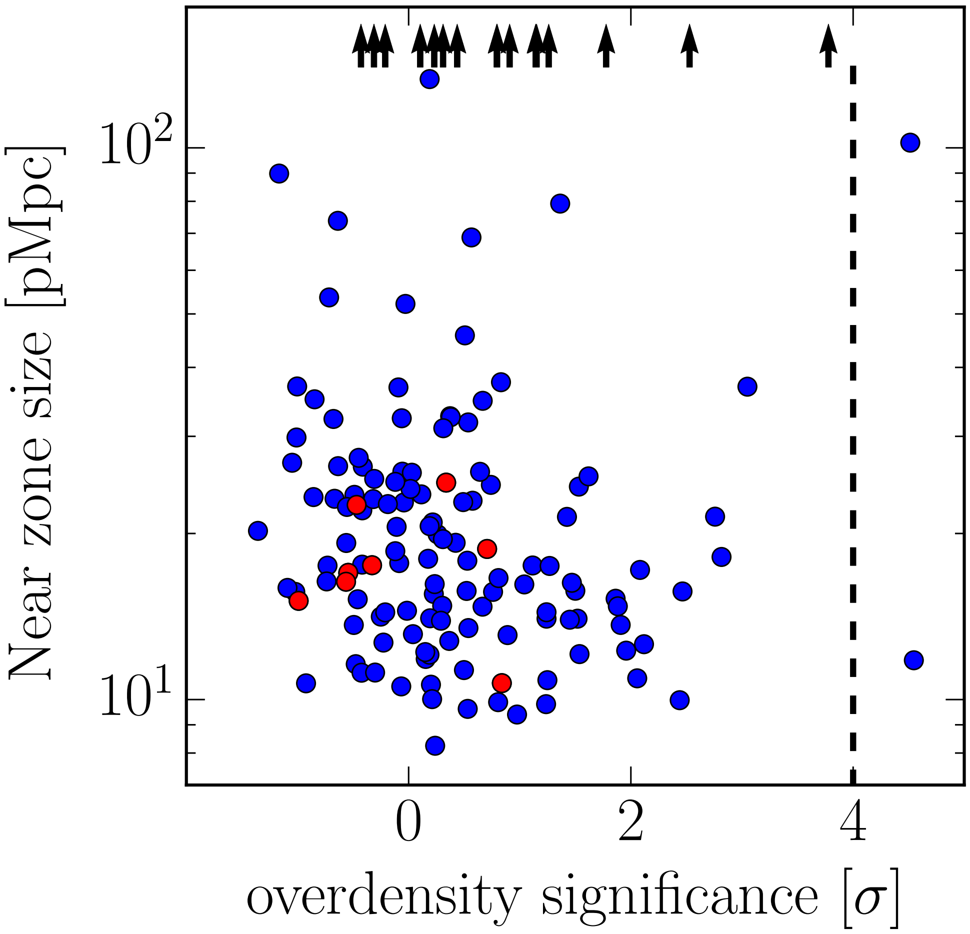

Figure 22 Near zone size of quasars as a function of the overdensity significance. The red points show the FIRST-detected quasars. The black arrows show quasars with near zone sizes larger than 150 pMpc. The $> 4\sigma$ overdense regions are to the right of the dashed line.

Chapter 3 Photoevaporation

In this chapter, the details of experiments involving wide field imaging with a Suprime-Cam mounted on the 8.2 m Subaru telescope targeting 11 fields with a strong local UV background from quasars at $z = 2 - 3$ order is presented. This work was performed to study the radiative feedback effect on low-luminosity galaxy systematically. In §3.1, the selection and reduction of targeted quasar fields are described, and our LAE sample is constructed. In §3.2, the LAE galaxy density in the vicinity of the quasars is investigated. The correlations between the galaxy density and the properties of the LAEs and the quasars (e.g. black hole mass and luminosity) are examined. The implications of our results are discussed in §3.3.

3.1 DATA AND SAMPLE SELECTION

3.1.1 Observations and Reduction

The quasar fields were selected based on the following criteria. I selected quasars whose redshifted Lyα fell in the wavelength range of the Suprime-Cam NB filters, $NB400$ ($\lambda_{\rm c}$ = 4000Å, FWHM= 92Å, $z_{\rm Ly\alpha} = 2.29^{+0.04}_{-0.04}$), $NB413$ ($\lambda_{\rm c}$ = 4130Å, FWHM= 83Å, $z_{\rm Ly\alpha} = 2.40^{+0.03}_{-0.04}$), $NB503$ ($\lambda_{\rm c}$ = 5030Å, FWHM= 74Å, $z_{\rm Ly\alpha} = 3.14^{+0.03}_{-0.04}$) or $NB515$ ($\lambda_{\rm c}$ = 5150Å, FWHM= 79Å, $z_{\rm Ly\alpha} = 3.24^{+0.03}_{-0.04}$), where $z_{\rm Ly\alpha}$ shows the Lyα redshift ranges corresponding to the FWHMs of the NB filters. Their filter transmission curves are shown in Figure 23. Systemic redshifts were found based on Hβ, [OIII] emission lines (Netzer et al., 2007; Shemmer et al., 2004) or narrow low ionization lines (Sulentic et al., 2014), which are more reliable than those measured by Lyα or CIV lines because they are easily influenced by quasar outflows as seen in §2. Quasars with a wide range in the UV luminosity (logλL_λ(912Å)= 45.6 − 47.8)were selected in order to investigate the variation of the quasar photoionization feedback. In total, 11 quasar fields were observed, of which three fields contained radio-loud quasars (SDSS1411, TXS1529

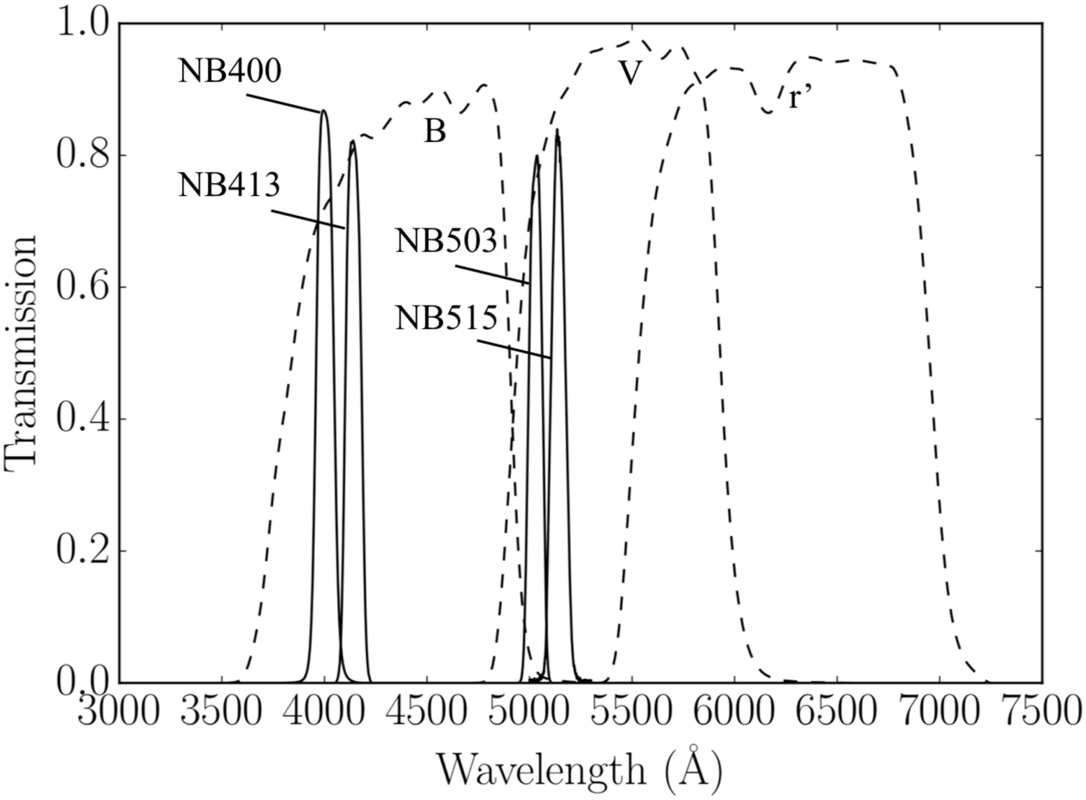

Figure 23 Filter transmission curves. The dashed lines show the transmission curves of broad-band filters, B, V, r', from left. The solid lines indicate the curves of narrow-band filters, $NB400$, $NB413$, $NB503$ $NB515$, from left.

and SDSS2135) and one field contained a quasar-pair with two quasars (SDSS1623 and SDSS1624) in close proximity to each other (e.g. Djorgovski et al., 1987; Onoue et al., 2018). The redshift and angular separation of the quasar-pair are $\Delta z = 0.006$ and $\Delta\theta = 3.5$ arcmin (1.7 pMpc), respectively. The properties of the quasars are also summarized in Table 5.

Observations were made on six nights in UT 2014, 2015 and 2017. The Suprime-Cam has ten 2k ×4k Hamamatsu CCDs, and covers a contiguous area of $34' \times 27'$ with a pixel scale of $0.''202$ pixel^{-1}. BB imaging is required to measure the flux excess in NB filters. The integration time was 12000–16800 s for each band. For the BB filters, the typical unit exposure time was 600 s for the B-band and V-band filters and 300 s for the r'-band filter, which was used because the V-band filter was not available during the observations of the SDSS1551 quasar field. In the case of the NB filters, the exposure time was 1200s. I adopted a common circle dithering pattern (full cycle) consisting of 7–9 pointings for NB filters and 4–8 pointings for BB filters. The sky condition was relatively good with a seeing size of 0.60–1.40 arcsec. The observation configuration is shown in Table 6.

I used SDFRED version 2.0 (Yagi et al., 2002; Ouchi et al., 2004) to perform data reduction of NB and BB images. The L.A. Cosmic recipe (van Dokkum, 2001) was used to remove cosmic rays, which was significant in the NB images acquired with long exposure time (1200 s). Flux calibrations of NB images were performed using a spectrophotometric standard star Feige110 for $NB400$, $NB413$ and $NB515$ images and Feige63 for $NB503$ images. For the BB images, I used the photometric standard stars SA110 and SA113 for the BB images and SA110 for the V-band images. The calibrations for the r'-band were performed using stars in the SDSS DR14 catalog. The estimated zero-point magnitudes were carefully examined using spectroscopic A-type stars, which have an almost flat spectrum in our observed wavelength range found in SDSS DR14. The astrometric calibration of NB-detected objects was performed using the Naval Observatory Merged Astrometric Dataset (NOMAD). The astrometric accuracy is ~ 0.3 arcsec and was estimated using the SDSS DR14 catalog.

Table 5 Taget quasar sample

Quasar Name	R.A. (J2000)	Decl. (J2000)	$z_{\rm sys}$ [1]	$\log\lambda L_\lambda$ [2] (erg s^{-1})	$\log M_{BH}$ [3] ($M_\odot$)	radio [4]	ref. 1 [5]	ref. 2 [6]
SDSS J142656.18+602550.8	$14^h26^m56.1^s$	$+60^\circ25'50''$	3.202	47.8206	$9.82^{+0.30}_{-0.30}$	quiet	3	3
OH91–121	$12^h35^m02.6^s$	$-11^\circ30'29''$	2.407	46.9242	$9.89^{+0.05}_{-0.05}$	quiet	*	2
SDSS J141123.51+004253.0	$14^h11^m23.5^s$	$+00^\circ42'53''$	2.257	46.7248	$9.37^{+0.30}_{-0.30}$	loud	3	3
HB89–1835+509	$18^h36^m14.50^s$	$+51^\circ01'45.0''$	2.272	46.4891	$9.34^{+0.06}_{-0.06}$	quiet	*	2
SDSS J170102.18+612301.0	$17^h01^m02.18^s$	$+61^\circ23'01.0''$	2.301	46.4573	$9.72^{+0.30}_{-0.30}$	quiet	3	3
TXS 1529–230	$15^h32^m31.5^s$	$-23^\circ10'32''$	2.280	46.3152	$9.42^{+0.13}_{-0.13}$	loud	*	2
SDSS J213510.60+013930.5	$21^h35^m10.6^s$	$+01^\circ39'31''$	3.199	46.2128	$8.65^{+0.30}_{-0.30}$	loud	3	3
SDSS J155137.22+321307.5	$15^h51^m37.22^s$	$+32^\circ13'07.5''$	3.143	46.0280	$9.54^{+0.18}_{-0.18}$	quiet	4	4
SDSS J095141.33+013259.5	$09^h51^m41.33^s$	$+01^\circ32'59.5''$	2.411	45.9534	$8.90^{+0.20}_{-0.20}$	quiet	1	1
SDSS J125034.41–010510.5	$12^h50^m34.41^s$	$-01^\circ05'10.5''$	2.397	45.8869	$9.06^{+0.20}_{-0.20}$	quiet	1	1
SDSS J162421.29+554243.0	$16^h24^m21.29^s$	$+55^\circ42'43.0''$	2.278	45.6695	$8.59^{+0.04}_{-0.04}$	quiet	*	2
SDSS J162359.21+554108.7	$16^h23^m59.21^s$	$+55^\circ41'08.7''$	2.272	45.5920	$8.86^{+0.05}_{-0.05}$	quiet	*	2

[1] Systemic redshift.

[2] Logarithm of intrinsic luminosity at rest-wavelength 912Å in $L_\odot$, which is estimated by fitting a single power law to the continuum free of the line emission (§3.1).

[3] Logarithm of black hole mass in $M_\odot$.

[4] Radio loud or not (Shemmer et al., 2004; Sulentic et al., 2014).

[5] The reference for the black hole mass: (1) Netzer et al. (2007); (2) Sulentic et al. (2014); (3) Shemmer et al. (2004); (4) Saito et al. (2016). * shows that the black hole mass was estimated using the CIV-based black hole mass estimator of Shen et al. (2011) based on the parameters given by Sulentic et al. (2014). Netzer et al. (2007) found that the errors of the black hole masses are estimated to be $20-60\%$. I provided the error of 60% for their black hole masses. The typical uncertainties of the black hole masses estimated by Shemmer et al. (2004) are less than a factor of two. Their list of masses has an uncertainty factor of two.

[6] The reference for $z_{\rm sys}$: (1) Netzer et al. (2007); (2) Sulentic et al. (2014); (3) Shemmer et al. (2004); (4) Saito et al. (2016).

The double image mode of SExtractor version 2.19.5 (Bertin & Arnouts, 1996) was used for object detection and photometry. Objects were detected with at least 10 connected pixels above 1.5σ times the sky background rms noise and photometric measurements were performed at the 1.5σ level in the NB images. The sky background rms was estimated using SExtractor as follows. Each image was separated into several meshes of 24 arcsec. The mean and standard deviation of the counts in each mesh were estimated with 3σ clipping, and mesh values that were too bright were removed using median filtering. Finally, the sky background rms was interpolated using a bicubic interpolation for each mesh. The area around bright objects and shallower regions around the edge of each image (~ 3 arcmin)were masked. The magnitudes of detected objects were measured within apertures of 2 arcsec diameter. The 5σ limiting magnitudes measured in the 2 arcsec apertures are summarized in Table 6 for all images.

3.1.2 LAE Selection

The following criteria were used, which are essentially the same as Mawatari et al. (2012) and Matsuda et al. (2005), to select LAEs in all quasar fields :

$$\begin{aligned} m_{\rm BB} - m_{\rm NB} &> f(EW_0 = 20\text{Å}), & (7) \\ m_{\rm NB} &< m_{{\rm lim},5\sigma}, & (8) \\ m_{\rm BB} - m_{\rm NB} &> h + 3\sigma_{\rm color}, & (9) \end{aligned}$$

where $m_{{\rm lim},5\sigma}$ and $3\sigma_{\rm color}$ are the 5σ limiting magnitude and 3σ $m_{\rm BB} - m_{\rm NB}$ color error, respectively. h is the color term, for which I use the typical $m_{\rm BB} - m_{\rm NB}$ color of the galaxies without Lyα emission, which was assumed to be the mode in the color distribution of objects lying in the range of $18.0 < m_{\rm NB} < 24.0$. $f(EW_0 = 20\text{Å})$ is the color which corresponds to the Lyα equivalent width (EW_0) of 20Å at rest frame, as expected using the LAE model presented in Appendix B. If the objects were not detected using the BB filter at 2σ, their BB magnitudes were replaced by the corresponding 2σ limiting magnitudes. In addition, I carefully visually checked the images and removed false detections. As a result, 1171 LAEs were obtained in total. 195 of them did not exhibit a UV continuum detection. These LAEs may appear due to the quasar fluorescence effect (e.g. Cantalupo et

Table 6 Observation log

Quasar Name	filter	exposure time × shots (sec)	seeing (arcsec)	$m_{lim,5\sigma}$ (mag)	Date
SDSS J142656.18+602550.8	$NB515$	1200 × 7	$0.''78$	25.63	2014 May 27
	V	600 × 4	$0.''80$	25.95	2014 May 27
OH91–121	$NB413$	1200 × 7	$1.''20$	25.45	2015 Jun 17
	B	600 × 7	$1.''20$	26.23	2015 Jun 16
SDSS J141123.51+004253.0	$NB400$	1200 × 8	$1.''04$	25.75	2014 May 25
	B	600 × 5	$1.''30$	26.25	2014 May 26
HB89–1835+509	$NB400$	1200 × 8	$0.''84$	25.73	2015 Jun 16
	B	600 × 4	$0.''94$	26.59	2015 Jun 17
SDSS J170102.18+612301.0	$NB400$	1200 × 9	$1.''10$	25.72	2014 May 25
	B	600 × 4	$0.''70$	27.12	2014 May 27
TXS 1529-230	$NB400$	1200 × 5	$0.''96$	25.00	2015 Jun 16
	B	600 × 4	$0.''96$	26.04	2015 Jun 17
SDSS J213510.60+013930.5	$NB515$	1200 × 8	$1.''10$	24.95	2014 May 26
	V	600 × 4	$0.''80$	25.48	2014 May 27
SDSS J155137.22+321307.5	$NB503$	$900 \times 4 + 600 \times 10$	$0.''60$	25.28	2017 May 23
	r' [1]	300 × 6	$1.''12$	25.80	2017 May 23
SDSS J095141.33+013259.5	$NB400$	1200 × 9	$1.''24$	25.23	2014 May 25, 26, 27
	B	600 × 5	$0.''96$	26.44	2014 May 27
SDSS J125034.41–010510.5	$NB413$	1200 × 8	$1.''40$	25.77	2014 May 26, 27
	B	300 × 8	$1.''40$	26.12	2014 May 26
SDSS J162421.29+554243.0	B	600 × 4	$0.''98$	26.88	2015 Jun 17
SDSS J162359.21+554108.7	$NB400$	1200 × 7	$1.''20$	25.67	2015 Jun 17

[1] The r'-band was used because the V-band filter was not available for SDSS1551.

al., 2007). It was confirmed that even if the 195 LAEs are excluded, the results did not change within the 1σ error. The number of LAE candidates obtained using the criteria in each field is also listed in Table 7 and the color-magnitude diagrams of the fields are shown in Figure 24. Figure 25 shows the number counts of LAEs in each quasar field. The counts are consistent with those of previous studies (Mawatari et al., 2012; Grove et al., 2009), who studied a field in the vicinity of a radio galaxy 53W002 (744 arcmin^2) and some blank fields BRI 1202–0725, BRI 1346–0322 and Q 2138–4427 (133 arcmin^2), respectively. The contamination of low-z emitters can be ignored because the contamination rate is expected to be at most, $\sim 1\%$ [1] , according to Mawatari et al. (2012); Matsuda et al. (2005, 2006); Venemans et al. (2005). There is no excess in the $m_{\rm BB} - m_{\rm NB}$ color of the SDSS1551, SDSS1701, and OH91–121 quasars due to the strong absorption observed in the spectrum at the Lyman α line. In addition, the flux of quasar SDSS1426, which is not plotted in the color-magnitude diagram, could not be accurately measured due to saturation of the CCD. Two possible quasars, SDSS J125036.70-005531.7 (Lee et al., 2013) and QSO B1833+509 (Weedman, 1985), whose redshifts were estimated by Lyα emission, coincidentally fell in the NB filters, and reside in the SDSS1250 and OH91–121 quasar fields as shown in Figure 24 (black open stars), respectively. I confirmed that even if the two quasars are included in the analysis, the results did not change.

The detection completeness of LAEs was estimated by Monte Carlo simulation. Initially, 5000 artificial objects were distributed with $18.0 < m_{\rm NB} < m_{\rm lim,5\sigma}$ so that the EW distribution follows that of Mawatari et al. (2012), $f(EW_0) = Ce^{-EW_0/w_0}$, where C is a normalization constant and $w_0 = 43.7$ Å is the e-folding length. Source detection, photometry, and LAE selection were conducted with the same parameters used for the real images. Then, I defined the completeness as the fraction of the number of pseudo LAEs detected in each magnitude bin (an ensemble average was taken with 1000 realizations). The completeness is $\gtrsim 60\%$ at the 5σ

---

[1] For example, in the SDSS1250 field, the primary contaminants are [OII] emitters at $z \sim 0.11$ detected by NB413 (Mawatari et al., 2012). The expected number of [OII] emitters in the survey volume at the redshift is estimated to be only 5.9 by using the luminosity function and the equivalent width distribution of [OII] emitters (Ciardullo et al., 2013). Similarly, the number of NB400-detected [OII] emitters at $z \sim 0.07$ in the SDSS1411 field is expected to be 3.4.

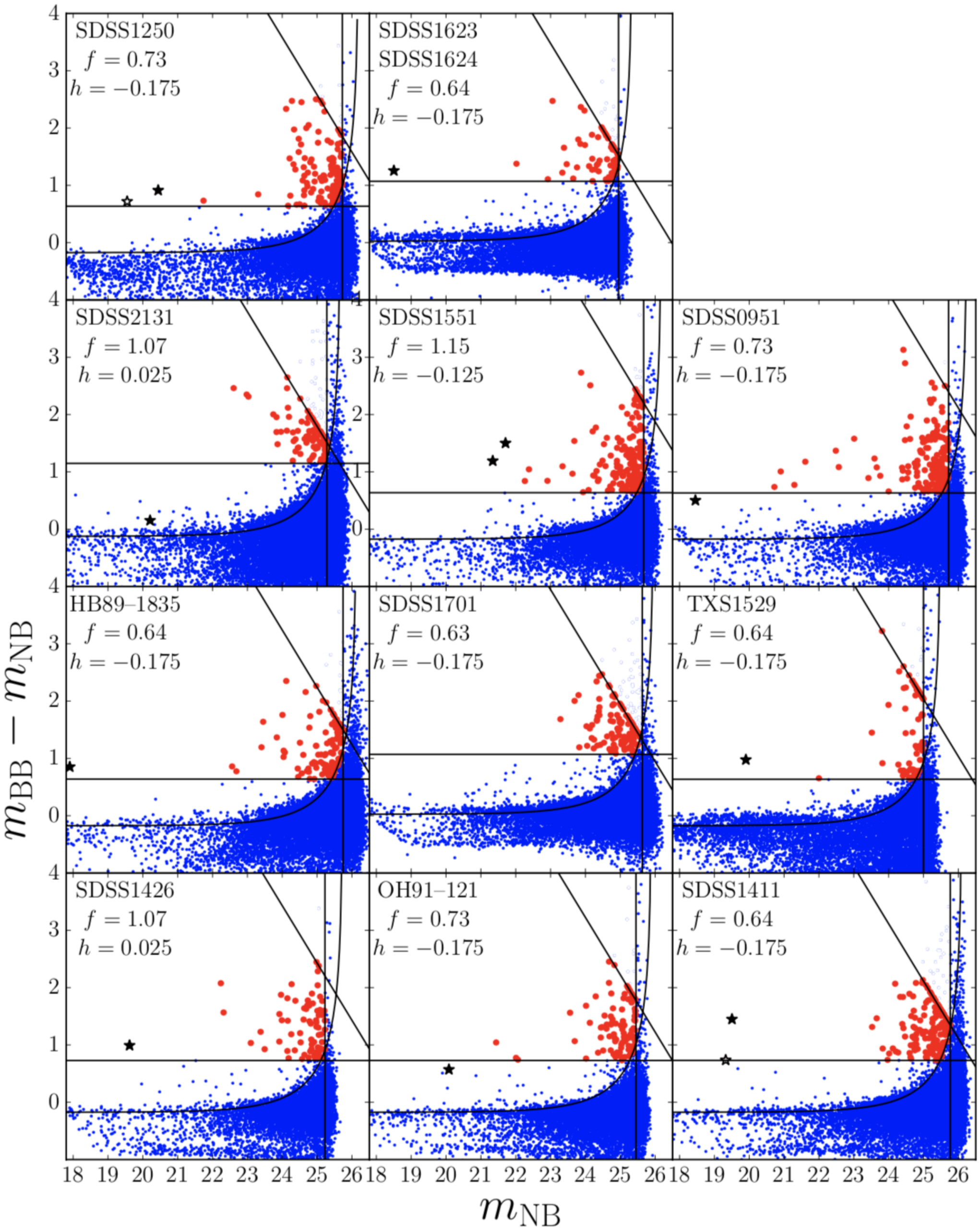

Figure 24 Color magnitude diagram $m_{\rm BB} - m_{\rm NB}$ versus $m_{\rm NB}$. The blue points show all objects except those in the masked regions around the bright stars. The red points indicate the LAE candidates and the black stars show the quasars in each field. The horizontal lines correspond to $EW_0 = 20$Å. The 5σ NB limiting magnitudes in each field are represented by the vertical lines and the $h + 3\sigma$ color errors are represented by curved black lines. The diagonal lines show the 2σ BB limiting magnitudes in each quasar field. There is no excess in the color of the SDSS1551, SDSS1701 and, OH91–121 quasars due to the strong absorption seen in the spectrum at the Lyman α line. In addition, the flux of the quasar SDSS1426 could not be accurately measured due to saturation. One field contains a quasar-pair (SDSS1623 and SDSS1624) in close proximity to each other.

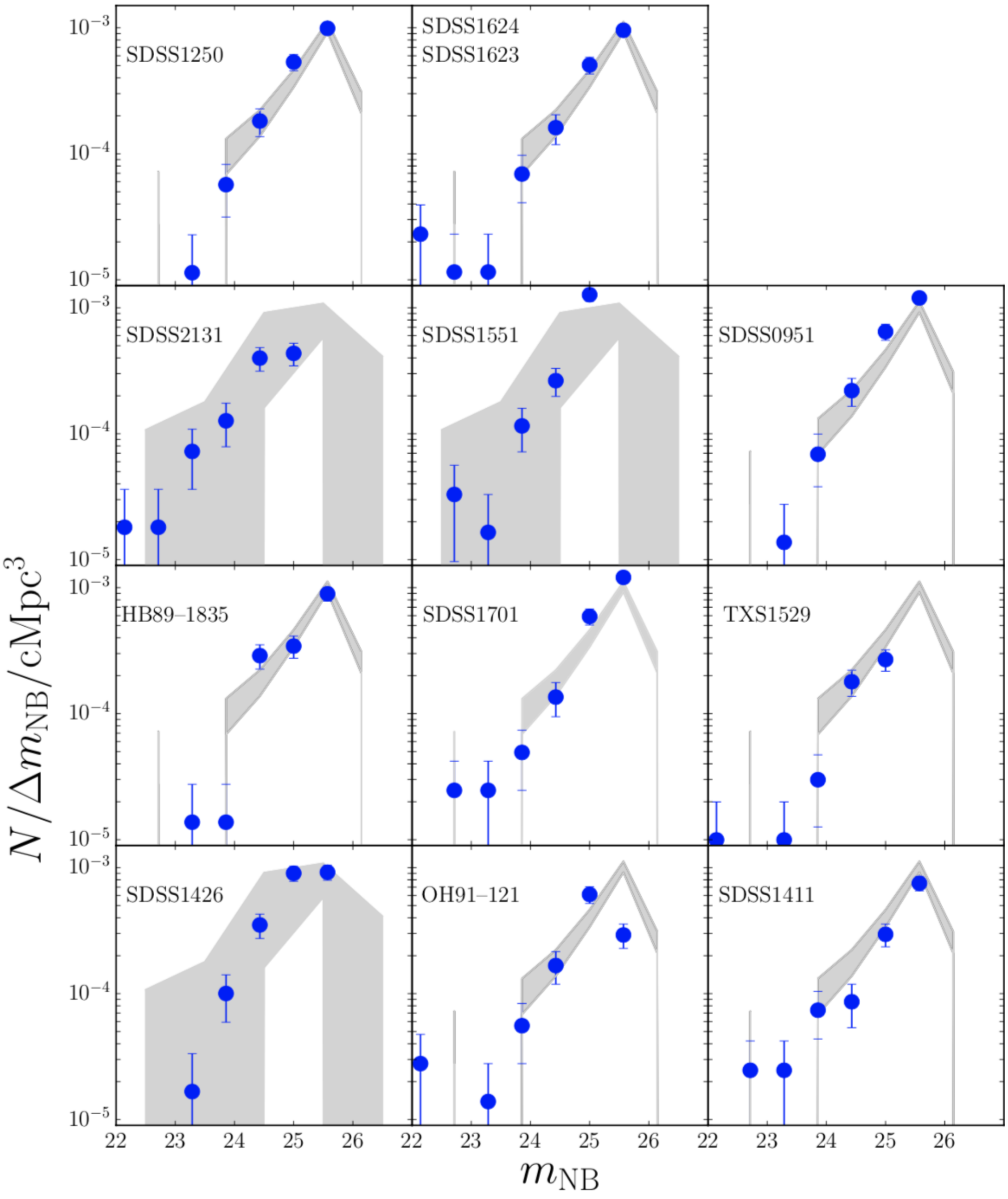

Figure 25 Number count of LAEs. The blue dots represent the number counts of LAEs in each quasar field. The error bars indicate the Poisson error. The gray shaded region shown in the HB89–1835, SDSS1623+1624, SDSS1701, SDSS1411, TXS1529, SDSS0951, OH91–121, and SDSS1250 quasar fields at $z \sim 2$ indicates the LAE number count of Mawatari et al. (2012). In the case of the SDSS1551, SDSS1426, and SDSS2131 fields at $z \sim 3$, they indicate the count given in Grove et al. (2009).

limiting magnitude of the NB filter for each field.

3.2 RESULTS

3.2.1 LAE Galaxy Density around Quasars

I applied the fixed aperture method to estimate the LAE surface density contour maps. A local number density was estimated by counting LAEs within the fixed aperture to evaluate the overdensity δ defined as $\delta = (N - \bar{N})/\bar{N}$, where N is the number of LAEs in the aperture. The scale of 8.0 cMpc was used as the radius of the distributed apertures in each field (Kikuta et al., 2017). $\bar{N}$ represents the average of N given by the all-quasar field average of the LAE number counts at the 5σ NB limiting magnitude for each field. It was confirmed that the LAE number counts are consistent with each other for all the target regions. The surface density of the LAEs in the masked regions is assumed to be the same as $\bar{N}$. I also calculated the size of the quasar proximity zones, where the UV radiation from the quasars is higher than the UV background radiation. The isotropic UV intensity $J(\nu)$ of the radiation at the Lyman limit from a central quasar, J_{21}, is important in the evaluation of the quasar photoevaporation effect (Kashikawa et al., 2007):

$$J(\nu) = J_{21} \left(\frac{\nu}{\nu_L}\right)^{\alpha} \times 10^{-21} \text{ erg cm}^{-2} \text{ s}^{-1} \text{ Hz}^{-1} \text{ sr}^{-1}, \tag{10}$$

where ν_L is the frequency at the Lyman limit, and α is the slope of the flux density of the quasar, $F_\nu(\nu) \propto \nu^\alpha$. The intrinsic monochromatic luminosity at the Lyman limit was estimated by fitting a single power law to the flux (Figure 26), free of line emission at 1340—1360 Å, 1440—1450Å and 1700—1730Å, using the rest-frame wavelength quasar spectrum from the SDSS Science Archive Server (SAS), with a spectral resolution of $R \sim 1300$—2500 (Pâris et al., 2017), for the quasars obtained by SDSS. The spectra of OH91–121, TXS1529, and HB89–1835 were taken from Sulentic et al. (2014). The intensity of the UV background radiation at $z = 2 - 4.5$ was evaluated to be $J_{21} = 1.0^{+0.5}_{-0.3}$ with a weak dependency of the redshift using the QSO proximity effect measurements of Cooke et al. (1997). The local UV radiation within the circle of the radius of r_{prox},

$$r_{\text{prox}} = \frac{1}{4\pi}\sqrt{\frac{L(\nu_L)}{10^{-21}}}\ \text{pMpc}, \tag{11}$$

is expected to be enhanced compared with the UV background. Therefore, r_{prox} was used to search for possible photoevaporation effects on the properties of LAEs. For SDSS1426, the $J_{21} = 10$ radius was used instead of the $J_{21} = 1.0$ to evaluate the environmental effect because the radius of $J_{21} = 1.0$ is larger than the FoV due to the brightness of the quasar. The r_{prox} for each quasar was estimated using its own alpha. Assuming a fixed typical alpha value of -0.30 (Selsing et al., 2016), the r_{prox} varies by as little as ~ 0.04arcmin (~ 0.07cMpc). The values of r_{prox} are listed in Table 7. Figure 27 shows the density maps of the LAEs in each quasar field with r_{prox} indicated for $J_{21} = 1$ and 10.

The average density near the quasars is 0.023 cMpc^{-2}, which corresponds to an overdensity $\delta = 0.48$ with 0.82σ significance. The quasars are found to reside in average density environments, which is consistent with the results we found in §2. SDSS1624 occupies the highest density of 0.045 cMpc^{-2} which corresponds to an overdensity of $\delta = 1.539$. Interestingly, this quasar forms a close pair with another quasar. Onoue et al. (2018) found that quasar pairs statistically tend to reside in overdense regions at $z \sim 1$ and 4. The densities of the quasars are summarized in Table 7. I examined possible relations between the overdensities and black hole masses and the radio loudness of the quasars shown in Figure 28. There was no significant correlation as in the case of the SDSS quasars (§2). In the Spearman rank correlation test, the P-value of a relation between the overdensity and the black hole mass is 0.17. Using only radio-quiet quasars, the P-value is 0.24.

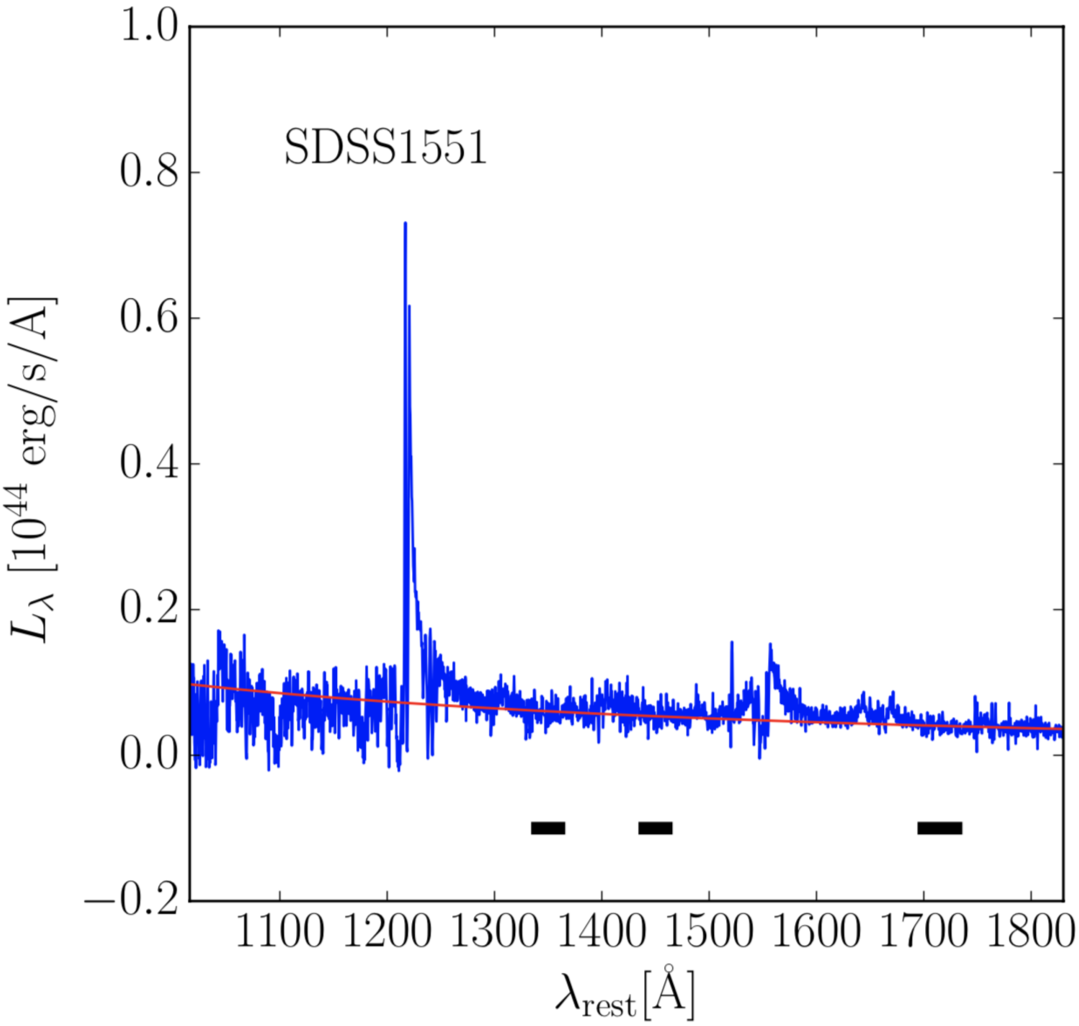

Figure 26 Example of fitting for the spectral energy distribution (blue line) of the SDSS1551 quasar. The red line indicates the fitted flux by a single power law. The black horizontal lines represent the free of line emission at 1340—1360 Å, 1440—1450Å and 1700—1730Å, respectively.

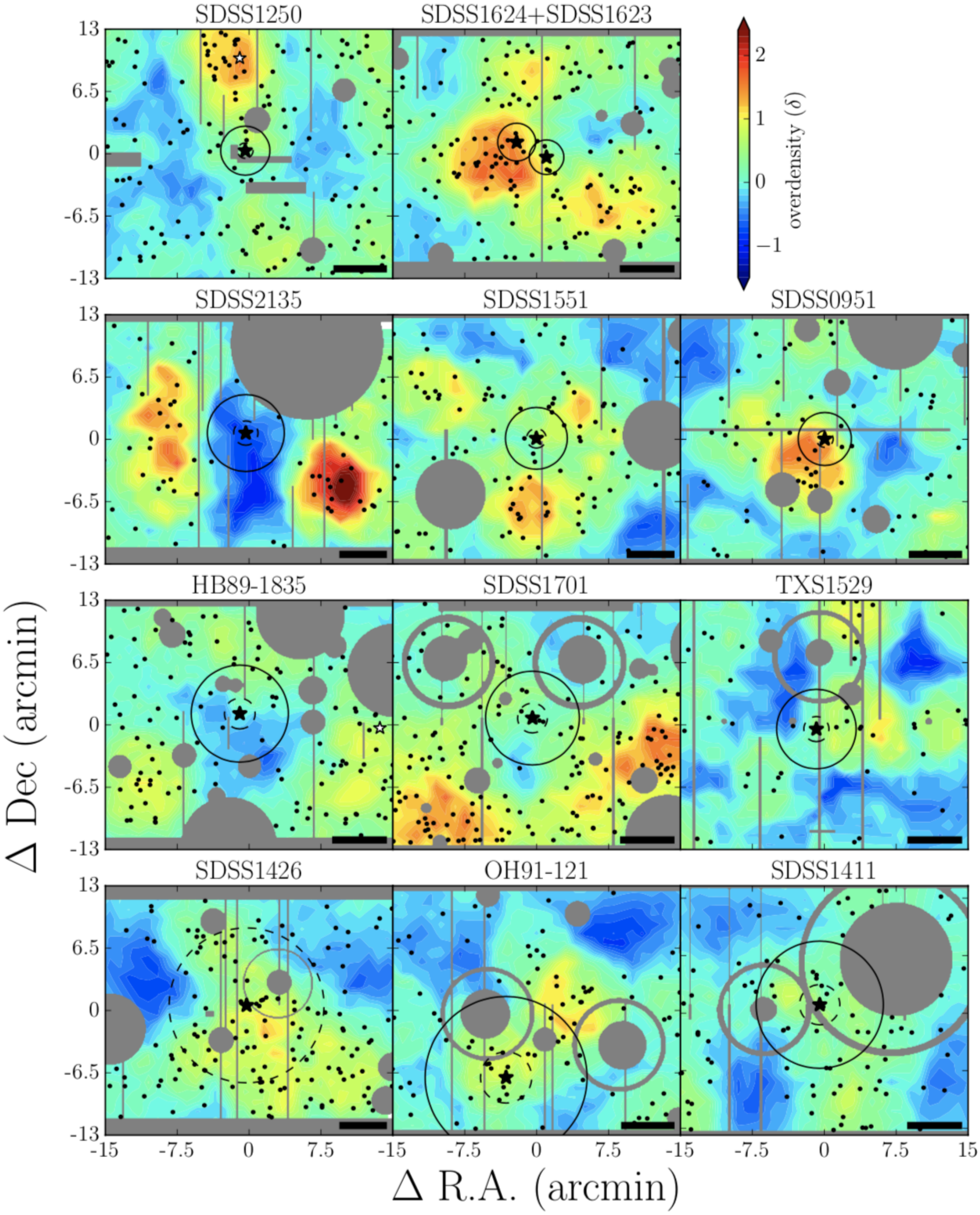

Figure 27 Overdensity maps in the quasar fields. The filled and open black stars show the quasars and possible quasars in each field, respectively. The black dots indicate the LAE candidates. The color contours show the overdensity. The radii of the isotropic UV intensity J_{21} of 1 and 10 are indicated by the solid and dashed black circles, respectively. The gray shaded regions show the masked regions. The size of each panel is 30 × 25 arcmin^2. The length of 8 cMpc, which is the scale used to derive the overdensity, is represented by the black line in the lower right corner in each panel.

Table 7 Results

Quasar Name	volume [1] ($\times 10^5$cMpc^3)	# LAEs [2]	overdensity [3]	$r_{\rm prox}$ [4] (arcmin (cMpc))	$N^{\rm exp}_{<r_{\rm prox}}(> 150Å)$ [5]	$N^{\rm obs}_{<r_{\rm prox}}(> 150Å)$ [6]
SDSS J142656.18+602550.8	1.05	137	0.741	25.5 (48.6)	0.866 [7]	7.45 [7]
OH91–121	1.26	84	0.640	8.44 (14.0)	4.22	3.63
SDSS J141123.51+004253.0	1.42	100	0.379	6.63 (10.7)	2.17	2.52
HB89–1835 +509	1.27	111	-0.0406	5.06 (8.17)	2.46	1.00
SDSS J170102.18+612301.0	1.42	162	0.216	4.89 (7.95)	12.8	0.00
TXS 1529-230	1.76	48	0.408	4.15 (6.70)	0.316	0.00
SDSS J213510.60+013930.5	0.967	59	-0.711	4.01 (7.63)	0.163	0.00
SDSS J155137.22+321307.5	1.06	103	0.337	3.22 (6.08)	0.00	0.00
SDSS J095141.33+013259.5	1.27	68	1.15	2.76 (4.60)	0.368	0.00
SDSS J125034.41-010510.5	1.54	157	0.437	2.56 (4.24)	0.464	0.00
SDSS J162421.29+554243.0	1.52	142	1.54	1.97 (3.19)	0.253	0.00
SDSS J162359.21+554108.7	1.52	142	0.653	1.80 (2.91)	0.188	0.00
Total [8]	16.1	1171			23.4	7.15
Total (exc. brightest quasars) [9]	11.0	739			14.6	0.00

[1] Effective volume in each field.

[2] The observed number of LAEs.

[3] Overdensity in which quasar reside. $\delta = (N - \bar{N})/\bar{N}$.

[4] The local UV radiation within the circle of the radius of $r_{\rm prox}$, that is defined by equation (11), is enhanced compared with the UV background by the radiation from each quasar.

[5] The observed completeness-corrected number of LAEs with $EW_0 > 150$Å in the quasar proximity zone.

[6] The expected completeness-corrected number of LAEs with $EW_0 > 150$Å in the quasar proximity zone.

[7] The $J_{21} = 10$ radius was used instead of the $J_{21} = 1.0$ radius which is used in other quasar fields because the radius of $J_{21} = 1.0$ in the SDSS1426 field is larger than its FoV.

[8] $N^{\rm exp}_{<r_{\rm prox}}(> 150Å)$ and $N^{\rm obs}_{<r_{\rm prox}}(> 150Å)$ are calculated excluding the SDSS1426 field.

[9] Total but for top four brightest quasars.

3.2.2 UV Luminosity Distributions of LAEs in the Vicinity of Quasar

The UV luminosity of a LAE is estimated using the proposed LAE model (see Appendix B). It should be noted that the derived $M_{\rm UV}$ distribution is affected by the discrepancy of completeness between the NB and BB filters since our Lyα selected sample is constructed from an NB magnitude-limited sample. It was difficult to correct the sample for completeness, and as such, I only focused on the relative difference of the distributions found in the vicinity and outer regions of the quasars. Figure 29 shows the $M_{\rm UV}$ distribution of the LAEs in the quasar fields. A deficit of faint ($M_{\rm UV} > -17$) LAEs in the proximity of a quasar can be seen in several fields. To examine this trend more clearly, the average UV luminosity distribution for all quasar fields except for the SDSS1426 is shown in Figure 30. The height of each distribution was normalized with that of SDSS1701 when the average is taken so that only the difference in the shapes of the distributions could be observed. The $M_{\rm UV}$ distributions are almost identical between the vicinity and outer region of the quasars at the bright end $M_{\rm UV} < -17.0$, while at the end, faint LAEs are significantly deficient in the vicinity of the quasars. The result suggests that fainter LAEs with $M_{\rm UV} > -17.0$ tend to avoid the central quasar as expected if the photoevaporation effects are shown. Moreover, It was found that faint LAEs with $M_{\rm UV} > -18.0$ only appeared in the vicinity of the top four luminous quasars, SDSS1426, OH91–121, SDSS1411 and HB89–1835, whose bolometric luminosities are estimated to be brighter than that of a typical hyper luminous quasar, $L_{\rm bol} > 10^{47}$ erg/s (Bischetti et al., 2017), using the bolometric correction of Runnoe et al. (2012). If these hyper luminous quasars are excluded, the trend becomes clearer as shown in Figure 30. This trend did not change even if the two possible quasars in HB89–1835 and SDSS1250 (white stars in Figure 24 and 27) are included. However, there is an uncertainty that the difference can be seen only beyond the completeness limit (gray region in Figure 30).

3.2.3 Equivalent Width Distributions of LAEs in the Vicinity of Quasars

It is well-known that the EW_0 of the Lyα emission is anti-correlated with the stellar masses of LAEs (e.g. Nilsson et al., 2009). The EW_0 of a LAE was estimated based on the proposed LAE model (see Appendix B). The correlation coefficient

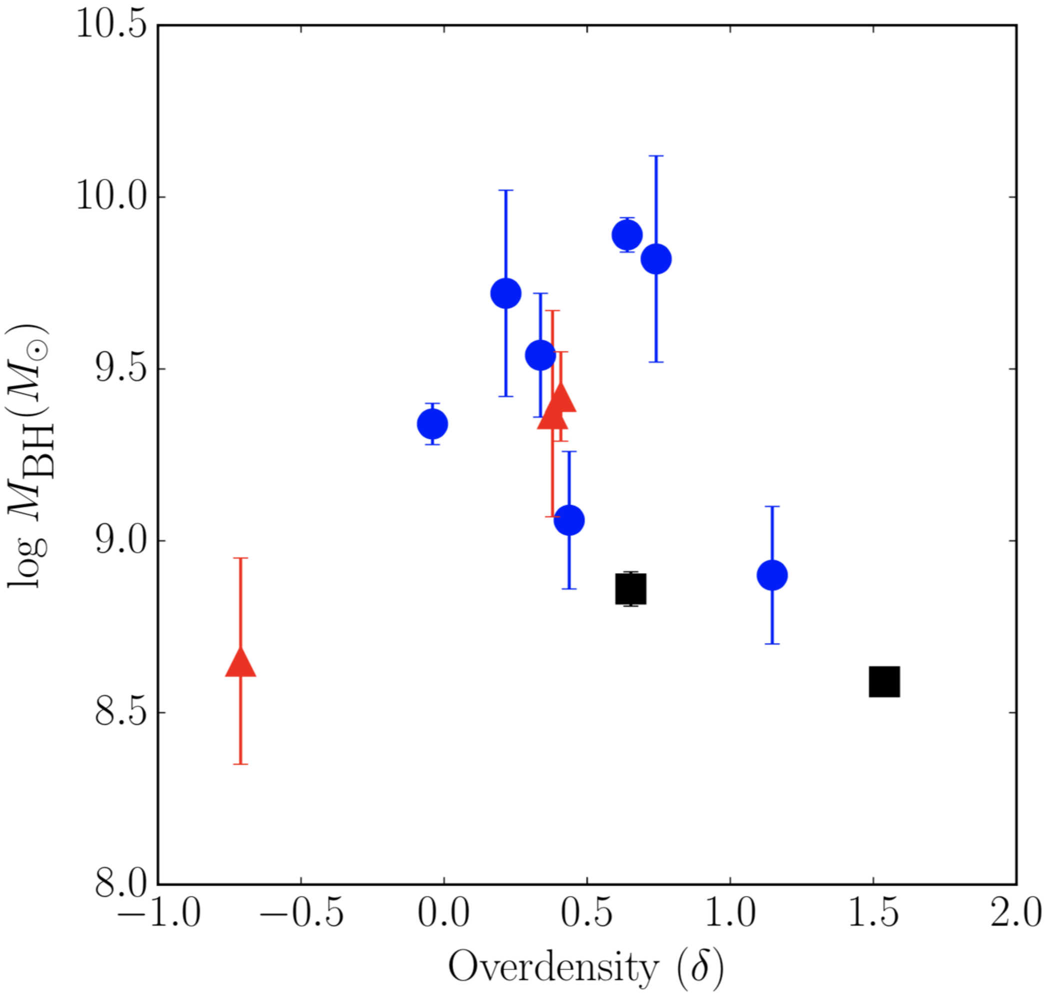

Figure 28 Relation between black hole mass and overdensity. The red triangle and blue points show the radio-loud and radio-quiet quasars, respectively. The quasar pair is represented by black squares.

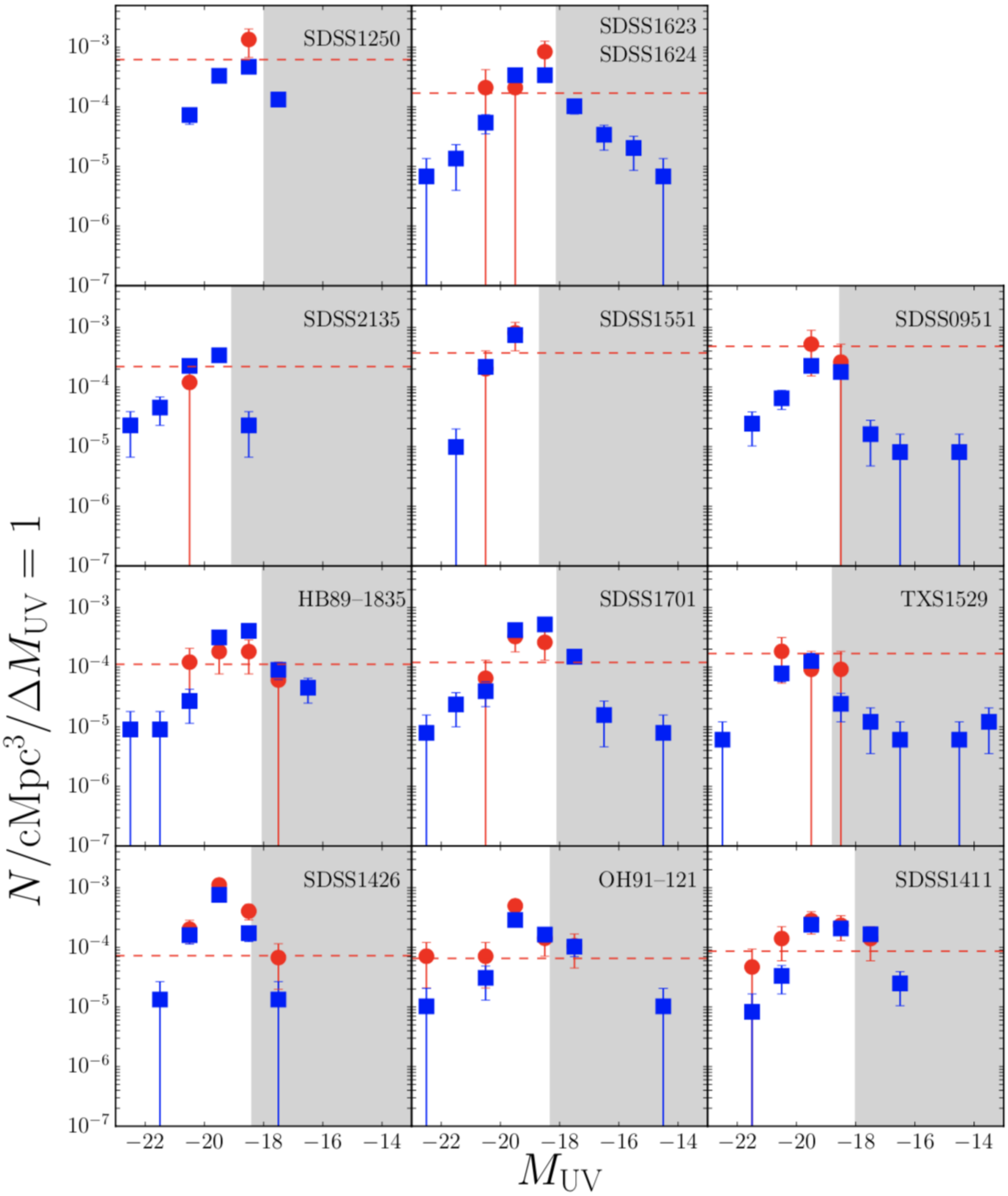

Figure 29 Distribution of M_{UV} of LAEs. The red circles and blue squares show the UV luminosity distribution in the bin width of $\Delta M_{UV}=1$ in the vicinity and outer region of the quasars, respectively. The error bar assumes a binomial distribution (Gehrels, 1986). The gray shaded region in each field shows the incomplete region where M_{UV} is larger than the M_{UV} limit which corresponds to the 5σ NB limiting magnitude, assuming the typical EW_0 value of 69Å which is the e-folding length of the EW_0 distribution in the field (see §3.3). For SDSS1426, the $J_{21}=10$ radius was used instead of the $J_{21}=1.0$ to evaluate the environmental effect because the radius of $J_{21}=1.0$ is larger than the FoV due to the brightness of the quasar. The upper limit for the case of no LAE detection (i.e., corresponds to $N=1.841$; Gehrels, 1986) is shown by the dashed red line.

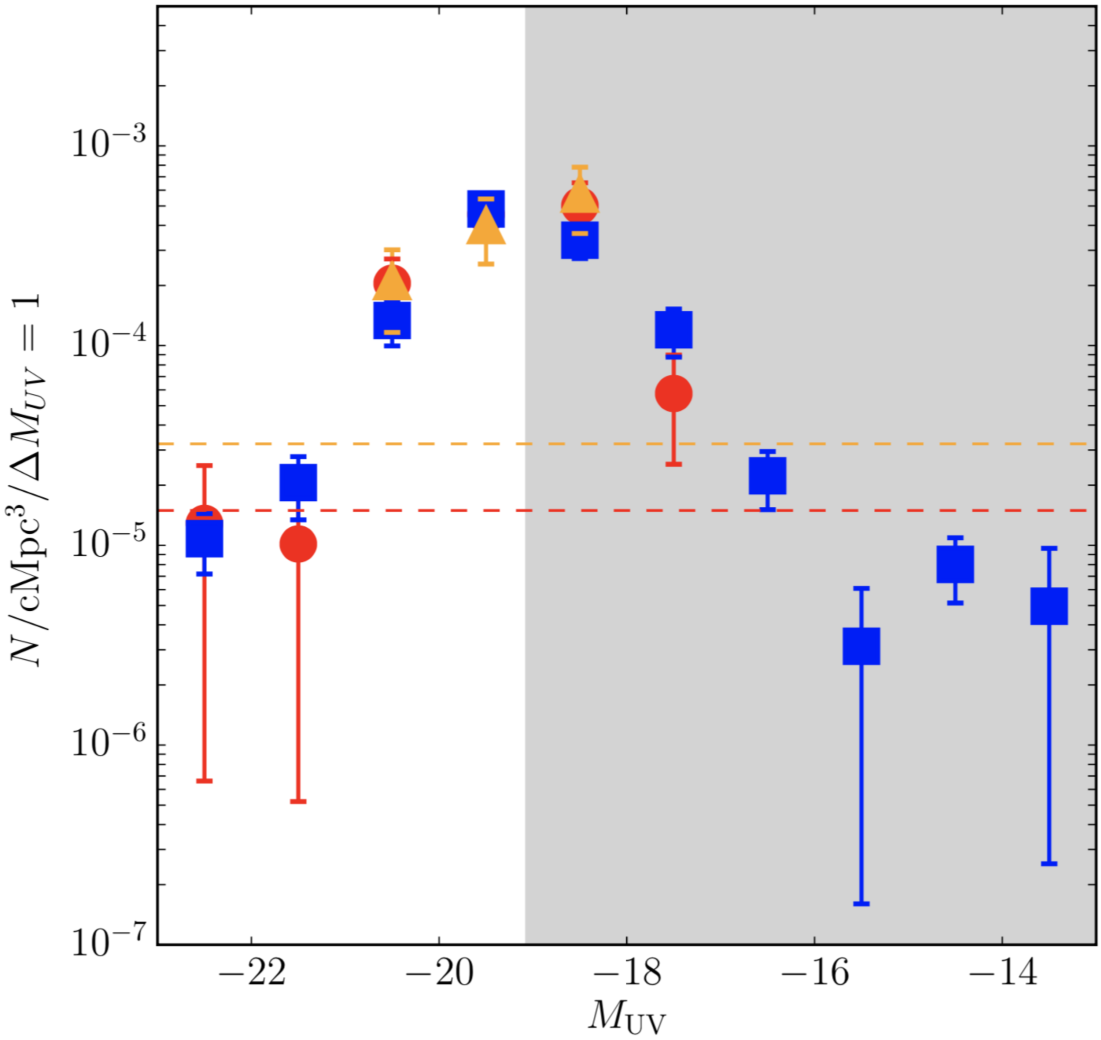

Figure 30 The average distribution of UV luminosity of LAEs in the vicinity of quasars. The red circles and blue squares show the distribution of M_{UV} n the bin width of $\Delta M_{UV} = 1$ in the vicinity and outer region of quasars, respectively. The error bars show the standard error of the mean of the sample number in each bin , except for Poisson error. The gray shaded region represents the completeness limit which corresponds to the M_{UV} at the shallowest 5σ NB limiting magnitude (that is, 24.95 in SDSS2131). In this case, it was assumed that the typical EW_0 value of 69Å which is the e-folding length of the EW_0 distribution in the field (see §3.3). The orange triangles show the resulting distribution if the four most luminous quasars, SDSS1411, SDSS1426, OH91–121 and HB89—1835 are excluded. The upper limit for no LAE detection is shown by the dashed red line.

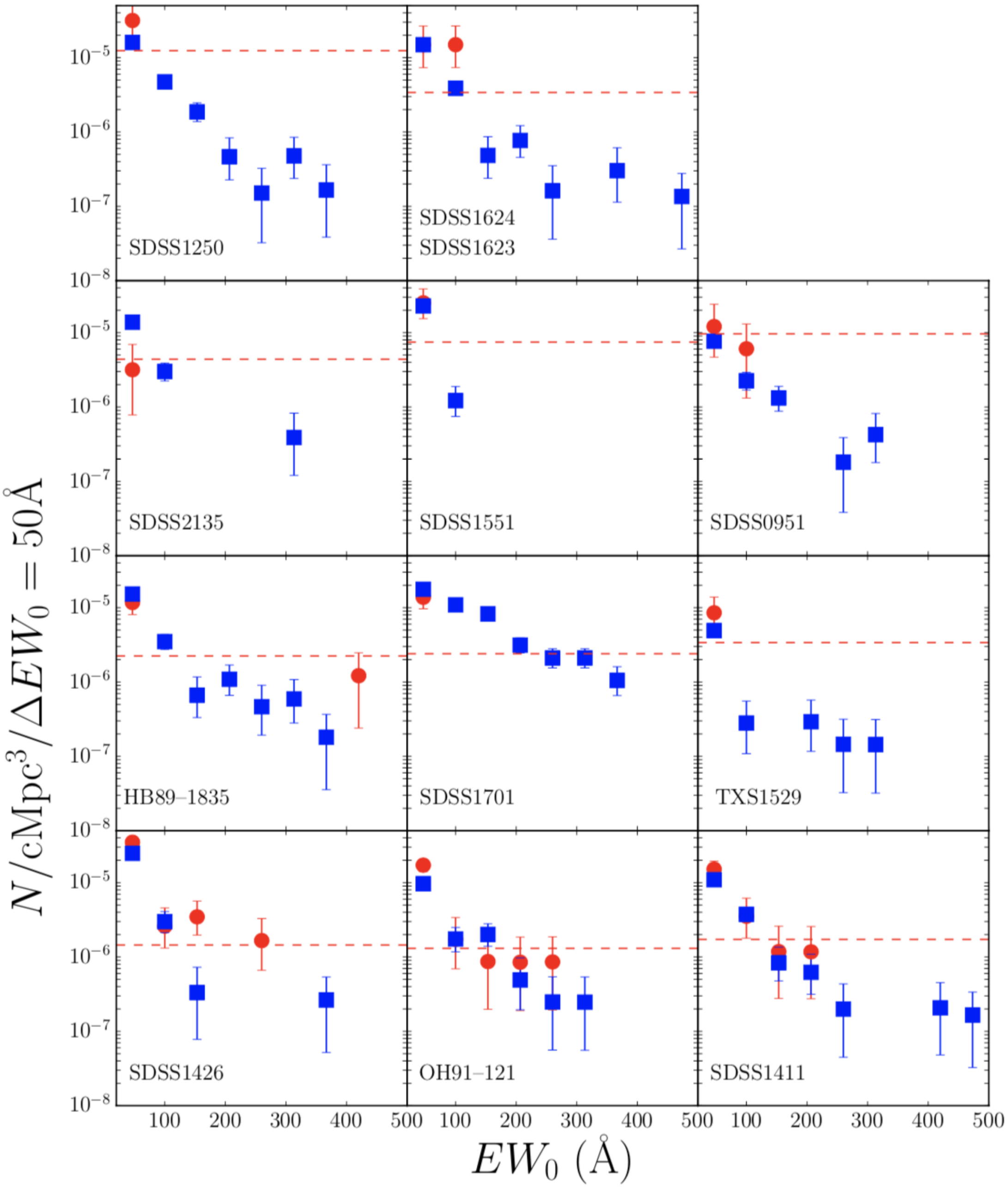

Figure 31 Distribution of EW_0 of LAEs in the vicinity of quasars. The filled red circles and blue squares represent the distribution in the bin width of $\Delta EW_0 =$ 50Å in the vicinity and outer region of the quasars, respectively. The error bar assumes a binomial distribution (Gehrels, 1986). For SDSS1426, the $J_{21} = 10$ radius was used instead of the $J_{21} = 1.0$ to evaluate the environmental effect because the radius of $J_{21} = 1.0$ is larger than the FoV due to the brightness of the quasar. The upper limit for the case of no LAE detection (i.e., corresponds to $N = 1.841$; Gehrels, 1986) is shown by the dashed red line.

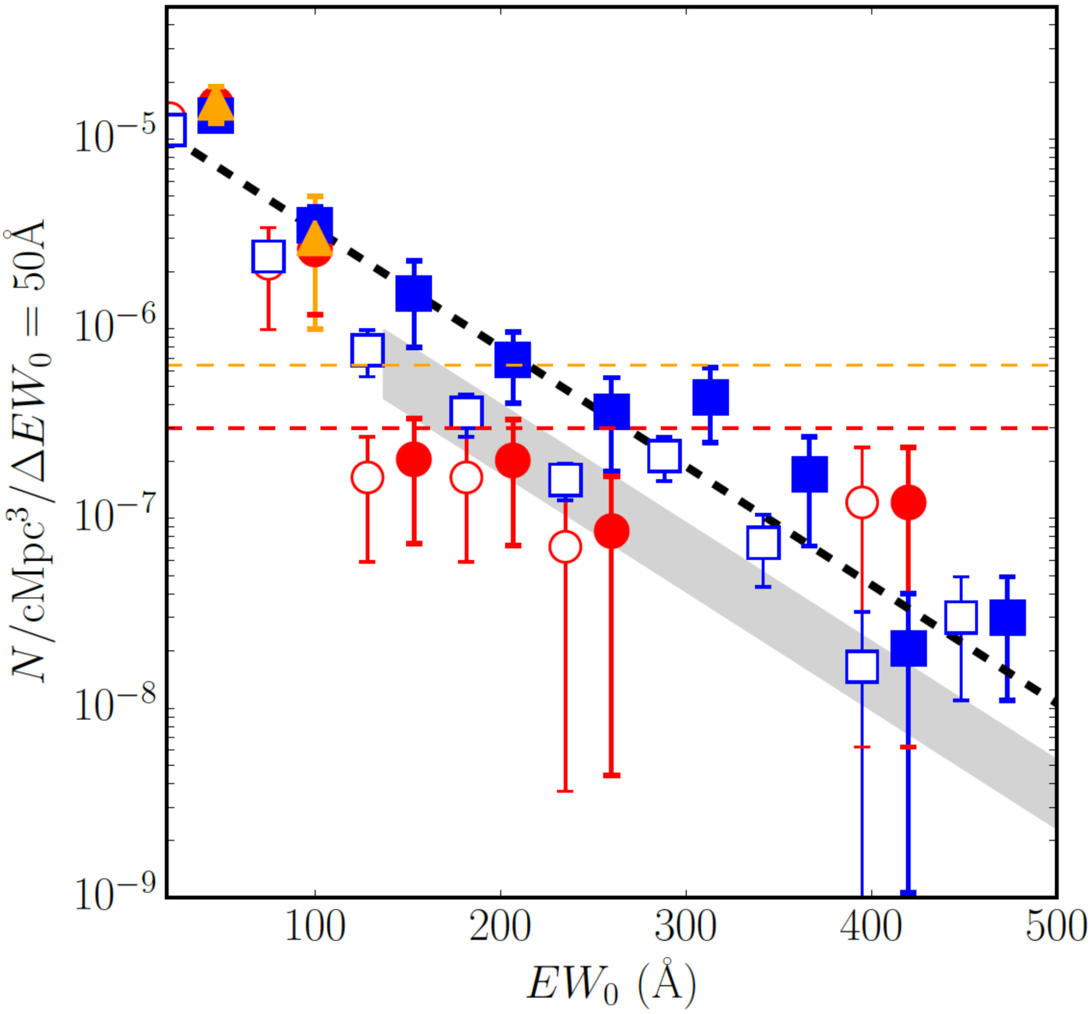

Figure 32 The average distribution of EW_0 of LAEs in the vicinity of quasars in the bin width of $\Delta EW_0 = 50\text{Å}$. The red circles and blue squares show the distribution in the vicinity and outer region of quasars, respectively. On the other hand, the red open circles and blue open squares, which are horizontally plotted by adding steps of $\delta EW_0 = 25\text{Å}$, show the distribution in the vicinity and outer region of quasars without completeness correction, respectively. The error bars represent the standard error of the mean of the sample number in each bin, except for Poisson error. The dashed black line indicates the best fit of the distribution in the outer region. The upper limit for no LAE detection is shown by the dashed red line. The orange triangles show the distributions in the vicinity excluding four of the most luminous quasars, SDSS1411, SDSS1426, OH91–121 and HB89–1835. The dashed orange line shows the upper limit for no LAE. The gray shaded region shows the expected distribution of LAEs in the vicinity of the quasars according to torus model (§3.3).

ρ and P-value between the EW_0 and $M_{\rm UV}$ distribution are 0.74 and $\ll 0.05$ in the Spearmann rank correlation test. The distribution of the EW_0 of the Lyα emission of the LAEs for each field is shown in Figure 31, which suggests that the LAEs in the quasar proximity region tend to have lower EW_0, especially, in the case of SDSS1701. The average EW_0 distribution for all fields but SDSS1426 are shown in Figure 32 in order to make the trend more pronounced. It was found that there is a tendency that LAEs with $EW_0 > 150$Å are less common in the proximity of quasars, while the abundance of LAEs with $EW_0 \lesssim 100$Å is almost the same in the vicinity and outer region. In the quasar proximity region, high-EW_0 LAEs with $EW_0 > 150$Å appeared only in the vicinity of the top four most luminous quasars. As is the case with the M_{UV} distribution, the trend becomes clearer if these hyper luminous quasars are excluded (Figure 32). The EW_0–UV luminosity relation (Nilsson et al., 2009) suggests that a LAE with a high EW_0 tends to have a lower UV luminosity. In fact, the $M_{\rm UV}$ of > -18.0 corresponds to $EW_0 > 150$Å in the EW_0–UV luminosity relation. The finding of a paucity of LAEs with high EW_0, which corresponds to low stellar mass objects around quasars could be caused by the quasar photoevaporation effect. A more quantitative discussion is provided in §3.4.1. Again, even if the two possible quasars (white stars in Figure 24 and 27) are added, the result did not change.

The deficit of LAEs with high EW_0 in the vicinity of the quasars could be due to the limited area rather than photoevaporation effects. I defined $N^{\rm obs}_{<r_{\rm prox}}(>150{\rm Å})$ and $N^{\rm exp}_{<r_{\rm prox}}(>150{\rm Å})$, which are summarized in Table 7, as the observed and expected completeness-corrected number of LAEs with $EW_0 > 150$Å, respectively. $N^{\rm exp}_{<r_{\rm prox}}(>150{\rm Å})$ is estimated assuming that the intrinsic LAE number density in the vicinity of a quasar is the same as that in the outer region. The highest expected number $N^{\rm exp}_{<r_{\rm prox}}(>150{\rm Å}) = 12.8$ was found in the SDSS1701 field even though $N^{\rm obs}_{<r_{\rm prox}}(>150{\rm Å}) = 0$. The difference may occur due to two possible overdense regions not being centered on the SDSS1701 quasar. As seen in Table 7, the total $N^{\rm obs}_{<r_{\rm prox}}(>150{\rm Å})$ is significantly smaller than the total $N^{\rm exp}_{<r_{\rm prox}}(>150{\rm Å})$. Interestingly, there are no LAEs with $EW_0 > 150$Å in the vicinity except for the top four brightest quasars. This is unlikely to be caused by a possible optical vignetting of S-Cam because the observed quasars always lie in the center of the images. I also performed χ^2 fitting using the equation, e^{-EW_0/w_0} that describes the EW_0 distribution in the outer region, and obtained $w_0 = 69^{+4}_{-6}$Å, which is consistent with Guaita et al. (2010) and Gronwall et al. (2007) who found that $w_0 = 83^{+10}_{-10}$Å at $z \sim 2$ and $w_0 = 76^{+11}_{-8}$Å at $z \sim 3$, respectively. However, the decay scale w_0 estimated by Nilsson et al. (2009) and Mawatari et al. (2012) at $z \sim 2$ is lower, $w_0 = 48.5^{+1.7}_{-1.7}$Å and $43.7^{+0.43}_{-0.43}$Å, respectively, and they suggest that redder galaxies populate LAEs at lower redshifts. If there is a focus on $z \sim 2$ in the sample, $w_0 = 73^{+4}_{-6}$Åis obtained. Although some w_0 evolution is observed in the redshift range of $\sim 3 - 6$ (Hashimoto et al., 2017), a consistent picture is still required for $z \sim 2 - 3$.

3.3 Discussion

Kashikawa et al. (2007) showed that a gas cloud in a halo with a small dynamical mass $M_{\rm vir} \lesssim 10^9 M_\odot$ will experience a considerable delay in star formation under a local UV background with $J_{21} \gtrsim 1$ based on the hydrodynamical simulation of Kitayama et al. (2000, 2001) as shown in Figure 33. In this simulation, the photoevaporation effect is quantitatively evaluated by solving self-consistently the UV photon radiative transfer, non-equilibrium chemical reaction, and the dynamics of baryon and dark matter, with the assumption of spherical symmetry. Recently, Hashimoto et al. (2017) concluded that LAEs with large Lyα, $EW_0 \sim 200 - 400$Å, have notably small stellar masses of $10^{7-8} M_\odot$, the median value of which is $7.1^{+4.8}_{-2.8} \times 10^7 M_\odot$ using the SED fitting method. Also, the stellar masses of LAEs with a smaller EW_0 of $\lesssim 150$Å, are found to be $5.9^{+19.2}_{-2.2} \times 10^8 M_\odot$ (Shimakawa et al., 2017). The stellar mass of LAEs can also be estimated from the Star Formation Rate (SFR)-stellar mass relation, the "main sequence". The average SFRs is 0.9 $M_\odot$ yr^{-1} for LAEs with $EW_0 > 150$Å and 6.4 $M_\odot$ yr^{-1} for those with $EW_0 < 150$Å(Kennicutt, 1998). Based on the main sequence of LAEs by Vargas et al. (2014), the stellar mass is estimated as $10^{7-8} M_\odot$ and $10^{8-9} M_\odot$ for $EW_0 > 150$Å and $EW_0 < 150$Å, respectively, which is consistent with the SED

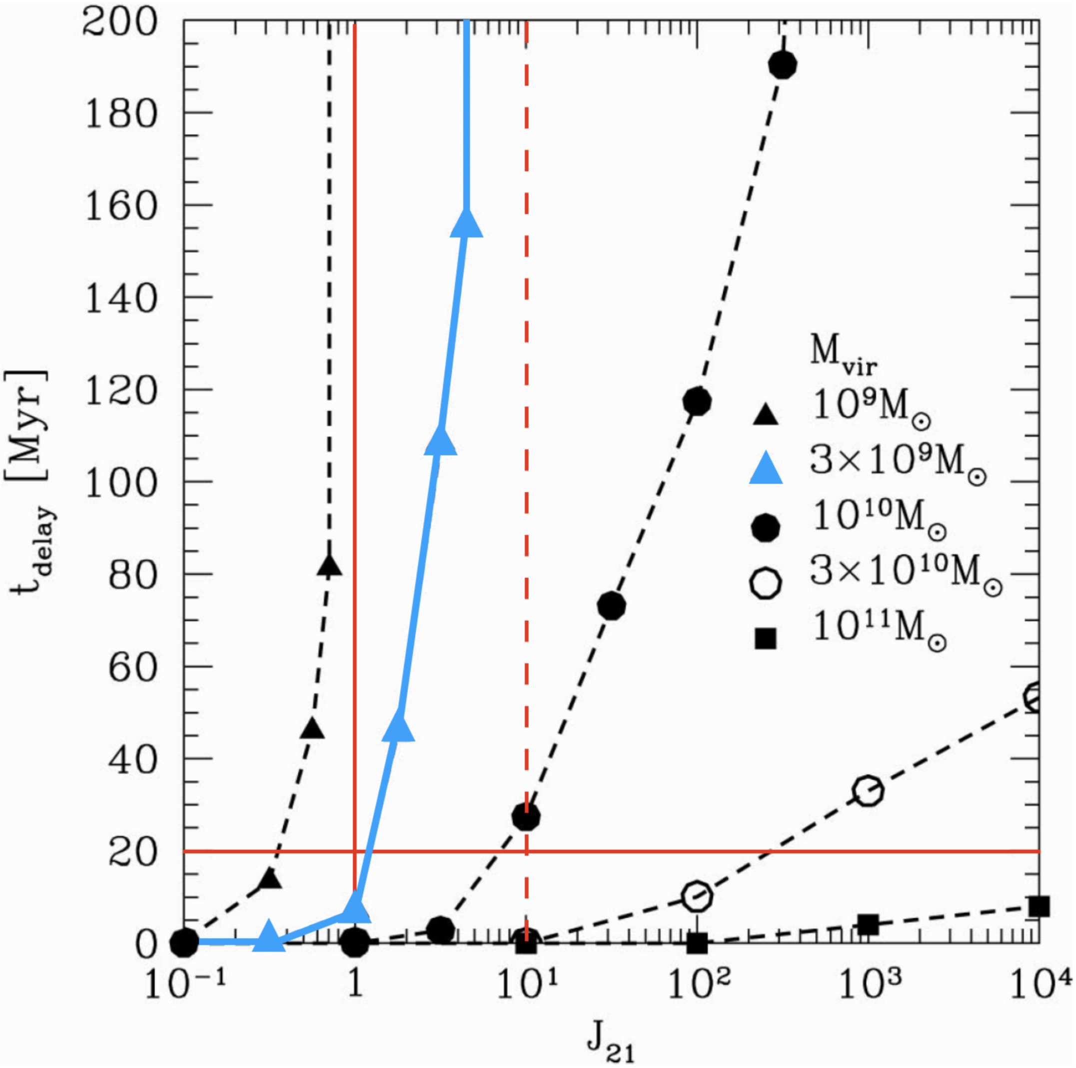

Figure 33 The delay time, $t_{\rm delay}$, of star formation in a halo with a dynamical mass under UV background with the intensity of J_{21}, taken from Kashikawa et al. (2007). The black triangle, blue triangle, black circle, open circle, and black square indicate the halo mass of $10^9 M_\odot$, $3 \times 10^9 M_\odot$ (the mean halo mass of LAEs with $EW_0 > 150$Å), $10^{10} M_\odot$, $3 \times 10^{10} M_\odot$, and $10^{11} M_\odot$, respectively. The right hand side of the red solid line represents the vicinity of our quasar by definition. The J_{21} of the UV radiation of the quasar in the vicinity can achieve at most ~ 10 (red dashed line). The typical age of LAEs with $EW_0 > 150$Å is $\lesssim 20$ Myr (horizontal red line) (Hashimoto et al., 2017).

fitting result. The stellar to halo mass ratio (SHMR) of LAEs at $z \sim 2$ is estimated to be $0.02^{+0.07}_{-0.01}$, assuming that each halo hosts one galaxy (Kusakabe et al., 2017). Therefore, it is expected that LAEs with $EW_0 \gtrsim 150$Å have a halo mass of $M_{\rm h} = 3.6^{+12.7}_{-2.3} \times 10^9 M_\odot$, and LAEs with $EW_0 \lesssim 150$Å occupy more massive halos of $M_{\rm h} = 2.9^{+14.0}_{-1.8} \times 10^{10} M_\odot$, using the stellar mass estimated by Hashimoto et al. (2017) and Shimakawa et al. (2017), and the SHMR of Kusakabe et al. (2017). It should be noted that the typical age of LAEs with $EW_0 > 150$Å is $\lesssim 20$ Myr (Hashimoto et al., 2017), which is shorter than the predicted delay time of > 20 Myr in star formation under a local UV background with $J_{21} \gtrsim 1$ for galaxies with the halo mass of $3.6 \times 10^9 M_\odot$, also based on hydrodynamical simulations (Kashikawa et al., 2007). Photoionization heating, which can raise the gas temperature due to the intense UV radiation from a quasar delays star formation in a small halo with mass smaller than $\sim 3 \times 10^9 M_\odot$, and its typical delay time is expected to be > 20 Myr. In other words, young galaxies with an age of < 20 Myr are prevented from forming by the quasar photoionization feedback. Therefore, the quasar photoionization feedback can reasonably explain the finding of a deficiency of LAEs, especially for LAEs with high EW_0 and low mass halos in the proximity of quasars, as shown in Figure 33. It should be noted that the quasar lifetime is also related to this effect. Even low-mass galaxies could collapse if they form before the quasar active phase. In addition, if the quasar life time is longer than ~ 20 Myr, a possible star formation delay mentioned above will be washed out. Interestingly, the delay time is comparable to the fiducial value of the quasar lifetime of $10^{7.5}$ yr, which is in agreement with observational results (Martini, 2004; Shen et al., 2007) and models (Hopkins et al., 2006), though with a large uncertainty.

The redshift uncertainty of the LAEs is estimated to be $\sim$ 30pMpc which is much larger than the typical scale of the quasar photoevaporation effect, $\sim$ 5pMpc, implying that the effect may be washed out. Nevertheless, it is interesting that there is a slight difference of the LAE distributions between the quasar vicinity and field as shown in Figure 32. The follow-up spectroscopic observation is key to limit the redshift error.

In §2, it was found that the number density of g-dropout galaxies in the vicinity of the SDSS quasars, whose median UV luminosity, log L_{912}, is equivalent to the result of this study, tend to be slightly deficient at < 0.5 pMpc in the vicinity of quasars. This might also be caused by the quasar photoionization feedback, though the scale is smaller than the proximity size, $r_{\rm prox} = 1.64^{+3.0}_{-3.0}$ pMpc, probed by LAEs in the study.

However, it was not possible to find evidence of the photoevaporation effect in the four hyper quasar fields, where the effect should perhaps be the strongest. According to the quasar evolution model of Kawakatu & Wada (2009), the brightness of a quasar is expected to monotonically decrease during the active phase. It should be noted that SDSS1426 has a large total infrared luminosity, $L_{\rm IR} = 10^{14.29}$ (Weedman et al., 2012), meaning that it is an X-ray bright, optically normal galaxy (XBONG) (Schawinski et al., 2015) or dusty quasar which is thought to be in the early stage of the quasar phase in the merger scenario (Kauffmann & Haehnelt, 2002). The ionization feedback from the luminous quasars may have not yet affected galaxies in their vicinity because they recently appeared. The result suggests that the timescale over which quasars can affect the gas cooling is estimated to be at most ~ 20 Myr, which is shorter than the quasar active phase time scale of a few ×100 Myr (Kawakatu & Wada, 2009), because the typical age of a LAE with high EW_0 is $\lesssim 20$ Myr (Hashimoto et al., 2017). However, the quasar evolution model of Kawakatu & Wada (2009) assumes the constant rate with time for the gas supplied from the host galaxy into the central SMBH. It is also thought that the quasar luminosity, which depends on the mass accretion rate, does not monotonically decrease but fluctuate with time (e.g. Choi et al., 2014). Observation of environments of newborn quasars (the dusty quasar or XBONG are the good candidates) is key in order to limit the uncertainty of the age of quasar. It is also interesting to examine the environments of dying quasars (§4.2.2). In addition, radio-loud quasars were found to reside in almost the same environment as radio-quiet quasars, as observed by Donoso et al. (2010) at $z \sim 0.5$. It was further found that quasar photoionization feedback is independent of radio-loudness.

In the context of the AGN unification model, quasars are observed relatively face-on with respect to the AGN torus, suggesting that the quasar photoionization feedback cannot affect directions that are transverse to the line of sight. The type 1 fraction of the AGN population is estimated to be approximately $50 - 70\%$ (Simpson, 2005), by estimating the [O III] luminosity from the UV luminosity using the bolometric correction factors of Runnoe et al. (2012) and Shen et al. (2011). Assuming that the fraction corresponds to the quasar viewing angle, the radiation solid angle of quasars is 0.47 – 0.79 radian. Thus, the expected number of LAEs with $EW_0 > 150$Å, which lie in the region where the quasar UV radiation is obscured by the torus is 7.3 – 12.1 based on the average EW_0 distribution (Figure 32). This expectation number is consistent with the observed number of LAEs with $EW_0 > 150$Å in the quasar proximity regions ($N^{\rm obs}_{<r_{\rm prox}}(>150\text{Å}) = 7.15$). In other words, the observed number of LAE with $EW_0 > 150$Å in the quasar proximity regions can be explained by the possible anisotropic radiation field of quasars.

I compared the results obtained with Marino et al. (2017) who investigated the photoionization effect in six quasar fields targeting galaxies with strong Lyα emission at $3 < z < 4$ using the MUSE (Multi Unit Spectroscopic Explorer). They found an opposite, positive correlation suggesting that LAEs with high EW_0 tend to cluster near the quasars. However, most of these high Lyα EW objects are likely to be caused by faint fluorescence, which can be detected by MUSE with high sensitivity. If their sample was confined to objects with UV continuum detections, there is no significant difference in the EW_0 distributions in the vicinity and outer regions of their quasars. Five of the six quasars are very luminous, $M_B \sim -30.0$ (Véron-Cetty & Véron, 2010), similar to SDSS1426 in the sample, suggesting that the results obtained are consistent with their results. Even if the SDSS1426 LAEs were limited to the sample with UV continuum detections only, this trend does not change. I found 195 LAEs that were not detected in BB images. The fraction of these continuum-undetected LAEs to the total 1171 sample is small (17%). Even if the 195 LAEs were excluded, the EW_0 and UV luminosity distribution did not change within 1σ errors. There was no difference in the number density of the continuum-undetected LAEs between the quasar vicinity and the outer region. Their continuum flux might not be detected due to the shallowness of the BB images, although they could be caused by the quasar fluorescence.

Another possible scenario to explain the scarcity of high EW_0 LAE, which is expected to be much younger than those with a lower EW_0 (Hashimoto et al., 2017), is that quasar fields could predominantly contain a more evolved population, such as LBGs. If quasars favor overdense environments, which enhance early galaxy formation, all the LAEs around the quasars might have already evolved into LBGs. This is also related to the quasar duty cycle: LBGs might have already formed at the time of the active phase of the quasar host galaxy. However, the statistical study in §2 showed that the most luminous quasars tend to avoid the overdense regions of LBGs, suggesting that quasars are not hosted by very massive halos that lack high EW_0 LAEs alone. This result raises some doubts about the aforementioned scenario. Simultaneous sampling for both LAEs and LBGs for quasar fields are required to validate this hypothesis.

Chapter 4 Summary and Discussion

In this thesis, the environment of a quasar throughout its lifetime was, for the first time, statistically and observationally studied. The findings imply that appearance of most quasars is independent of their large-scale environments. Once they appear, low-mass galaxy formation around the quasar will be suppressed because of the intense UV radiation from the quasar by photoevaporation. In this chapter, we summarize our findings in §2 and §3 (§4.1). Finally, we discuss these findings and show the future direction of our study (§4.2).

4.1 Summary

I examined the environment of quasars at high redshifts by solving the two questions; (1) In what environment do quasars exist? (2) How much influence do quasars have on surrounding galaxies? I summarized the findings for the two sides as follows.

1. What environment do quasars live in ? (§2)

   A statistically significant sample of 179 protoclusters from the HSC survey (Toshikawa et al., 2018) was used to investigate the spatial correlation between the protoclusters and quasars at $z \sim 4$. It should be noted that this sample is approximately 10 times as large as the number of all previously known protoclusters. I identified 151 SDSS quasars at $z = 3.3 - 4.2$ in the effective areas of the HSC-Wide layer, whose redshift range corresponds to the g-dropout selection function.

   The following results were obtained.

   - It was found that only 2 out of the 151 quasars reside in the protoclusters at $z \sim 4$. The overdensity significance at the quasar position is identical to that of g-dropout galaxies. In addition, the distribution of the angular separations from quasars to the nearest protoclusters is also identical to that of the separations from g-dropout galaxies. Therefore, it was suggested that quasars reside in almost the same environment as star-forming galaxies.

- I used stacking analysis to find that the average density of g-dropout galaxies around quasars is slightly higher than that around g-dropout galaxies on $1.0 - 2.5$ pMpc scales. However, at < 0.5 pMpc, the density around quasars tend to be lower.
- It was also found that quasars with a higher UV-luminosity or with more massive black holes tended to avoid the most overdense regions and that the quasar near zone sizes are anti-correlated with overdensity, although with weak 2σ significance.

The following possibilities are presented to account for the fact that the most luminous quasars do not exist in the most overdense regions: (1) galaxy major mergers might not be a principal requirement for efficient fuel supply and growth for quasars, (2) quasar photoionization feedback disturb galaxy formation, (3) the quasar halo mass at $z \sim 4$ is not massive enough to evolve into a cluster halo mass.

Interestingly, our results imply that most of the quasars might not be activated by a major merger, which is inconsistent with a general hypothesis that quasar activity is triggered by frequent mergers. Trakhtenbrot et al. (2017) found a diversity of host galaxy properties of luminous quasars at $z \sim 5$ in terms of SMBH fueling mechanisms, suggesting that galaxy merger may not be a necessary condition for either of the process, and other mechanisms that are not related to major mergers drive the fast growth of the most massive BHs. Another possible mechanism of fast SMBH and stellar growth in the early universe is secular processes, such as large-scale inflows of cold gas, that penetrate into the centers of massive dark matter halos. However, cold gas streams are also expected to converge and provide significant amount of gas supply to the SMBHs preferentially in large-scale overdense environments (e.g. Costa et al., 2014; Di Matteo et al., 2008; Sijacki et al., 2009). According to Dekel & Birnboim (2006), cold streams at $z > 2$ should still not be fully disrupted in the rare massive halo objects with $> 10^{12}M_{\odot}$ even if diluted by hot medium heated by quasar feedback. However, recent cosmological hydrodynamic simulation (e.g. Di Matteo et al., 2008) showed that strong feedback on massive halos with $> 10^{12}M_{\odot}$ at $z \sim 6$ stop the cold stream to penetrate into central BH. They mentioned that even though at $z < 6$ in massive halos the feedback energy clearly affect the inflowing cold gas, and it is not clear how significantly they disrupt the cold flows.

In the future, I will investigate a possible correlation between AGNs and the > 1000 complete protocluster candidates found in the HSC-SSP final data release with better statistical accuracy.

2. How much influence do quasars affect for surrounding galaxies ? (§3)

   Deep and wide imaging to target 11 quasar fields was performed to study the photoionization effect of young and low mass galaxies, LAEs systematically. In order to examine the variation of the ionization effects, quasars with a range of properties, such as radio-loudness, black hole mass ($\log M_{\rm BH}/M_{\odot} = 8.59 - 9.89$), and luminoisty ($\log\lambda L_{\lambda}(912\text{Å}) = 45.6 - 47.8$) were selected. I selected LAEs in the quasar fields and obtained 1171 LAEs in total, up to 5σ NB limiting magnitudes ($\sim 25 - 27$) and carefully performed visual examinations for fake detection. The proximity zone of a quasar is defined by the region where the local UV radiation from this entity is comparable to the UV background.

   The following results were obtained.

   - The 11 quasars tend to reside in average LAE density environments, whose average overdensity δ is 0.48 with 0.82σ significance. One quasar pair in the sample appears in the most overdense region. These findings are consistent with previous findings based on LBGs in §2 and Onoue et al. (2018).

- I compared the EW_0 and $M_{\rm UV}$ distribution of LAEs in the vicinity and outer region of a quasar. It is found that LAEs with high EW_0 ($EW_0 \gtrsim 150$Å) or equivalently, faint UV luminosity ($M_{\rm UV} \gtrsim -17.0$), are relatively scarce in the vicinity of the quasars. The range of EW_0 or $M_{\rm UV}$ corresponds to a notably smaller halo mass of $M_h \sim 10^{9-10} M_\odot$ estimated either from SED fitting or the main sequence, assuming $M_h/M_* \sim 50$. The LAEs with such low halo masses are expected to be subjected to quasar photoevaporation.
- Counter to the main trend, it was found that the feedback seems to be less effective in fields with hyper luminous quasars, but this could be explained by assuming that these luminous quasars are in the early stage of quasar activity. The environment around radio-loud quasars is similar to that in the vicinity of radio-quiet quasars.

In the thesis, for the first time, I performed a systematic study of quasar negative feedback on the surrounding galaxies. Future cosmological baryonic simulations including this kind of feedback will be invaluable for the interpretation of observational results.

4.2 Discussion Based on the Two Results

4.2.1 Consistency

There are two issues about the consistency of the two analysis in §2 and §3.

First, in §2, the most luminous quasars might suppress the star formation, suggested from lower density of LBGs in the vicinity of the quasars. However, in §3, it was found that the quasar photoevaporation effect is effective for LAEs which occupy less massive halos of $M_{\rm h} = 10^9 - 10^{10} M_\odot$, implying that the photoevaporation effect might not affect the LBGs because LBGs averagely have older and more massive population than LAEs. It should be noted that the less massive end of the halo mass function of LBGs broadly extends to the halo mass of $10^{10} M_\odot$ (Harikane et al., 2018), suggesting that the less massive part of LBGs can be subject to the quasar photoevaporation. The observation of less massive end of LBGs around quasars is key to get a consistent picture of photoevaporation.

Second is about the environment of the most luminous quasars. The photoevaporation seems to be less effective around hyper luminous quasars, implying that these quasars are still in an early stage of quasar activity (§3). On the other hand, the SDSS luminous quasars tend to avoid the galaxy overdense regions (§2). At first sight, these results look contradictory, but it was found that the average of bolometric luminosity of the latter 151 SDSS quasars is estimated to be $46.5^{+0.3}_{-0.3}$ erg/s using the bolometric correction of Runnoe et al. (2012). This estimated luminosity is much lower than the typical luminosity, $> 10^{47}$ erg/s, of hyper luminous quasars which is expected not to still affect the surrounding galaxies (§3), suggesting that the photoevaporation from our SDSS quasars could be occurred.

4.2.2 Open questions and Future Directions

Studies of quasar environments at various scales (from a few kpc to Mpc) and at different cosmic epochs are fundamental to understand the role of the environment in matter accretion onto the center of galaxies, possibly triggering the quasar activity. In the study, for the first time, (1) it was found that luminous quasars do not preferentially appear in protoclusters, and (2) implications regarding the quasar photoevaporation effect were observationally found. The synergy between these two effects (quasar photoionization vs excess of galaxy clustering around the quasars) is complex and depends upon many factors, such as the mass of the host galaxy, and the luminosity and opening angle of the quasar (e.g. Faucher-Giguère et al., 2008).

I will try to have a better understanding of the environments of high-z quasars by analyzing the following five things. The issues left unsolved and the solutions are summarized as follows.

1. Correlation between quasars and protoclusters.

   (a) Examine the environments of fainter quasars

   There is still a possibility that fainter quasars reside in the protoclusters because the quasar sample which was used in the study about the correlation between protoclusters and SDSS quasars in §2 is limited to be very luminous. A possible correlation between HSC-selected protoclusters and HSC-selected fainter quasars constructed by Akiyama et al. (2018) will be examined. This analysis allows us to examine whether fainter quasars exist in the protoclusters or not.

It is also important to understand the environments of the dusty quasars (e.g. Piconcelli et al., 2015), which are difficult to identify based on optical observation (e.g. HSC survey) due to the dust absorption. In fact, some dusty quasars has been being found in the protoclusters (e.g. Lehmer et al., 2009). The Infra Red (IR) or near IR spectroscopic observation such as the Multi-Object InfraRed Camera and Spectrograph (MOIRCS) mounted on Subaru telescope or upcoming Wide Field Infrared Survey Telescope (WFIRST), which has more light-gathering power. Targeting of the HSC-selected protoclusters could allow us to not only detect the dusty quasars but also examines whether their quasars reside in the protoclusters.

These analysis could lead to a comprehensive solution for the appearance mechanism of quasars with a wide range of the luminosity.

(b) Correlation between quasars and protoclusters in a variety of era.

It is non-trivial to confirm whether quasars do not live in the protoclusters even in a variety of era because the correlation between the protoclusters and quasars only at $z \sim 4$ in §2 was studied. It is suggested that the halo mass of quasars tend to be heavier in higher redshift (Shen et al., 2007). Thus, quasars at $z > 5$ may reside in the protoclusters. Actually, some quasars were found to reside in overdense regions at $z > 5$ (e.g. Husband et al., 2013). It is possible to construct the protoclusters at $z \sim 5$ and $z \sim 6$ using r-dropouts and i-dropouts for the upcoming deeper data of HSC-SSP.

The protocluster sample at $z \sim 3$ will be also constructed using the HSC-SSP data and CFHT Large Area u- band Deep Survey (CLAUDS) data which is one of the survey programs of Canada France Hawaii Telescope (CFHT), and a possible correlation between the protoclusters and quasars in a wide range of era will be examined. The u-band data of CLAUDS allow us to select the u-dropout galaxies which are LBGs at $z \sim 3$ and construct the protoclusters at $z \sim 3$ in the same way as the protocluster search at $z \sim 4$ (§2).

The quasar appearance mechanism may be better understood throughout a variety of eras by taking the correlation with SDSS quasars at the same era as the protoclusters.

2. Reducing the uncertainty of quasar photoevaporation feedbacks.

    (c) Simultaneous observation of LAEs and LBGs around quasars.

    For the first time, it was found that the less massive LAEs with a halo mass of $< 10^9 M_\odot$ are significantly deficient in the vicinity of quasars. However, there is a possibility that this deficiency might be occurred by not the photoevaporation but the evolution from LAEs into LBGs (Mori & Umemura, 2006). If quasars favor overdense environments, which enhance early galaxy formation, all the LAEs around quasars might have already evolved into LBGs. This is also related to the quasar duty cycle: LBGs might have already formed at the time of the active phase of the quasar host galaxy.

    I will resolve a degeneracy of this possibility by simultaneously observing the LAEs and LBGs around quasars. Firstly, the LBGs at $z \sim 3$ with the combination of HSC-SSP and CLAUDS data will be constructed, and the SDSS quasars in the same redshift as the LBGs will be selected. Then I will conduct the follow-up observation with NB468 filter, whose central wavelength is 4680Å , targeting their quasar fields, allowing to detect the LAEs at $z \sim 2.8$ and draw the distribution of LAEs and LBGs around the quasars. It may be concluded that if the densities of the LBGs in the vicinity of the quasars is more enhanced than those of the LAEs, the implication is that the LAEs have evolved into LBGs. However, in the case that the LBGs density is average or lower than LAEs, a deficiency can occur by quasar photoevaporation.

(d) Characterizing the environments of dying quasars

In §3, it was found that there was no evidence for the photoevaporation effect in some very luminous quasars. It is thought that the radiation from such quasars still not affect the surrounding galaxies because they just appeared. However, there is a possibility that quasar photoevaporation does not exist.

I will resolve the degeneracy by selecting dying quasars (Ichikawa & Inayoshi, 2017) and examining the distribution of galaxies around them. Dying quasars are the ones which the radiation from the SMBH was recently switched off. In the system of such dying quasar, the IR radiation from the dusty torus which lies at a distance of $\sim$ 10 pc from the center of the SMBH is weaker, but the emission from the narrow line region (e.g., [OIII] emission) at a distance of $\sim$ 1 kpc from the center is still stronger (see Figure 5). Thus, [OIII] emitters with strong emissions that are constructed in the HSC-SSP data (Hayashi et al., 2018) are good candidates for dying quasars. It is possible to select the dying quasar candidates using combinations of the [OIII] emitter catalog with Spitzer and WISE data (Ichikawa & Inayoshi, 2017).

Investigating galaxy densities in the vicinity of the dying quasars, we could restrict the quasar photoevaporation effect with the uncertainty of the appearance time of quasar excluded.

(e) Three-dimensional distribution of LAEs around quasar

It should be noted that NB imaging on §3 explores only a small redshift coverage at the same redshift of quasars, though the results are obtained on sky projection basis. The quasar proximity zones, which is typically $\sim$ 1.0pMpc, is much smaller than the NB's spatial coverage in the line-of-sight direction. According to the AGN unified model (Figure 5), an anisotropic structure of the quasar photoevapolation effect can be expected.

This question could be resolved by examining the three-dimensional distribution of LAEs in the vicinity of quasars, using the panoramic integral-field spectrograph. Recently, the LAE distribution in some quasar fields was examined using the MUSE mounted on VLT (Marino et al., 2017). However, because of extremely high luminosities of the quasars, and thus, the regions where the quasar photoevaporation effect affects is much far beyond the FoV of the MUSE. Our fainter quasars with a bolometric luminosity of $\sim 10^{45}$ erg s^{-1} are adequate to conduct the follow-up observations with MUSE to examine the distribution of LAEs. Moreover, using the upcoming Subaru/Prime Focus Spectrograph (PFS) which is a panoramic integral-field spectrograph with a FoV of $\sim$ 100 times larger than that of the MUSE is key for the examination of the environment of brighter quasars.

This would resolve not only the anisotropy of the photoevaporation, but also the geometric structure of the dusty torus.

Appendix A Estimate Black Hole Masses

I evaluated the black hole masses of quasars based on CIV single-epoch measurements (Vestergaard, 2002). For these $z \sim 4$ quasars, the best emission lines to estimate the black hole mass do not fall in the SDSS optical window, except for the CIV line. It is well-known that the CIV line region is subject to outflows and winds (e.g. Shen et al., 2008). This would likely result in large variances and possible biases in the estimated black hole masses. Nevertheless, if such non-virial motions occur at random, it is perhaps possible to statistically address any potential correlation between the environment and the properties of the black hole. Two black hole mass estimators were used, and the results were compared. Firstly, the calibrated single-epoch black hole estimator (Park et al., 2013) was used:

$$\begin{aligned} \log\left[\frac{M_{\rm BH}^{\rm Park+13}}{M_\odot}\right] = \alpha_{\rm P} \quad &+ \quad \beta_{\rm P}\log\left(\frac{L_{1350}}{10^{44}\ {\rm erg\ s^{-1}}}\right) \\ &+ \quad \gamma_{\rm P}\log\left(\frac{\Delta V_{\rm P}({\rm C\,IV})}{10^{3}\ {\rm km\ s^{-1}}}\right), \end{aligned} \tag{12}$$

where $L_{1350} = 1350 \times L_\lambda(1350)$ is the monochromatic continuum luminosity at 1350 Å and $\Delta V_{\rm P}({\rm C\,IV})$ is the full width at half maximum (FWHM) of the CIV which was taken from the SDSS DR12 catalog, 'FWHM_CIV'. The parameters $\alpha_{\rm P}$, $\beta_{\rm P}$, and $\gamma_{\rm P}$ are 7.48, 0.52, 0.56, respectively (Park et al., 2013). Figure 34 shows the relation between the estimated black hole masses of quasars and their g-dropout overdensities. The Spearman rank correlation test shows that the correlation coefficients are −0.216, −0.138, and −0.140, and the P-values are 0.0136, 0.111, and 0.107 for the three angular scales, respectively. These results hint at a weak anti-correlation between the black hole mass and overdensity.

Recently, Coatman et al. (2017) used the quasar spectra which have both Balmer lines and CIV lines to directly compare the velocity widths of their emission lines. They found the following updated estimator:

$$\log\left[\frac{M_{\rm BH}^{\rm Coatman+17}}{M_\odot}\right] = \alpha_{\rm C} \;+\; \beta_{\rm C}\log\left(\frac{L_{1350}}{10^{44}\ {\rm erg\ s^{-1}}}\right) + \gamma_{\rm C}\log\left(\frac{\Delta V_{\rm C}^{\rm correct}({\rm C}\,\textsc{iv})}{10^{3}\ {\rm km\ s^{-1}}}\right), \tag{13}$$

where $\alpha_{\rm C}$, $\beta_{\rm C}$, and $\gamma_{\rm C}$ are 6.71, 0.53, 2.00, respectively. Here, the $\Delta V_{\rm C}^{\rm correct}({\rm C}\,\textsc{iv})$ is the corrected FWHM of the CIV line taking into account the blueshift of the CIV due to the existence of outflows (Coatman et al., 2017). Coatman et al. (2017) found a strong correlation between the blueshift of the CIV and the black hole mass ratio estimated from Hα and CIV. Their results show that in order to correct the black hole mass estimated from CIV, it is necessary to apply a correction factor based on the blueshift of this line. The $\Delta V_{\rm C}^{\rm correct}({\rm C}\,\textsc{iv})$ is obtained from

$$\Delta V_{\rm C}^{\rm correct}({\rm C}\,\textsc{iv}) = \frac{\Delta V_{\rm C}({\rm C}\,\textsc{iv})}{(0.41 \pm 0.03) \times \frac{\rm CIV_{Blueshift}}{10^3} + 0.62 \pm 0.04} \tag{14}$$

In order to estimate these parameters the continuum shape was first substracted by fitting a power law ($f_\lambda \sim \lambda^\alpha$) using the continuum windows of the spectrum at 1445 − 1455 Å and 1695 − 1705 Å. The CIV line was fitted using a multi-Gaussian model, masking out the regions where absorption was detected above 1.5σ as in Shen et al. (2008). The FWHM and the blueshift (defined as $c \times (1549.48 - \lambda_{\rm half})/1549.48$, where c is the speed of light and $\lambda_{\rm half}$ is the centroid of the CIV estimated from the modeled profile, provides a more accurate measurement. For this estimator, the correlation coefficients are −0.194, −0.0969, and −0.0985, and the P-values are 0.0273, 0.263, and 0.257 respectively, in the Spearman rank correlation test. During this re-analysis, the most problematic quasars were flagged and excluded from the analysis of both the Park et al. (2013) and Coatman et al. (2017) results shown in Figure 34. To summarize, using both estimators we find very similar results. The results are the strongest for the smallest scale environment (< 1 arcmin) in the sense that quasars with the most massive black holes tend to avoid the most overdense regions. These results are summarized in Table 3.

Finally, I also compared the black hole mass and environment for the FIRST detected quasars. The fraction of the FIRST quasars tend to be high in high

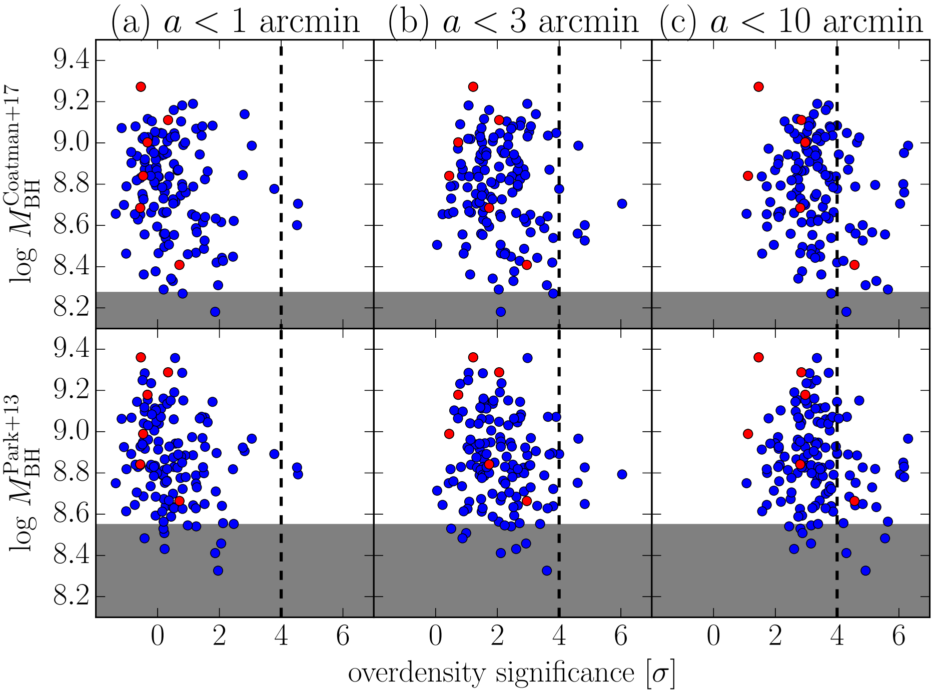

Figure 34 Black hole masses for overdensity significances about quasars using two black hole mass estimators, Coatman et al. (2017) estimator (first line) and Park et al. (2013) estimator (second line). The panel (a), (b) and (c) show the relation between the CIV-based back hole masses of quasars and the maximum overdensity significances centered on quasars with the radius of 1, 3, and 10 arcmin, respectively. The FIRST detected quasars are shown by the red points. The $> 4\sigma$ overdense regions are to the right of the dashed line. we show the complete limit (the gray shade regions), which corresponds to BOSS limiting magnitude of $r < 21.8$, assuming that the quasar spectrum energy density $f_\nu \propto \nu^{-0.5}$ and $\Delta V_{\rm P}(\rm CIV) = 4385.06$ and $V_{\rm C}^{\rm correct}(\rm CIV) = 2240.72$ km/s which are the median FWHM of CIV line of SDSS quasar sample at $z = 3.3 - 4.2$.

blackhole mass end as can be seen in Ichikawa & Inayoshi (2017), and they do not lie in particularly overdense regions, although the sample is very small (red points in Figure 19 and Figure 34).

Appendix B Model for Lyman α emitters

Herein, the model of a LAE used to estimate the continuum and Lyα emission luminosity from the galaxy based on BB and NB imaging is presented. The continuum flux density $f_\nu^{\rm cont}$ is assumed as

$$\begin{aligned} f_\nu^{\rm cont} &= a(\nu - \nu_{\rm Ly\alpha}) + b \quad \text{at} \quad \nu < \nu_{\rm Ly\alpha}, & (15) \\ &= 0 \qquad\qquad\qquad\quad \text{at} \quad \nu \geq \nu_{\rm Ly\alpha}, & (16) \end{aligned}$$

where $\nu_{\rm Ly\alpha}$ indicates the observed-frame frequency at the Lyα emission, and a and b are constants. Two different cases were discussed in my work: (1) BB covers Lyα emission, and (2) BB does not cover the emission.

CASE 1 : BB COVERS LYα EMISSION

The observed flux density in the NB and BB are, to a first approximation are given by:

$$\begin{aligned} \langle f_\nu \rangle_{\rm NB} \Delta_{\rm NB} &= F_{\rm Ly\alpha} + \frac{b\Delta_{\rm NB}}{2} & (17) \\ \langle f_\nu \rangle_{\rm BB} \Delta_{\rm BB} &= F_{\rm Ly\alpha} + b\delta + \frac{-a\delta^2}{2} & (18) \\ \delta &\equiv \nu_{\rm Ly\alpha} - \nu_{\rm BB} + \frac{\Delta_{\rm BB}}{2}, & (19) \end{aligned}$$

respectively. Here, $F_{\rm Ly\alpha}$ is the flux of the Lyman α emission, and $\Delta_{\rm NB}$ and $\Delta_{\rm BB}$ are the FWHM of the NB and BB filters in the frequency space, respectively, and $\nu_{\rm BB}$ is the central frequency of the BB filter. In addition, the following boundary conditions were imposed:

$$m_{\rm BB} - m_{\rm NB} = h \quad \text{at} \quad {\rm F}_{\rm Ly\alpha} = 0. \tag{20}$$

The h indicates the color term (see §2).

Solving the equation (17), (18) and (20), a Lyα luminosity $L_{\rm Ly\alpha}$, a UV flux density $f_{\rm UV}$, a rest-frame EW_0 of Lyα emission EW_0, and $f(EW_0 = 20\text{Å})$ in equation (7) can be obtained as follows;

$$\begin{aligned}
L_{\mathrm{Ly}\alpha} &= \frac{4\pi d_l^2 \Delta_{\mathrm{BB}} \Delta_{\mathrm{NB}}}{\Delta_{\mathrm{NB}} - 10^{-0.4h} \Delta_{\mathrm{BB}}} \left(\langle f_\nu \rangle_{\mathrm{BB}} - 10^{-0.4h} \langle f_\nu \rangle_{\mathrm{NB}} \right) & (21) \\
f_{\mathrm{UV}} &= 2 \frac{\Delta_{\mathrm{NB}} \langle f_\nu \rangle_{\mathrm{NB}} - \Delta_{\mathrm{BB}} \langle f_\nu \rangle_{\mathrm{BB}}}{\Delta_{\mathrm{NB}} - \Delta_{\mathrm{BB}} 10^{-0.4h}} & (22) \\
EW_0 &= \frac{(1+z)\lambda_{\mathrm{Ly}\alpha}^2}{2c} \frac{\Delta_{\mathrm{NB}} \Delta_{\mathrm{BB}} \left(\langle f_\nu \rangle_{\mathrm{BB}} - 10^{-0.4h} \langle f_\nu \rangle_{\mathrm{NB}} \right)}{\langle f_\nu \rangle_{\mathrm{NB}} \Delta_{\mathrm{NB}} - \langle f_\nu \rangle_{\mathrm{BB}} \Delta_{\mathrm{BB}}} & (23) \\
f &= -2.5 \log_{10} \left[\frac{2cEW_0 \Delta_{\mathrm{NB}} + 10^{-0.4h} (1+z) \lambda_{\mathrm{Ly}\alpha}^2 \Delta_{\mathrm{NB}} \Delta_{\mathrm{BB}}}{2cEW_0 \Delta_{\mathrm{BB}} + (1+z) \lambda_{\mathrm{Ly}\alpha}^2 \Delta_{\mathrm{NB}} \Delta_{\mathrm{BB}}} \right] & (24)
\end{aligned}$$

, where z is the redshift of the LAE, $\lambda_{\mathrm{Ly}\alpha}$ is the rest-frame wavelength of the Lyα emission, and c is the speed of light. d_l is the luminosity distance at each redshift.

CASE 2 : BB DOES NOT COVER LYα EMISSION

The observed flux density in the NB and BB are obtained by

$$\begin{aligned}
\langle f_\nu \rangle_{\mathrm{NB}} \Delta_{\mathrm{NB}} &= F_{\mathrm{Ly}\alpha} + \frac{b \Delta_{\mathrm{NB}}}{2} & (25) \\
\langle f_\nu \rangle_{\mathrm{BB}} \Delta_{\mathrm{BB}} &= \left(a(\nu_{\mathrm{Ly}\alpha} - \nu_{\mathrm{BB}}) + b \right) \Delta_{\mathrm{BB}} & (26) \\
m_{\mathrm{BB}} - m_{\mathrm{NB}} &= h \quad \text{at} \quad \mathrm{F}_{\mathrm{Ly}\alpha} = 0 & (27)
\end{aligned}$$

as in Case 1. Then, the following equations are obtained:

$$\begin{aligned}
L_{\mathrm{Ly}\alpha} &= 4\pi d_l^2 \Delta_{\mathrm{NB}} \left(10^{0.4h} \langle f_\nu \rangle_{\mathrm{BB}} - \langle f_\nu \rangle_{\mathrm{NB}} \right) & (28) \\
f_{\mathrm{UV}} &= 2 \langle f_\nu \rangle_{\mathrm{BB}} 10^{0.4h} & (29) \\
EW_0 &= \frac{(1+z)\lambda_{\mathrm{Ly}\alpha}^2}{2c} \frac{\left(10^{-0.4h} \langle f_\nu \rangle_{\mathrm{NB}} - \langle f_\nu \rangle_{\mathrm{BB}} \right) \Delta_{\mathrm{NB}}}{\langle f_\nu \rangle_{\mathrm{BB}}} & (30) \\
f &= -2.5 \log_{10} \left[\frac{(1+z) \lambda_{\mathrm{Ly}\alpha}^2 \Delta_{\mathrm{NB}} 10^{-0.4h}}{2cEW_0 + (1+z) \lambda_{\mathrm{Ly}\alpha}^2 \Delta_{\mathrm{NB}}} \right]. & (31)
\end{aligned}$$

I assumed that the flux density of a LAE is zero at wavelengths shorter than the Lyα wavelength. Even though, the residual flux could be as high as $\sim 60\%$ (Madau, 1995). In that case, the EW_0 estimate increases by 60%.

Bibliography

Abazajian, K., Adelman-McCarthy, J. K., Agüeros, M. A., et al. 2004, AJ, 128, 502

Adams, S. M., Martini, P., Croxall, K. V., Overzier, R. A., & Silverman, J. D. 2015, MNRAS, 448, 1335

Adelberger, K. L., & Steidel, C. C. 2005, ApJ, 630, 50

Aihara, H., Armstrong, R., Bickerton, S., et al. 2018, PASJ, 70, S8

Aihara, H., Arimoto, N., Armstrong, R., et al. 2018, PASJ, 70, S4

Akiyama, M., He, W., Ikeda, H., et al. 2018, PASJ, 70, S34

Axelrod, T., Kantor, J., Lupton, R. H., & Pierfederici, F. 2010, Proc. SPIE, 7740, 774015

Benson, A. J., Lacey, C. G., Baugh, C. M., Cole, S., & Frenk, C. S. 2002, MNRAS, 333, 156

Bischetti, M., Piconcelli, E., Vietri, G., et al. 2017, A&A, 598, A122

Borisova, E., Cantalupo, S., Lilly, S. J., et al. 2016, ApJ, 831, 39

Baldry, I. K., Glazebrook, K., Brinkmann, J., et al. 2004, ApJ, 600, 681

Bañados, E., Venemans, B., Walter, F., et al. 2013, ApJ, 773, 178

Barkana, R., & Loeb, A. 1999, ApJ, 523, 54

Bertin, E., & Arnouts, S. 1996, A&AS, 117, 393

Becker, R. H., White, R. L., & Helfand, D. J. 1995, ApJ, 450, 559

Behroozi, P. S., Wechsler, R. H., & Conroy, C. 2013, ApJ, 770, 57

Blandford, R. D., & Znajek, R. L. 1977, MNRAS, 179, 433

Böhringer, H., Schuecker, P., Guzzo, L., et al. 2001, A&A, 369, 826

Bond, J. R., Cole, S., Efstathiou, G., & Kaiser, N. 1991, ApJ, 379, 440

Bosch, J., Armstrong, R., Bickerton, S., et al. 2018, PASJ, 70, S5

Bower, R. G. 1991, MNRAS, 248, 332

Bruns, L. R., Wyithe, J. S. B., Bland-Hawthorn, J., & Dijkstra, M. 2012, MNRAS, 421, 2543

Chokshi, A. 1997, ApJ, 491, 78

Cai, Z., Fan, X., Peirani, S., et al. 2016, ApJ, 833, 135

Cantalupo, S., Lilly, S. J., & Porciani, C. 2007, ApJ, 657, 135

Chiang, Y.-K., Overzier, R., & Gebhardt, K. 2013, ApJ, 779, 127

Choi, E., Naab, T., Ostriker, J. P., Johansson, P. H., & Moster, B. P. 2014, MNRAS, 442, 440

Ciardullo, R., Gronwall, C., Adams, J. J., et al. 2013, ApJ, 769, 83

Coil, A. L., Hennawi, J. F., Newman, J. A., Cooper, M. C., & Davis, M. 2007, ApJ, 654, 115

Cole, S., Lacey, C. G., Baugh, C. M., & Frenk, C. S. 2000, MNRAS, 319, 168

Cooke, A. J., Espey, B., & Carswell, R. F. 1997, MNRAS, 284, 552

Cooke, E. A., Hatch, N. A., Muldrew, S. I., Rigby, E. E., & Kurk, J. D. 2014, MNRAS, 440, 3262

Costa, T., Sijacki, D., Trenti, M., & Haehnelt, M. G. 2014, MNRAS, 439, 2146

Coatman, L., Hewett, P. C., Banerji, M., et al. 2017, MNRAS, 465, 2120

Davis, M., Tonry, J., Huchra, J., & Latham, D. W. 1980, ApJ, 238, L113

Dawson, K. S., Schlegel, D. J., Ahn, C. P., et al. 2013, AJ, 145, 10

Dekel, A., & Birnboim, Y. 2006, MNRAS, 368, 2

Di Matteo, P., Bournaud, F., Martig, M., et al. 2008, A&A, 492, 31

Donoso, E., Li, C., Kauffmann, G., Best, P. N., & Heckman, T. M. 2010, MNRAS, 407, 1078

Dressler, A. 1980, ApJ, 236, 351

Djorgovski, S., Perley, R., Meylan, G., & McCarthy, P. 1987, ApJ, 321, L17

Donoso, E., Li, C., Kauffmann, G., Best, P. N., & Heckman, T. M. 2010, MNRAS, 407, 1078

Eftekharzadeh, S., Myers, A. D., White, M., et al. 2015, MNRAS, 453, 2779

Enoki, M., Nagashima, M., & Gouda, N. 2003, PASJ, 55, 133

Enoki, M., Ishiyama, T., Kobayashi, M. A. R., & Nagashima, M. 2014, ApJ, 794, 69

Fan, X., Strauss, M. A., Becker, R. H., et al. 2006, AJ, 132, 117

Fan, L., Knudsen, K. K., Fogasy, J., & Drouart, G. 2018, ApJ, 856, L5

Fanidakis, N., Baugh, C. M., Benson, A. J., et al. 2012, MNRAS, 419, 2797

Fanidakis, N., Macciò, A. V., Baugh, C. M., Lacey, C. G., & Frenk, C. S. 2013, MNRAS, 436, 315

Faucher-Giguère, C.-A., Lidz, A., Hernquist, L., & Zaldarriaga, M. 2008, ApJ, 688, 85

García-Vergara, C., Hennawi, J. F., Barrientos, L. F., & Rix, H.-W. 2017, ApJ, 848, 7

Gehrels, N. 1986, ApJ, 303, 336

Giavalisco, M. 2002, ARA&A, 40, 579

Guaita, L., Gawiser, E., Padilla, N., et al. 2010, ApJ, 714, 255

Gronwall, C., Ciardullo, R., Hickey, T., et al. 2007, ApJ, 667, 79

Grove, L. F., Fynbo, J. P. U., Ledoux, C., et al. 2009, A&A, 497, 689

Hashimoto, T., Ouchi, M., Shimasaku, K., et al. 2017, MNRAS, 465, 1543

Hashimoto, T., Garel, T., Guiderdoni, B., et al. 2017, A&A, 608, A10

Hayashi, M., Kodama, T., Koyama, Y., et al. 2010, MNRAS, 402, 1980

Hayashi, M., Tanaka, M., Shimakawa, R., et al. 2018, PASJ, 70, S17

Hopkins, P. F., Somerville, R. S., Hernquist, L., et al. 2006, ApJ, 652, 864

Hopkins, P. F., Hernquist, L., Cox, T. J., & Kereš, D. 2008, ApJS, 175, 356

Husband, K., Bremer, M. N., Stanway, E. R., et al. 2013, MNRAS, 432, 2869

Hatch, N. A., Wylezalek, D., Kurk, J. D., et al. 2014, MNRAS, 445, 280

Harikane, Y., Ouchi, M., Ono, Y., et al. 2018, PASJ, 70, S11

He, W., Akiyama, M., Bosch, J., et al. 2018, PASJ, 70, S33

Henriques, B. M. B., White, S. D. M., Lemson, G., et al. 2012, MNRAS, 421, 2904

Hopkins, P. F., Hernquist, L., Cox, T. J., & Kereš, D. 2008, ApJS, 175, 356-389

Hopkins, P. F., Cox, T. J., Kereš, D., & Hernquist, L. 2008, ApJS, 175, 390

Husband, K., Bremer, M. N., Stanway, E. R., et al. 2013, MNRAS, 432, 2869

Ichikawa, K., & Inayoshi, K. 2017, ApJ, 840, L9

Ishikawa, S., Kashikawa, N., Toshikawa, J., & Onoue, M. 2015, MNRAS, 454, 205

Ivezic, Z., Axelrod, T., Brandt, W. N., et al. 2008, Serbian Astronomical Journal, 176, 1

Jurić, M., Kantor, J., Lim, K., et al. 2015, arXiv:1512.07914

Kashikawa, N., Kitayama, T., Doi, M., et al. 2007, ApJ, 663, 765

Kawanomoto, S., Uraguchi, F., Komiyama, Y., et al. 2018, PASJ, 70, 66

Kereš, D., Katz, N., Weinberg, D. H., & Davé, R. 2005, MNRAS, 363, 2

Kikuta, S., Imanishi, M., Matsuoka, Y., et al. 2017, ApJ, 841, 128

Kim, S., Stiavelli, M., Trenti, M., et al. 2009, ApJ, 695, 809

Kodama, T., Arimoto, N., Barger, A. J., & Arag'on-Salamanca, A. 1998, A&A, 334, 99

Kodama, T., Tanaka, I., Kajisawa, M., et al. 2007, MNRAS, 377, 1717

Koyama, Y., Kodama, T., Tadaki, K.-i., et al. 2013, MNRAS, 428, 1551

Kawakatu, N., Umemura, M., & Mori, M. 2003, ApJ, 583, 85

Kang, E., & Im, M. 2015, Journal of Korean Astronomical Society, 48, 21

Kitayama, T., Tajiri, Y., Umemura, M., Susa, H., & Ikeuchi, S. 2000, MNRAS, 315, L1

Kitayama, T., Susa, H., Umemura, M., & Ikeuchi, S. 2001, MNRAS, 326, 1353

Kauffmann, G., & Haehnelt, M. G. 2002, MNRAS, 332, 529

Kawakatu, N., & Wada, K. 2009, ApJ, 706, 676

Kennicutt, R. C., Jr. 1998, ARA&A, 36, 189

Kikuta, S., Imanishi, M., Matsuoka, Y., et al. 2017, ApJ, 841, 128

Kusakabe, H., Shimasaku, K., Ouchi, M., et al. 2017, arXiv:1707.09373

Kuiper, E., Hatch, N. A., Röttgering, H. J. A., et al. 2010, MNRAS, 405, 969

Lacey, C., & Cole, S. 1993, MNRAS, 262, 627

Lacey, C. G., Baugh, C. M., Frenk, C. S., et al. 2015, arXiv:1509.08473

Larson, K. L., Sanders, D. B., Barnes, J. E., et al. 2016, ApJ, 825, 128

Lee, K.-S., Dey, A., Cooper, M. C., Reddy, N., & Jannuzi, B. T. 2013, ApJ, 771, 25

Lehmer, B. D., Alexander, D. M., Geach, J. E., et al. 2009, ApJ, 691, 687

Lin, L., Patton, D. R., Koo, D. C., et al. 2008, ApJ, 681, 232-243

Lee, K.-G., Bailey, S., Bartsch, L. E., et al. 2013, AJ, 145, 69

Magnier, E. A., Schlafly, E., Finkbeiner, D., et al. 2013, ApJS, 205, 20

Mori, M., & Umemura, M. 2006, New Astron. Rev., 50, 199

Madau, P. 1995, ApJ, 441, 18

Magorrian, J., Tremaine, S., Richstone, D., et al. 1998, AJ, 115, 2285

Marconi, A., & Hunt, L. K. 2003, ApJ, 589, L21

Marino, R. A., Cantalupo, S., Lilly, S. J., et al. 2017, arXiv:1709.03522

Matsuda, Y., Yamada, T., Hayashino, T., et al. 2005, ApJ, 634, L125

Matsuda, Y., Yamada, T., Hayashino, T., Yamauchi, R., & Nakamura, Y. 2006, ApJ, 640, L123

Mawatari, K., Yamada, T., Nakamura, Y., Hayashino, T., & Matsuda, Y. 2012, ApJ, 759, 133

Miyazaki, S., Komiyama, Y., Sekiguchi, M., et al. 2002, PASJ, 54, 833

Miyazaki, S., Komiyama, Y., Nakaya, H., et al. 2012, Proc. SPIE, 8446, 84460Z

Magliocchetti, M., Maddox, S. J., Jackson, C. A., et al. 2002, MNRAS, 333, 100

Magliocchetti, M., Popesso, P., Brusa, M., et al. 2016, arXiv:1606.08286

Malkan, M. A., & Sargent, W. L. W. 1982, ApJ, 254, 22

Martini, P. 2004, Coevolution of Black Holes and Galaxies, 169

Mauch, T., & Sadler, E. M. 2007, MNRAS, 375, 931

Morselli, L., Mignoli, M., Gilli, R., et al. 2014, A&A, 568, A1

Mortlock, D. J., Warren, S. J., Venemans, B. P., et al. 2011, Nature, 474, 616

Mazzucchelli, C., Bañados, E., Decarli, R., et al. 2017, ApJ, 834, 83

McConnell, N. J., Ma, C.-P., Gebhardt, K., et al. 2011, Nature, 480, 215

McNamara, B. R., Wise, M., Nulsen, P. E. J., et al. 2000, ApJ, 534, L135

Nakajima, K., Ouchi, M., Shimasaku, K., et al. 2012, ApJ, 745, 12

Nakamura, F., & Li, Z.-Y. 2011, ApJ, 740, 36

Nagashima, M., Yahagi, H., Enoki, M., Yoshii, Y., & Gouda, N. 2005, ApJ, 634, 26

Netzer, H., Lira, P., Trakhtenbrot, B., Shemmer, O., & Cury, I. 2007, ApJ, 671, 1256

Nilsson, K. K., Möller-Nilsson, O., Møller, P., Fynbo, J. P. U., & Shapley, A. E. 2009, MNRAS, 400, 232

Nilsson, K. K., Tapken, C., Møller, P., et al. 2009, A&A, 498, 13

Ocvirk, P., Pichon, C., & Teyssier, R. 2008, MNRAS, 390, 1326

Ono, Y., Ouchi, M., Harikane, Y., et al. 2018, PASJ, 70, S10

Onoue, M., Kashikawa, N., Uchiyama, H., et al. 2018, PASJ, 70, S31

Oogi, T., Enoki, M., Ishiyama, T., et al. 2016, MNRAS, 456, L30

Orsi, Á. A., Fanidakis, N., Lacey, C. G., & Baugh, C. M. 2016, MNRAS, 456, 3827

Overzier, R. A., Shu, X., Zheng, W., et al. 2009, ApJ, 704, 548

Overzier, R. A. 2016, A&A Rev., 24, 14

Ota, K., Venemans, B. P., Taniguchi, Y., et al. 2018, ApJ, 856, 109

Ouchi, M., Shimasaku, K., Okamura, S., et al. 2004, ApJ, 611, 660

Park, D., Woo, J.-H., Denney, K. D., & Shin, J. 2013, ApJ, 770, 87

Pâris, I., Petitjean, P., Ross, N. P., et al. 2017, A&A, 597, A79

Piconcelli, E., Vignali, C., Bianchi, S., et al. 2015, A&A, 574, L9

Press, W. H., & Schechter, P. 1974, ApJ, 187, 425

Ross, N. P., Myers, A. D., Sheldon, E. S., et al. 2012, ApJS, 199, 3

Rozo, E., Rykoff, E. S., Evrard, A., et al. 2009, ApJ, 699, 768

Runnoe, J. C., Brotherton, M. S., & Shang, Z. 2012, MNRAS, 422, 478

Schlafly, E. F., Finkbeiner, D. P., Jurić, M., et al. 2012, ApJ, 756, 158

Shen, Y., Strauss, M. A., Oguri, M., et al. 2007, AJ, 133, 2222

Shen, Y., Greene, J. E., Strauss, M. A., Richards, G. T., & Schneider, D. P. 2008, ApJ, 680, 169-190

Shen, Y., Richards, G. T., Strauss, M. A., et al. 2011, ApJS, 194, 45

Shen, Y., McBride, C. K., White, M., et al. 2013, ApJ, 778, 98

Simpson, C. 2005, MNRAS, 360, 565

Sijacki, D., Springel, V., & Haehnelt, M. G. 2009, MNRAS, 400, 100

Steidel, C. C., Adelberger, K. L., Shapley, A. E., et al. 2005, ApJ, 626, 44

Saito, T., Matsuda, Y., Lacey, C. G., et al. 2015, MNRAS, 447, 3069

Saito, Y., Imanishi, M., Minowa, Y., et al. 2016, PASJ, 68, 1

Selsing, J., Fynbo, J. P. U., Christensen, L., & Krogager, J.-K. 2016, A&A, 585, A87

Schawinski, K., Koss, M., Berney, S., & Sartori, L. F. 2015, MNRAS, 451, 2517

Shapley, A. E., Steidel, C. C., Adelberger, K. L., et al. 2001, ApJ, 562, 95

Shemmer, O., Netzer, H., Maiolino, R., et al. 2004, ApJ, 614, 547

Shimakawa, R., Kodama, T., Shibuya, T., et al. 2017, MNRAS, 468, 1123

Sulentic, J. W., Marziani, P., del Olmo, A., et al. 2014, A&A, 570, A96

Schawinski, K., Koss, M., Berney, S., & Sartori, L. F. 2015, MNRAS, 451, 2517

Saripalli, L., Hunstead, R. W., Subrahmanyan, R., & Boyce, E. 2005, AJ, 130, 896

Shapley, A. E., Steidel, C. C., Erb, D. K., et al. 2005, ApJ, 626, 698

Thomas, D., Maraston, C., Bender, R., & Mendes de Oliveira, C. 2005, ApJ, 621, 673

Tonry, J. L., Stubbs, C. W., Lykke, K. R., et al. 2012, ApJ, 750, 99

Toshikawa, J., Kashikawa, N., Overzier, R., et al. 2014, ApJ, 792, 15

Toshikawa, J., Kashikawa, N., Overzier, R., et al. 2016, ApJ, 826, 114

Toshikawa, J., Uchiyama, H., Kashikawa, N., et al. 2018, PASJ, 70, S12

Tadaki, K.-i., Kodama, T., Tamura, Y., et al. 2014, ApJ, 788, L23

Tanaka, I., De Breuck, C., Kurk, J. D., et al. 2011, PASJ, 63, 415

Trainor, R. F., & Steidel, C. C. 2012, ApJ, 752, 39

Trakhtenbrot, B., Volonteri, M., & Natarajan, P. 2017, ApJ, 836, L1

Terlevich, A. I., Caldwell, N., & Bower, R. G. 2001, MNRAS, 326, 1547

Urry, C. M., & Padovani, P. 1995, PASP, 107, 803

van Dokkum, P. G. 2001, PASP, 113, 1420

van der Burg, R. F. J., Hildebrandt, H., & Erben, T. 2010, A&A, 523, A74

Venemans, B. P., Röttgering, H. J. A., Miley, G. K., et al. 2005, A&A, 431, 793

Venemans, B. P., Röttgering, H. J. A., Miley, G. K., et al. 2007, A&A, 461, 823

Vestergaard, M. 2002, ApJ, 571, 733

Véron-Cetty, M.-P., & Véron, P. 2010, A&A, 518, A10

Vargas, C. J., Bish, H., Acquaviva, V., et al. 2014, ApJ, 783, 26

White, M., Myers, A. D., Ross, N. P., et al. 2012, MNRAS, 424, 933

Weedman, D. W. 1985, ApJS, 57, 523

Weedman, D., Sargsyan, L., Lebouteiller, V., Houck, J., & Barry, D. 2012, ApJ, 761, 184

Wisotzki, L., Bacon, R., Blaizot, J., et al. 2016, A&A, 587, A98

Yagi, M., Kashikawa, N., Sekiguchi, M., et al. 2002, AJ, 123, 66

Zauderer, B. A., Veilleux, S., & Yee, H. K. C. 2007, ApJ, 659, 1096